AD-A198 627 FILE COPY

②

AFOSR-TR. 88-0933

Final Scientific Report

on

FUNDAMENTAL PROCESSES IN PARTIALLY IONIZED PLASMAS

Grant AFOSR-83-0108

Prepared for

AIR FORCE OFFICE OF SCIENTIFIC RESEARCH

For the Period

February 1, 1983 to January 31, 1988

DTIC
S ELECTE D
AUG 25 1988
E

Submitted by

C. H. Kruger, Principal Investigator
M. Mitchner, Co-Principal Investigator
S. A. Self, Co-Principal Investigator

HIGH TEMPERATURE GASDYNAMICS LABORATORY
Mechanical Engineering Department
Stanford University

document has been approved
public release and sale; its
distribution is unlimited.

88 8 25

Final Scientific Report

on

FUNDAMENTAL PROCESSES IN PARTIALLY IONIZED PLASMAS

Grant AFOSR-83-0108

Prepared for

AIR FORCE OFFICE OF SCIENTIFIC RESEARCH

For the Period

February 1, 1983 to January 31, 1988

Accession For
NTIS GRA&I ☒
DTIC TAB ☐
Unannounced ☐
Justification
By
Distribution/
Availability Codes
Dist | Avail and/or Special
A-1

Submitted by

C. H. Kruger, Principal Investigator
M. Mitchner, Co-Principal Investigator
S. A. Self, Co-Principal Investigator

QUALITY INSPECTED 2

UNCLASSIFIED
SECURITY CLASSIFICATION OF THIS PAGE

AD-A198 621

REPORT DOCUMENTATION PAGE

1a. REPORT SECURITY CLASSIFICATION: Unclassified

1b. RESTRICTIVE MARKINGS: None

2a. SECURITY CLASSIFICATION AUTHORITY:

2b. DECLASSIFICATION / DOWNGRADING SCHEDULE:

3. DISTRIBUTION / AVAILABILITY OF REPORT: Approved for public release; distribution unlimited

4. PERFORMING ORGANIZATION REPORT NUMBER(S):

5. MONITORING ORGANIZATION REPORT NUMBER(S): AFOSR-TR- 88-0933

6a. NAME OF PERFORMING ORGANIZATION: Stanford University

6b. OFFICE SYMBOL (If applicable):

7a. NAME OF MONITORING ORGANIZATION: Air Force Office of Scientific Research

6c. ADDRESS (City, State, and ZIP Code):
Department of Mechanical Engineering
Stanford, California 94305-3030

7b. ADDRESS (City, State, and ZIP Code):
Directorate of Physical & Geo. Sci. AFOSR/NP
Bolling AFB, Building 410
Washington, DC 20332

8a. NAME OF FUNDING / SPONSORING ORGANIZATION: Air Force Office of Scientific Research

8b. OFFICE SYMBOL (If applicable): NP

9. PROCUREMENT INSTRUMENT IDENTIFICATION NUMBER: Grant AFOSR-83-0108

8c. ADDRESS (City, State, and ZIP Code):
Directorate of Physical & Geo. Science
AFOSR/NP, Bolling AFB, Building 410
Washington, DC 20332

10. SOURCE OF FUNDING NUMBERS

PROGRAM ELEMENT NO	PROJECT NO	TASK NO	WORK UNIT ACCESSION NO
61102F	2301	B2	

11. TITLE (Include Security Classification): Fundamental Processes in Partially Ionized Plasmas

12. PERSONAL AUTHOR(S): C. H. Kruger, PI, M. Mitchner, Co-PI, S. A. Self, Co-PI

13a. TYPE OF REPORT: Final Scientific Report

13b. TIME COVERED: FROM 2/1/83 TO 1/31/88

14. DATE OF REPORT (Year, Month, Day): 88/05/15

15. PAGE COUNT: [redacted] 153

16. SUPPLEMENTARY NOTATION: → Magnetohydrodynamics, (MHD) ←

17. COSATI CODES

FIELD	GROUP	SUB-GROUP

18. SUBJECT TERMS (Continue on reverse if necessary and identify by block number)
Plasma, Sheath, Secondary Flow Power, Cathode
Recombination, Boundary layer, Diagnostics, Anode Discharge
Three-body, MHD, Electrothermal, Breakdown

19. ABSTRACT (Continue on reverse if necessary and identify by block number)

This report describes the results of a five-year research program on the Fundamental Processes in Partially Ionized Plasmas conducted in the High Temperature Gasdynamics Laboratory at Stanford University. This research is directed to three major areas: recombination in molecular plasmas, discharge effects (plasma electrode interaction) and interaction of discharges and fluid dynamics. Recombination and ionization are fundamental processes that play a role in nearly all applications and natural phenomena that involve partially ionized plasmas. Under the present program, experiments have been designed and theoretical analyses conducted to obtain a better knowledge of the rates of electron recombination in the presence of molecular species. Sudies were undertaken of the near-electrode region and the processes by which current is transferred in the region between a plasma and an electrode. A study of the interaction of discharges and fluid dynamics has measured the significant secondary flows and their effects caused by the interaction of a magnetic field with a current-carrying plasma.

Keywords

20. DISTRIBUTION / AVAILABILITY OF ABSTRACT: ☒ UNCLASSIFIED/UNLIMITED ☒ SAME AS RPT. ☐ DTIC USERS

21. ABSTRACT SECURITY CLASSIFICATION: Unclassified

22a. NAME OF RESPONSIBLE INDIVIDUAL: Lt Col Bruce Smith

22b. TELEPHONE (Include Area Code): 202-767-4908

22c. OFFICE SYMBOL: NP

DD FORM 1473, 84 MAR

83 APR edition may be used until exhausted
All other editions are obsolete.

SECURITY CLASSIFICATION OF THIS PAGE
UNCLASSIFIED

Table of Contents

Section Page

1.0 INTRODUCTION 1

2.0 PROJECT DESCRIPTIONS 3

2.1 Recombination in Molecular Plasmas 3

2.1.1 Introduction 3
2.1.2 Research Objectives 7
2.1.3 Status of Research 7

A. Theoretical Work 8
A.1 Supersonic Expansion Approach 8
A.2 Pulsed Photoionization Approach 14

B. Experimental Work 33
B.1 Reaction Cell 34
B.2 Gas Handling 41
B.3 Light Sources 48
B.4 Diagnostics 51
B.5 Conclusions 62

2.2 Discharge Effects: Plasma-Electrode Interaction 64

2.2.1 Introduction 64
2.2.2 Research Objectives 66
2.2.3 Status of Research 66

A. Governing Equations and Non-Dimensionalization 67

B. Boundary Conditions 70

C. Solutions 73
C.1 Isothermal Quasi-Neutral Solution (Analytic) 74
C.2 Isothermal Solution (Numerical) 81
C.3 Non-Isothermal Solution, Simplified Energy Equation (Numerical) 96
C.4 Non-Isothermal Solution, Complete Set of Equations (Numerical) 103

2.3 Interaction of Plasma Currents and Fluid Mechanics: MHD Secondary Flow 108

2.3.1 Introduction 108
2.3.2 Research Objectives 109
2.3.3 Status of Research 110

A. Theoretical Background 110
A.1 Description of Experiments 113

B. Experimental Results 121
B.1 Transverse Velocity Measurements 121
B.2 Effects of Secondary Flow 125

Section **Page**

B.3 Dependence of Secondary Flow and Related Effects on Interaction Parameter 134
B.4 Summary and Conclusions 137

3.0 REFERENCES 139

4.0 PUBLICATIONS AND PRESENTATIONS 146

5.0 PERSONNEL 148

1.0 INTRODUCTION

This report describes results obtained during a five-year research program on the Fundamental Processes in Partially Ionized Plasmas conducted in the High Temperature Gasdynamics Laboratory at Stanford University. This research was supported by a grant from the Air Force Office of Scientific Research (AFOSR-83-0108) and was conducted under the direction of Professors Charles H. Kruger, Morton Mitchner, and Sidney Self. Three Ph.D. candidates are currently conducting their doctoral research under this program, while one student completed his Ph.D. with support from the program.

Several space power and propulsion systems of potential long-range interest to the Air Force involve partially ionized plasmas. Such systems include MPD thrusters, both open- and closed-cycle MHD power generation, and thermionic energy conversion. Although the specific configurations, the exact operating conditions, and which of the competing systems will prove to be most useful in the long term remain to be established, it is important at this time to provide a broad fundamental research base in support of development activity. In particular, there are a number of key issues regarding the properties and discharge behavior of partially ionized plasmas and the interaction of discharges with fluid dynamics that need to be understood before the potential and limitations of competing systems can be fully evaluated. In addition, it is important that outstanding young applied scientists be educated in these areas.

The present research on partially ionized plasmas is discipline- rather than device-oriented and is focused on three major areas:

1. Recombination in molecular plasmas
2. Discharge effects: plasma electrode interaction
3. Interaction of discharges and fluid dynamics

In addition, each of these areas involves the development and application of modern plasma diagnostic techniques.

These areas are overlapping and mutually supportive. Thus, understanding of plasma properties is important to the study of discharges and their interaction with fluid dynamics. In the same spirit, plasma diagnostic methods are developed so that they can be applied in achieving our research objectives. In areas 1) and 3), the research is primarily experimental in nature, with supporting theoretical studies for the planning of the research and interpretation of the data. Area 2) has so far been restricted to theoretical modeling and computations.

Progress in each of the three research areas is described in Section 2.0. Publications and Presentations resulting from this work are cited in Section 4.0, and Section 5.0 lists the personnel who have contributed to this report.

2.0 PROJECT DESCRIPTIONS

Included in this section are descriptions of progress in each of three project areas. Each project contains the following subsections: (a) Introduction; (b) Research Objectives; and (c) Status of Research. Additional descriptions may be found in the publications listed in Section 4.0.

2.1 Recombination in Molecular Plasmas

2.1.1 Introduction

The equilibrium thermodynamic properties and the quasi-equilibrium transport properties of partially ionized plasmas have been fairly well worked out, at least with regard to the theoretical aspects, and many important results are given in the book Partially Ionized Gases [1.1]. There remain, however, a number of areas where plasma properties are not now adequately understood, particularly with regard to nonequilibrium plasmas. Since a knowledge of plasma properties is fundamental to any system description, it is important that this area receive appropriate attention. The electron density is often the single most important thermodynamic property; in many nonequilibrium situations it is determined by finite ionization and recombination rates. These rates in turn depend on the constituents of the gas and the form of nonequilibrium.

In applications of interest to the Air Force (e.g., MHD generators and space propulsion) where a high-pressure (i.e., of the order of an atmosphere) partially-ionized plasma flows past a cooled surface, recombination of electrons occurs with positive alkali-metal ions M^+ under conditions for which there have been few, if any, reported measurements of the recombination rate. Typically, these conditions are for relatively low electron number densities n_e where the three-body recombination process

$$e + M^+ + e \longrightarrow M + e \; , \qquad (1.1)$$

usually dominant at higher electron number densities (e.g., $n_e \gtrsim 10^{12}$ cm^{-3}, at $T \gtrsim 1000$ K), no longer plays a major role. (The recombination coefficient α_e for this process is defined by the relation $dn_e/dt = -\alpha_e n_e n_i$, where n_i denotes the ion number density and t is the time.)

The goal of this study is to obtain an improved understanding of recombination processes under the aforementioned conditions of low n_e and atmospheric pressures, by developing a means for producing a highly nonequilibrium plasma in a mixture containing an alkali metal vapor and a molecular gas, and making measurements thereon. From an engineering point-of-view, it is the actual value of the recombination rate which is of primary importance, independent of what the underlying kinetic mechanisms may be. However, a knowledge of the mechanisms is very useful in that it enables one to extrapolate and predict values of the recombination rate for conditions that go beyond those for which measurements exist.

In addition to measurements of the recombination rates, another objective of our proposed work is therefore to identify the operative recombination mechanisms and to make comparisons of our measurements with existing theories. It has been proposed by Bates et al. [1.2] that the three-body recombination process

$$e + M^+ + X_k \longrightarrow M + X_k \qquad (1.2)$$

where X_k denotes a molecular species, is important under the conditions of interest. The recombination coefficient α_k for this reaction (defined by the relation $dn_e/dt = -\alpha_k n_e n_i$) has been calculated by Bates et al. [1.2] for the case of nitrogen molecules, but no experiments have been reported to date that would enable a comparison to be made with theory.

At higher pressures, collisional atomic processes dominate radiative processes, so that one may employ the important simplifications $\alpha_e = n_e \alpha_e'(T)$ and $\alpha_j = n_j \alpha_j'(T)$. Here $\alpha_e'(T)$ and $\alpha_j'(T)$ are functions of temperature, and n_j denotes the number density of the molecular species j. The quantities α_e' and α_j' are also referred to (loosely) as recombination coefficients.

Experimental studies of the recombination process in which the third body is an atom or molecule have been carried out using (hydrocarbon) flames [1.3], where the products of combustion contained several molecular species. To extract information about the individual molecules X_j, the assumption was made that the contributions from the different molecules in the mixture were additive. Expressed equivalently, in terms of recombination coefficients, it was assumed that the overall rate α (which was measured, in effect) could be written in terms of the individual rates α_j by the formula

$$\alpha = \sum_j x_j \alpha_j ,$$

where $x_j = n_j/n$ denotes the mole fraction of species X_j. Here n_j is the number density of species X_j and n is the total number density.

The results obtained in this fashion have been strongly criticized by Bates [1.4], who claimed that the recombination coefficient for a molecular mixture is not additive, but that it is given by the formula

$$\alpha = \frac{n}{\eta} \{ \sum_p \frac{1}{\sum_j x_j B_j(p)} \}^{-1} .$$

The quantities $B_j(p)$ are related to the rates of de-excitation of M by X_j from all energy levels above and including p, to all levels below p. The factor η is given in terms of atomic constants and the temperature T as $(2\pi m_e kT/h^2)^{3/2} = KT^{3/2}$. Values of $B_j(p)$ have been calculated by Bates et al. [1.2] for the molecular species H_2 and N_2.

For a single species, one obtains from this expression for α the result

$$\alpha_j = \frac{n_j}{\eta} \{ \sum_p \frac{1}{B_j(p)} \}^{-1} .$$

It is therefore apparent that the value of α for a mixture of molecules cannot be written, in general, in terms of the individual α_j. To be able to calculate α for a mixture, the factors $B_j(p)$ must be used. However, before being able to rely on the calculated factors $B_j(p)$, it is necessary to test the theory by obtaining data in which only a single molecular species X_j is present in the recombining gas together with the alkali metal M. It is clear that flame experiments are unable to yield such data.

A further distinction between the theory by Bates et al. [1.2] and the ad hoc additive rule is illustrated in Fig. 1.1, where the calculated recombination coefficient of a mixture of H_2 and N_2 is shown, based on calculated values of $B_j(p)$. A significant departure from the additive rule is clearly evident.

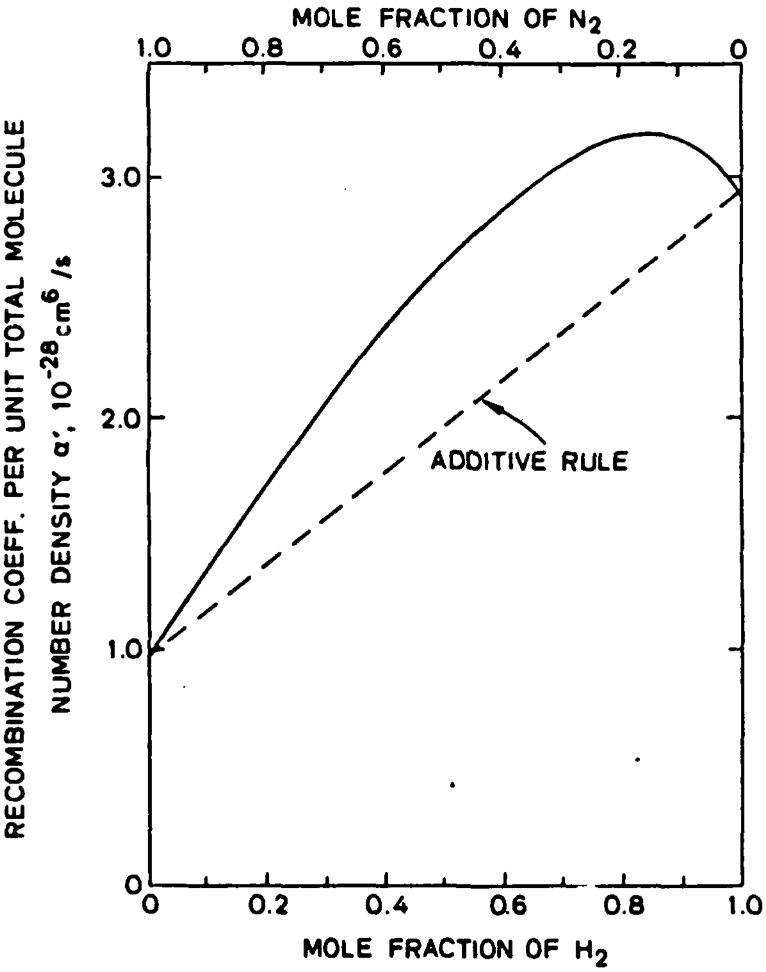

Fig. 1.1. Calculated recombination coefficient of a mixture of N_2 and H_2 per unit total molecule number density, at a temperature of 2000 K.

2.1.2 Research Objectives

1. To design and construct an experimental system that can produce a recombining alkali metal plasma under conditions where the molecular three-body process dominates.
2. To examine, in particular, the recombination of cesium ions in the presence of nitrogen.
3. To measure the desired recombination rate as a function of the background gas temperature.
4. To measure the recombination rate as a function of the partial pressures of Cs and N_2.
5. To examine the recombination rate of interest in a mixture of molecular species.

2.1.3 Status of Research

The remainder of this section describes first theoretical calculations directed at analyzing two possible experimental systems for producing the nonequilibrium conditions necessary for studying the desired three-body molecular recombination process. One concept is based on the use of a supersonic nozzle to rapidly expand a flowing high-temperature plasma consisting of N_2 and thermally ionized Cs. This approach would provide steady-state conditions. Measurements of n_e at several spatial locations (e.g., before and after the expansion) would provide information for determining the recombination coefficient. The second concept would employ a pulse of radiation to produce ionizational nonequilibrium by photoionization of Cs vapor confined with N_2 in a heated test volume. Measurements of n_e as a function of time following a rapid quenching of the photoionizing radiation would enable determination of the recombination rate. The reasons for choosing the second approach are presented.

The second part of this section describes the experimental work performed in developing the necessary hardware to execute the pulsed photoionization experiments. The work is presented in four main parts: Reaction Cell, Gas Handling, Light Sources, and Diagnostics.

A. Theoretical Work

A.1 Supersonic Expansion Approach

A.1.1 Experimental Configuration

An experimental system for producing a nonequilibrium recombining plasma using a supersonic expansion approach is illustrated schematically in Fig. 1.2. An arc heater is used to produce a flow of high-temperature Ar into a large plenum chamber. An alkali metal vapor such as cesium or potassium is added to the gas, together with various molecular species introduced either singly, or in controlled combinations. The purpose of the plenum is to permit a thorough mixing of the gases and to enable the mixture to come to thermodynamic equilibrium.

The gas mixture then flows through a chamber viewport where the stagnation temperature of the gas can be measured with thermocouples and by spectroscopic methods. A convergent-divergent supersonic nozzle follows, in which the gas is rapidly cooled, so that electron recombination

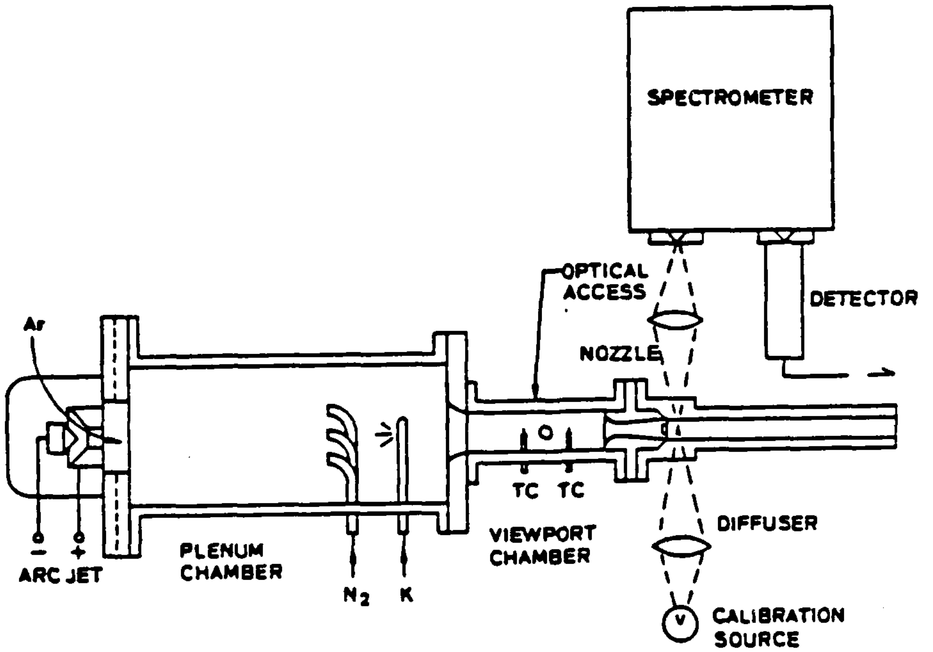
SPECTROMETER
OPTICAL ACCESS
DETECTOR
Ar
NOZZLE
O
TC TC
DIFFUSER
− +
ARC JET
PLENUM CHAMBER
N_2
K
VIEWPORT CHAMBER
V
CALIBRATION SOURCE

Fig. 1.2. Experimental system based on supersonic expansion approach.

is induced. The electron number density is measured spectroscopically or by an electrical conductivity diagnostic at the exit of the nozzle, thereby providing data from which the recombination coefficient can be calculated. The gas then passes through a supersonic diffuser and is exhausted to the atmosphere.

A.1.2 Recombination Model

To design the apparatus, it is necessary to determine approximately the optimal experimental conditions, within the constraints imposed by the operating limits of the arc jet. These conditions include the plenum pressure and temperature, the number densities of the potassium (which we shall take here to be the alkali metal vapor) and the molecular gas additives, and the geometry of the converging-diverging nozzle. Since three-body recombination will occur in which both the electrons and the molecules serve as third bodies, it is desirable that experiments be conducted for conditions such that the latter process is dominant. Shown in Fig. 1.3, are the values of α'_{N_2} for N_2, as calculated by Bates et al. [1.2], and the values of α'_e as given by Hinnov and Hirschberg [1.5]. We shall take N_2 as the molecular third body in the discussion that follows.

The quasi-one-dimensional steady-state electron continuity equation that governs the behavior of n_e, is

$$u \frac{dn_e}{dx} + n_e \frac{du}{dx} + un_e \frac{d}{dx} \ell n\, A = \dot{n}_e \, ,$$

where $\dot{n}_e$ denotes the net electron production rate, and is given by the expression

$$\dot{n}_e = \left(n_K s - n_e^2\right) \left(n_e \alpha'_e + n_{N_2} \alpha'_{N_2}\right) .$$

Here $s = s(T) = KT^{3/2} \exp(-\varepsilon_i/kT)$, where ε_i is the ionization energy of potassium. In obtaining $\dot{n}_e$, the ionization rates have been expressed as $S_e = s(T)\alpha'_e$ and $S_{N_2} = s(T)\alpha'_{N_2}$ by use of the method of detailed balancing. The gas flow speed u (as well as all other gas properties) is given in terms of the cross-sectional area of the nozzle $A = A(x)$, by the well-known relations of gas dynamics [1.6].

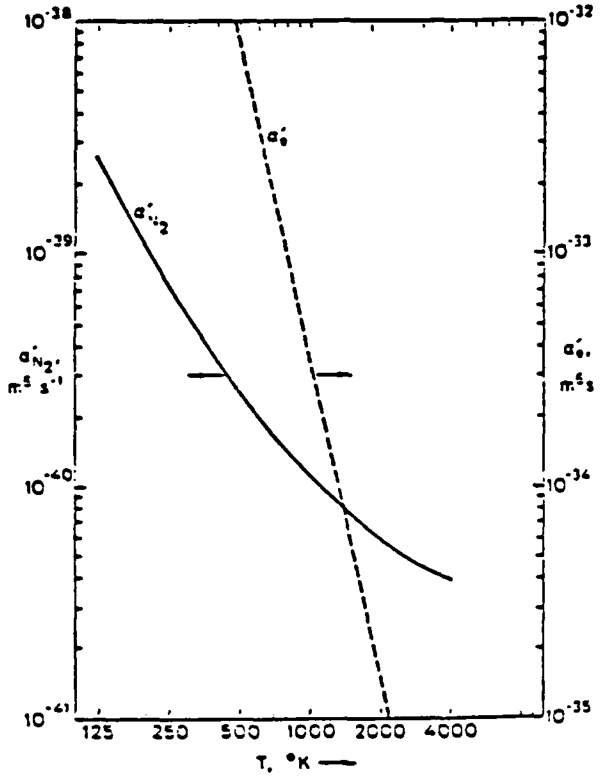

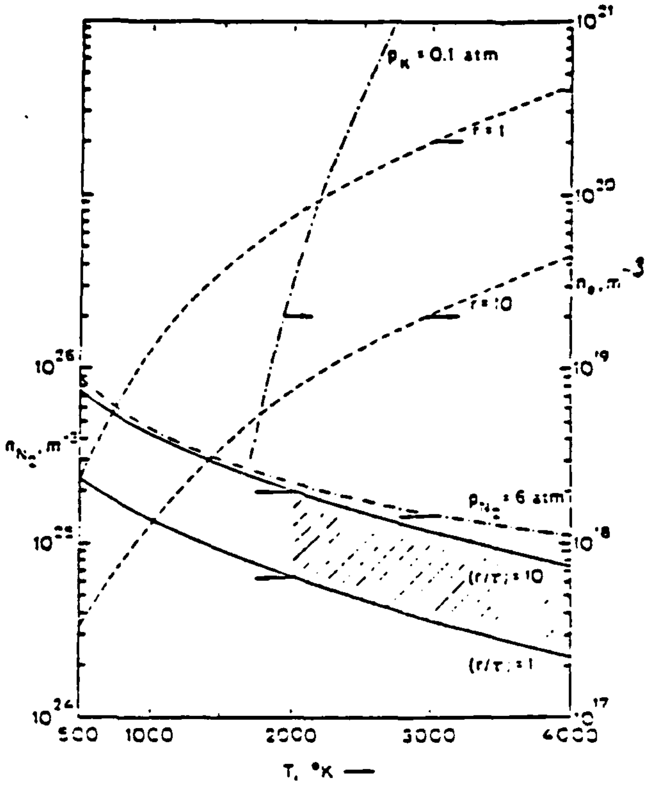

Fig. 1.3. Temperature dependence of the three-body recombination coefficients with either N_2 or electrons serving as the third body.

Fig. 1.4. Domain of experimental conditions required for determining the three-body recombination coefficient with N_2.

Before discussing some of the results of integrating the continuity equation for $n_e(x)$, it is useful to introduce two concepts that serve as a guide in selecting the initial condition at the entrance to the nozzle. We denote the ratio of the recombination rate by N_2 to that by electrons as $r \equiv n_{N_2}\alpha'_{N_2}/(n_e\alpha'_e)$, and the ratio of the characteristic time for recombination by N_2 to the residence time of a fluid element in the nozzle as $\tau \equiv t_{N_2}/t_{res}$. Here $t_{N_2} = (\alpha'_{N_2} n_{N_2} n_e)^{-1}$ and $t_{res} \approx L/a$, where L is the nozzle length and $a = (\gamma RT)^{1/2}$ is the speed of sound.

We would anticipate that desirable upstream gas states would satisfy the conditions $r > 1$ and $\tau \sim 1$. (For $\tau \ll 1$ the flow would approach the "equilibrium" limit, in which ionization and recombination rates are approximately equal. For $\tau \gg 1$ the flow would be approximately "frozen," where little recombination by N_2 occurs.) The condition on r would ensure that recombination rate by N_2 would exceed that by electrons.

From the equation defining r we may write

$$n_e = \frac{n_{N_2}\left(\alpha'_{N_2}/\alpha'_e\right)}{r} ,$$

and substituting for n_e in the equation defining τ, we obtain

$$n_{N_2} = \left[\left(\frac{r}{\tau}\right) \frac{(\alpha'_e/\alpha'_{N_2}}{\alpha'_{N_2}} 200 \sqrt{T}\right]^{1/2} .$$

(We have used here the approximate expression $t_{res} = 0.005/\sqrt{T}$, corresponding to a nozzle length of 0.1 m). Shown in Fig. 1.4 are the values of n_{N_2} plotted as a function of temperature for values of the parameter (r/τ) equal to 1 and 10, and the corresponding values of n_e for $r = 1$ and 10. Also shown are constant partial pressure lines for N_2 and K with $p_{N_2} = 6$ atm and $p_K = 0.1$ atm. These values are estimates of the approximate maximum values of the nitrogen and potassium partial pressures that can be used with the available experimental facilities.

The estimated range of possible experimental values for n_{N_2} and the temperature fall in the region defined by $T \gtrsim 2000$ K and by the curves labeled $(r/\tau) = 1$ and $p_{N_2} = 6$ atm. It appears that values of (r/τ) up to about 10 can be achieved.

To obtain a more accurate picture than is provided by the preceding analysis, a program was written to integrate the electron continuity equation numerically. The purpose of this program was to estimate the optimal experimental conditions that should be used for determining $\alpha'_{N_2}(T)$. The variation of n_e with streamwise location in a Mach 2 converging-diverging nozzle is shown in Figs. 1.5 and 1.6 for various representative values of the upstream stagnation conditions that may be achieved with the steady-state gas flow system presently available in the High Temperature Gasdynamics Laboratory. The operating characteristics of the arc jet heater in that system limit the N_2 partial pressure to about four atmospheres, or in equivalent terms $n_{N_2} \lesssim 10^{25}$ m^{-3} for a plenum temperature of 3000 K. (Figures 1.5a and 1.6b are for conditions which are somewhat more extreme.)

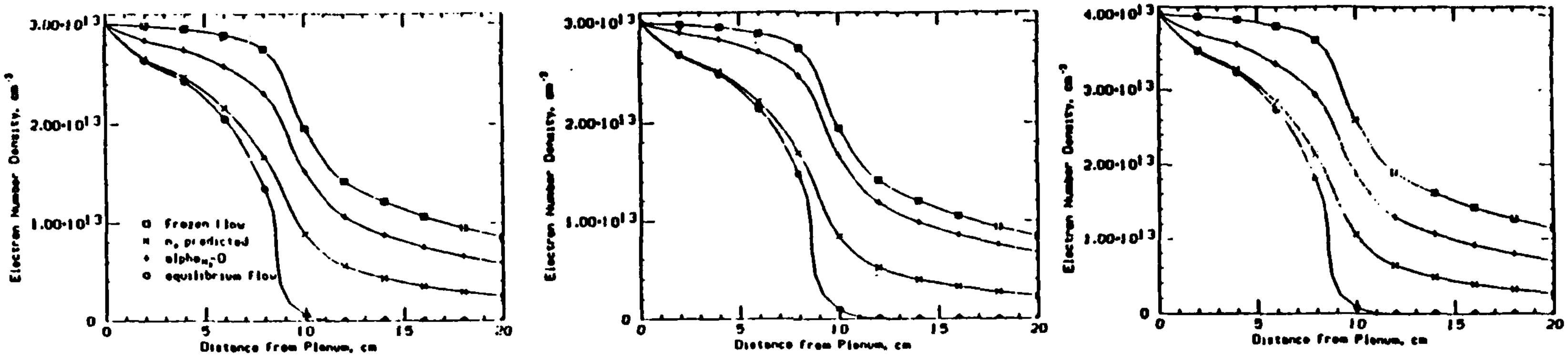

(a) $n_{N_2} = 10^{25} m^{-3}$, $n_e = 3\times10^{19} m^{-7}$
N_2 effect = 1.32

(b) $n_{N_2} = 2\times10^{25} m^{-3}$, $n_e = 3\times10^{19} m^{-3}$
N_2 effect = 1.86

(c) $n_{N_2} = 10^{25} m^{-3}$, $n_e = 4\times10^{19} m^{-3}$
N_2 effect = 1.57

Fig. 1.5. Variation of electron density through the nozzle for a stagnation temperature of 2000 K.

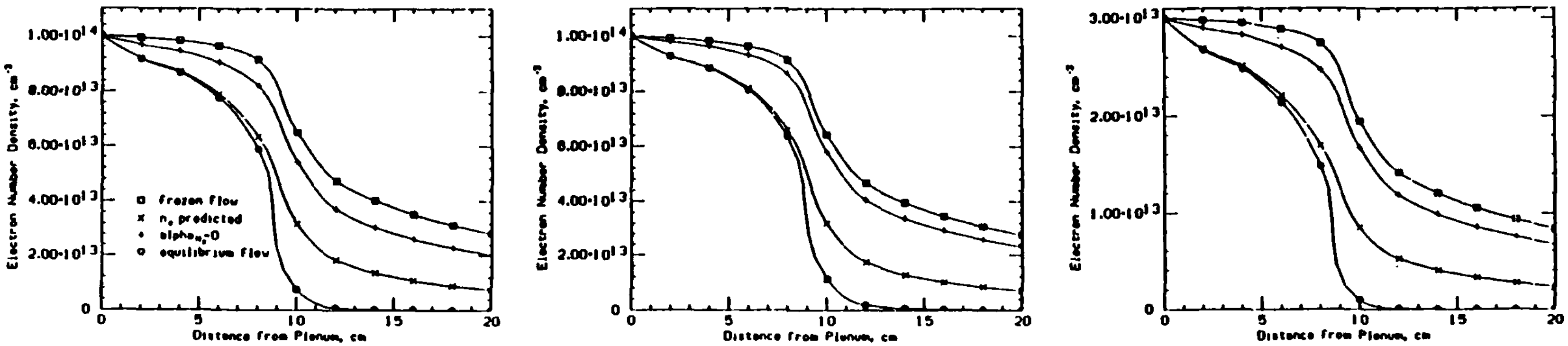

(a) $n_{N_2} = 10^{25} m^{-3}$, $n_e = 10^{20} m^{-3}$
N_2 effect = 1.70

(b) $n_{N_2} = 2\times10^{25} m^{-3}$, $n_e = 10^{20} m^{-3}$
N_2 effect = 2.26

(c) $n_{N_2} = 10^{25} m^{-3}$, $n_e = 4\times10^{-19} m^{-3}$
N_2 effect = 0.88

Fig. 1.6. Variation of electron density through the nozzle for a stagnation temperature of 3000 K.

The four curves in each figure show the "frozen" flow, the "equilibrium" flow, the recombining flow, and the contribution to the recombination by just the electron three-body process. Figures 1.5 and 1.6 are for stagnation temperatures of 2000 K and 3000 K respectively. With reference to Fig. 1.5a, Fig. 1.5b shows the effect of increasing n_{N_2}, and Fig. 1.5c shows the effect of increasing n_e. With reference to Fig. 1.6c, Fig. 1.6b shows the effect of increasing n_{N_2}, and Fig. 1.6c shows the effect of decreasing n_e. The term "N_2 effect" for each figure is the fractional decrease in n_e attributable to three-body recombination with N_2, that is, $[n_e(\alpha'_{N_2} = 0) - n_e]/n_e$. These results show that increasing the values of n_{N_2} and n_e are generally favorable and increasing T is unfavorable with respect to increasing the fractional effect of N_2.

A.1.3 Limitations of the Steady-State Experiment

It appears from Figs. 1.5 and 1.6 that in order for the value of n_e at the exit of the nozzle to depart significantly from the frozen value, it is necessary to have $\tau < 1$, but this requirement then precludes achieving the (desirable) condition $r \gtrsim 10$. If n_e is decreased so as to increase r, the value of τ is also increased, thereby reducing the effects of recombination relative to frozen flow. This behavior may be seen more clearly from the relation

$$\frac{r}{\tau} = \frac{(n_{N_2}\alpha'_{N_2})^2 t_{res}}{\alpha'_e}$$

obtained by combining the expressions for r and τ so as to eliminate n_e. For fixed N_2 partial pressure and nozzle dimensions, the right-hand side is a function only of the stagnation temperature. Taking $p_{N_2} = 4$ atm and $t_{res} = 0.005/\sqrt{T}$, one obtains $r/\tau = 5.4$ for T = 2000 K and $r/\tau = 7.2$ for T = 3000 K.

Another limitation of the rapid expansion experiment stems from the practial difficulties of providing optical access for diagnostic measurements of the expanding gas at more than a few axial locations (e.g., the plenum, the exit, and perhaps one intermediate position). Since the gas temperature decreases by approximately 1000 K from the upstream plenum to the downstream exit, the accuracy of determining the temperature dependence of $\alpha'_{N_2}(T)$ would be limited by the relatively coarse resolution with which the dependence on axial location of n_e could be measured. The use of the available arc jet introduces a further possible complication in that argon atoms will be present in the recombining plasma.

A.2 Pulsed Photoionization Approach

A.2.1 Experimental Configuration

An experimental system for producing a nonequilibrium recombining plasma using a pulsed photoionization approach is illustrated schematically in Fig. 1.7. The radiation source is a pulsed short arc Xe lamp directed along the axis of a tube containing the test gas (e.g., Cs vapor and N_2). The Cs vapor and N_2 are contained in a one-inch-diameter, twelve-inch-long Inconel tube fitted with sapphire windows. The Cs pressure is one to ten torr and the nitrogen pressure is about one atmosphere. An electric tube oven heats the Cs-N_2 mixture in the temperature

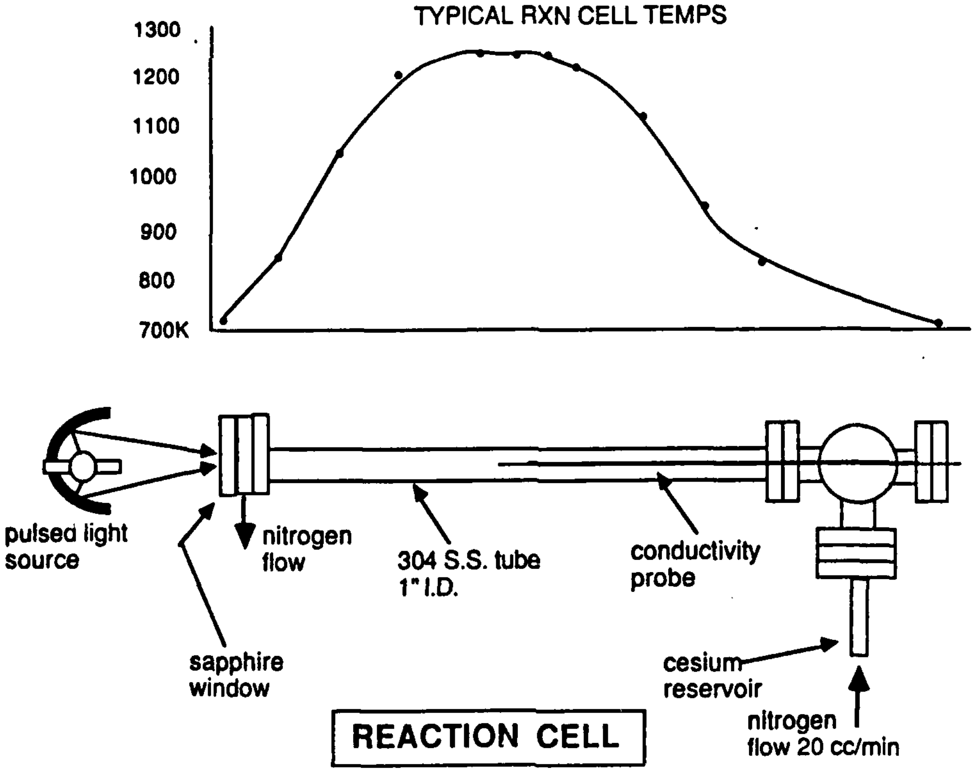
TYPICAL RXN CELL TEMPS
1300
1200
1100
1000
900
800
700K
pulsed light source
nitrogen flow
304 S.S. tube 1" I.D.
conductivity probe
sapphire window
cesium reservoir
nitrogen flow 20 cc/min
REACTION CELL

Fig. 1.7. Experimental system based on pulsed photoionization approach.

range 400 to 1200 K. A low flow rate of the gas mixture through the tube contributes to maintaining high gas purity. The sapphire window has 75% transmission of radiation down to 200 nm wavelengths so it is transparent to photons capable of singly ionizing ground state Cs atoms, i.e., $\lambda \leq 318$ nm, and opaque to photons capable of ionizing N_2, i.e., $\lambda \leq 200$ nm. The Xe flashlamp provides a 2-ms pulse of ionizing photons which is coupled to the Cs test cell through an ellipsoidal reflector.

nonequilibrium, isothermal Cs plasma is produced by the radiation pulse. The free electrons are rapidly thermalized through collisons with the N_2. As the electrons begin to recombine with Cs^+ in the presence of the nitrogen, the electron number density would be determined as a function of time. Possible methods for obtaining the electron density include measurements of the spectral emission from free-bound and high-lying bound-bound transitions in Cs, as well as measurements of the electrical conductivity using a four-pin conductivity probe. The time history of the electron number density is directly related to the rate coefficient for recombination on N_2.

Experimental conditions would be chosen so that the recombination on N_2 proceeds at a much greater rate than electron loss by recombination on electrons, or by diffusion of electrons to the test cell walls. Under such conditions $dn_e/dt = -\alpha'_{N_2} n_{N_2} n_e^2$, so that

$$\frac{1}{n_e} = \frac{1}{n_{eo}} + \alpha'_{N_2} n_{N_2} t \ .$$

Thus the slope of $1/n_e$ plotted vs time gives $\alpha_{N_2}(T)$ multiplied by the known concentration of N_2. The temperature dependence of $\alpha_{N_2}(T)$ is empirically determined by performing the experiment over the range of temperatures that can be achieved with the apparatus previously described.

The electron number densities corresponding to the parameter value $r = 10$ are given in Table 1.1. Also shown in the table are characteristic times for recombination on N_2, $t_{N_2} \sim (\alpha_{N_2} n_{N_2} n_e)^{-1}$, for electron diffusion to the walls, $t_{diff} \sim R^2/D_a \simeq KR^2 n_{N_2}/\sqrt{T}$, for the ionizing light pulse to decay from a peak to a minimum intensity, t_{pls}, and for thermalization of free electrons $t_{rlx} = [\nu_{e,N_2} \cdot 10 \cdot (2m_e/m_{N_2})]^{-1}$. Here

Table 1.1

Characterization of Pulsed Experiment

Temp, K	n_e, cm^{-3}	t_{N_2}, sec	t_{diff}, sec	t_{pls}, sec	t_{rlx}, sec
400	3×10^{10}	7×10^{-3}	0.9	1×10^{-4}	4×10^{-9}
600	7×10^{10}	8×10^{-3}	0.5	1×10^{-4}	4×10^{-9}
800	2×10^{11}	7×10^{-3}	0.3	1×10^{-4}	4×10^{-9}

$R \simeq 1$ cm is the radius of the test cell, D_a is the ambipolar diffusion coefficient, K is a constant that depends on atomic properties of Cs^+ and N_2 [1.7], ν_{e,N_2} is the average e,N_2 collision frequency [1.8], and $10\cdot(2m_e/m_{N_2})$ is the average fraction of electron kinetic energy lost in all collisions with N_2 [1.9]. A typical value for the flashlamp pulse forming network is used for t_{pls}.

Table 1.1 shows that the characteristic times are ordered as $t_{rlx} \ll t_{pls} < t_{N_2} \ll t_{diff}$, and therefore that the experimental conditions result in an isothermal plasma dominated by recombination on N_2. The degree of excitation of N_2 by encounters with photons or energetic electrons is negligible. The N_2 molecules do not significantly absorb photons with wavelengths greater than 200 nm [1.10]. The energy corresponding to an electron liberated from the Cs ground state by a 200 nm photon is 2.1 eV. To excite a ground state N_2 to its first vibrationally excited state requires approximately 0.22 eV [1.11], or each electron can excite at most 10 N_2 molecules. An estimate of the maximum fraction of N_2 molecules which could be excited in this manner is therefore $10\cdot n_e/n_{N_2} < 10^{-6}$.

A.2.2 Reaction Kinetics Model

In addition to processes (1.1) and (1.2), a loss of electrons under conditions of interest could also occur through a sequence of reactions involving fast formation of the ion cluster $Cs^+\cdot N_2$, fast two-body switching to form Cs_2^+, followed by dissociative recombination of the cesium dimer ion. These processes can be written as follows:

$$Cs^+ + N_2 + N_2 \longrightarrow Cs^+\cdot N_2 + N_2 \qquad (1.3a)$$

$$Cs^+\cdot N_2 + Cs \longrightarrow Cs_2^+ + N_2 \qquad (1.4a)$$

$$e + Cs_2^+ \longrightarrow Cs + Cs \qquad (1.5)$$

Reactions analogous to (1.3a) and (1.4a) can occur when water vapor impurities are present and H_2O replaces N_2 as a clustering partner. These reactions are written:

$$Cs^+ + H_2O + N_2 \longrightarrow Cs^+ \cdot H_2O + N_2 \qquad (1.3b)$$

$$Cs^+ \cdot H_2O + Cs \longrightarrow Cs_2^+ + H_2O \qquad (1.4b)$$

Other possible mechanisms of electron loss are electron dissociative recombination with $Cs^+ \cdot N_2$, electron attachment, and ion-ion recombination as represented respectively by the reactions

$$e + Cs^+ \cdot N_2 \longrightarrow Cs + N_2 \qquad (1.6)$$

$$e + Cs + N_2 \longrightarrow Cs^- + N_2 \qquad (1.7)$$

$$Cs^- + Cs^+ \longrightarrow 2Cs \qquad (1.8)$$

In what follows, we present a detailed examination of the overall recombination process that includes both the ion-molecule reaction channel (1.3), (1.4), and (1.5) as well as the three-body processes (1.1 and 1.2). Using estimates of the recombination rate coefficients and equilibrium constants (to calculate the backward rates) constructed from available information in the literature (see Table 1.2 for references), we show that experimental conditions at higher temperatures can be chosen to maintain process (1.2) as the dominant electron loss mechanism, despite the fast reactions (1.3) and (1.4). Later we show that inclusion of reactions (1.6)-(1.8) does not affect the dominance of reaction (1.2) in electron loss frequency. In addition we also show that by using a liquid nitrogen cold trap and because of the gettering action of Cs, as well as from considerations of the reaction kinetics, the deleterious effects of a possible water impurity are not significant.

a. Partial Equilibrium

Although reactions (1.3) and (1.4) proceed in a forward direction rapidly relative to the three other reactions considered, the backward rates for these reactions are also large. Reactions (1.3) and (1.4) are able to quickly reach a partial equilibrium condition, where the forward

Table 1.2

Reaction Rate and Equilibrium Constants

Reaction	Constants	References
	$k_1 = 1.09\times10^{-8}/T^{4.5}\ \mathrm{cm}^6/\mathrm{s}$	
$e + Cs^+ + e \underset{k_{-1}}{\overset{k_1}{\rightleftarrows}} Cs + e$	$k_{-1} = 2.64\times10^{7}/T^3{*}\exp(-45128/T)\ \mathrm{cm}^3/\mathrm{s}$	1.5, 1.1
	$k_1/k_{-1} = 4.13\times10^{-16}{*}T^{-1.5}{*}\exp(45128/T)\ \mathrm{cm}^3$	
	$k_2 = 6.58\times10^{-29}{*}\exp(590.4/T)\ \mathrm{cm}^6/\mathrm{s}$	
$e + Cs^+ + N_2 \underset{k_{-2}}{\overset{k_2}{\rightleftarrows}} Cs + N_2$	$k_{-2} = 1.59\times10^{-13}{*}T^{1.5}{*}\exp(-44538/T)\ \mathrm{cm}^3/\mathrm{s}$	1.2, 1.1
	$k_2/k_{-2} = 4.13\times10^{-16}{*}T^{-1.5}{*}\exp(45128/T)\ \mathrm{cm}^3$	
	$k_{3a} = 6.42\times10^{-10}\ \mathrm{cm}^3/\mathrm{s}$	1.19, 1.20, 1.22
$Cs^+ + N_2 + N_2 \underset{k_{-3a}}{\overset{k_{3a}}{\rightleftarrows}} Cs^+ N_2 + N_2$	$k_{-3a} = 7.81\times10^{18}{*}T^{-1.5}{*}\exp(-3374/T)\ \mathrm{s}^{-1}$	1.14, 1.15, 1.16
	$k_{3a}/k_{-3a} = 8.22\times10^{-29}{*}T^{1.5}{*}\exp(3374/T)\ \mathrm{cm}^3$	1.12, 1.26, 1.18
	$k_{3b} = 6.42\times10^{-10}\ \mathrm{cm}^3/\mathrm{s}$	
$Cs^+ + H_2O + N_2 \underset{k_{-3b}}{\overset{k_{3b}}{\rightleftarrows}} Cs^+ H_2O + N_2$	$k_{-3b} = 2.44\times10^{18}/T{*}\exp(-7049/T)\ \mathrm{s}^{-1}$	1.20, 1.13, 1.24
	$k_{3b}/k_{-3b} = 2.63\times10^{-28}{*}T{*}\exp(7049/T)\ \mathrm{cm}^3$	1.17
	$k_{4a} = 10^{-9}\ \mathrm{cm}^3/\mathrm{s}$	
$Cs^+ N_2 + Cs \underset{k_{-4a}}{\overset{k_{4a}}{\rightleftarrows}} Cs_2^+ + N_2$	$k_{-4a} = \exp(-1.081\times10^{4}/T - 23.97 + 8.303\times10^{-4}{*}T - 1.496\times10^{-7}{*}T^2)\ \mathrm{cm}^3/\mathrm{s}$	1.21, 1.13, 1.24
	$k_{4a}/k_{-4a} = \exp(1.081\times10^{4}/T + 3.244 - 8.303\times10^{-4}{*}T + 1.496\times10^{-7}{*}T^2)$	

Table 1.2 cont.

Table 1.2 (cont.)

Reaction	Constants	References
$Cs^+ H_2O + Cs \underset{k_{-4b}}{\overset{k_{4b}}{\rightleftharpoons}} Cs_2^+ + H_2O$	$k_{4b} = 10^{-9}$ cm^3/s $k_{-4b} = \exp(-7.134\times10^3/T - 23.39 + 8.525\times10^{-4}*T - 1.559\times10^{-7}*T^2)$ cm^3/s $k_{4b}/k_{-4b} = \exp(7.134\times10^3/T + 2.668 - 8.525\times10^{-4}*T + 1.559\times10^{-7}*T^2)$	1.21, 1.23, 1.24
$e + Cs_2^+ \underset{k_{-5}}{\overset{k_5}{\rightleftharpoons}} Cs + Cs$	$k_5 = 10^{-8}*(300/T)^{1/2}$ cm^3/s $k_{-5} = \exp(-3.09\times10^4/T + 2.5*\ell n(T) - 41.57 - 8.303\times10^{-4}*T + 1.496\times10^{-7}*T^2)$ cm^3/s $k_5/k_{-5} = \exp(3.094\times10^4/T - 3*\ell n(T) + 26.00 + 8.303\times10^{-4}*T - 1.496\times10^{-7}*T^2)$	1.25, 1.26
$e + Cs^+ N_2 \underset{k_{-6}}{\overset{k_6}{\rightleftharpoons}} Cs + N_2$	$k_6 = 5.0\times10^{-7}*(300.0/T)^{1.5}$ cm^3/s $k_{-6} = 5.2\times10^{16}*T^{1.5}*\exp(-41754./T)$ cm^3/s $k_6/k_{-6} = 5.02\times10^{12}*T^{-3}*\exp(41754./T)$	1.26
$e + Cs + N_2 \underset{k_{-7}}{\overset{k_7}{\rightleftharpoons}} Cs^- + N_2$	$k_7 = 8.2\times10^{-14}$ cm^3/s $k_{-7} = 1.98\times10^2*T^{1.5}*\exp(-5452.1/T)$ 1/s $k_7/k_{-7} = 4.14\times10^{-16}*T^{-1.5}*\exp(5452.1/T)$ cm^3	1.27 (high-pressure limit)
$Cs^- + Cs^+ \underset{k_{-8}}{\overset{k_8}{\rightleftharpoons}} Cs + Cs$	$k_8 = 2.0\times10^{-7}*300/T$ cm^3/s $k_{-8} = 2.0\times10^{-7}*300/T*\exp(-39673/T)$ cm^3/s $k_8/k_{-8} = \exp(39673/T)$	1.15, 1.28, 1.29

and backward rate are equal in magnitude. This partial equilibrium is maintained while the recombination reactions slowly change the ion and electron concentrations.

Table 1.2 lists the preceding ten chemical reactions. Also listed are the values of the corresponding forward and backward rate constants and the ratios of these two constants (i.e., the equilibrium constants), used in all subsequent calculations. The constants were obtained using the references shown. The photoionization of Cs vapor by ultraviolet radiation from a flashlamp can be represented by the reaction

$$Cs + h\nu \xrightarrow{k_\nu} Cs^+ + e \ .$$

The photon flux is modeled as a rectangular function in time, and the Cs vapor can be shown to be optically thin. Under these conditions the rate of increase of the electron number density can be represented by $d[e]/dt = [Cs]k_\nu$ where k_ν is the integral over wavelength of the product of the photon flux and the total photoionization cross section. The value for k_ν used in these calculations is 1.0 sec^{-1}. This value corresponds to a photon flux (wavelengths < 318 nm) of about 10^{20} photons/$cm^2 \cdot sec$, which is an estimate of the flux attainable with our pulsed short arc flashlamp system.

Shown in Figs. 1.8a, 1.9a, and 1.10a are the time histories of the number densities of the species of interest for three different test cell temperatures. The $Cs^+ \cdot H_2O$ species occurs in concentrations which are off the lower end of the plotted scale. This species is treated explicitly in the section on impurities. (Note that reactions (1.6)-(1.8) are not modeled in the results presented in these figures.) It is assumed that the flashlamp is energized at $t = 0$ and it is extinguished at $t = 1$ ms; the dynamic relaxation of the nonequilibrium plasma occurs for times $t > 1$ ms. These plots were made by numerically solving the set of differential equations which describe the kinetics of the species involved in reactions (1.1) through (1.5). For $t < 0$, the plasma is in a state of local thermodynamic equilibrium. The equilibrium species concentrations shown in the figures are determined by the Cs vapor pressure (controlled by the reservoir temperature), by the initial

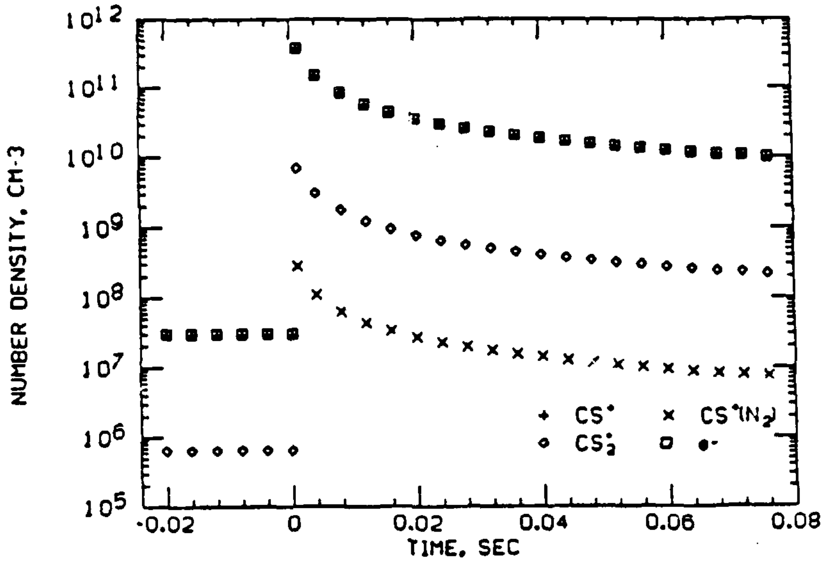

Fig. 1.8a. Species concentrations from numerical solution of kinetics equations for reactions (1.1)-(1.5). T = 1000 K; [Cs] = 4.5×10^{14} cm^{-3}; [N_2] = 10^{19} cm^{-3}; [H_2O] = 10^{13} cm^{-3}. Two distinct regimes are shown: t < 0, complete equilibrium; t > 1 ms, plasma relaxation. Photoionization occurs between these regimes.

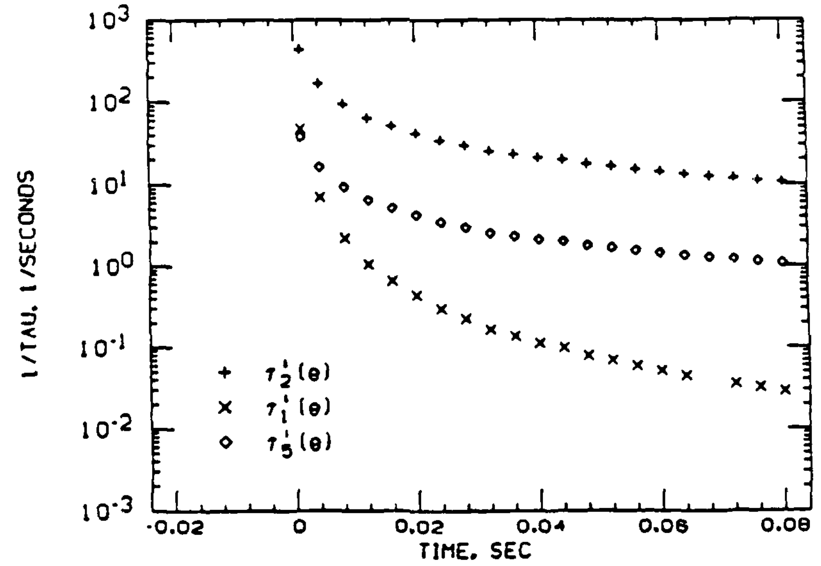

Fig. 1.8b. Electron loss frequencies from numerical solution of kinetics equations for reactions (1.1)-(1.5). T = 1000 K; [Cs] = 4.5×10^{14} cm^{-3}; [N_2] = 10^{19}; [H_2O] = 10^{13} cm^{-3}. $1/\tau_i^{\downarrow}(e) \equiv$ (net electron loss rate)/[e]. For ambipolar diffusion, $1/\tau_{diff}^{\downarrow}(e) \lesssim 10$ sec^{-1}.

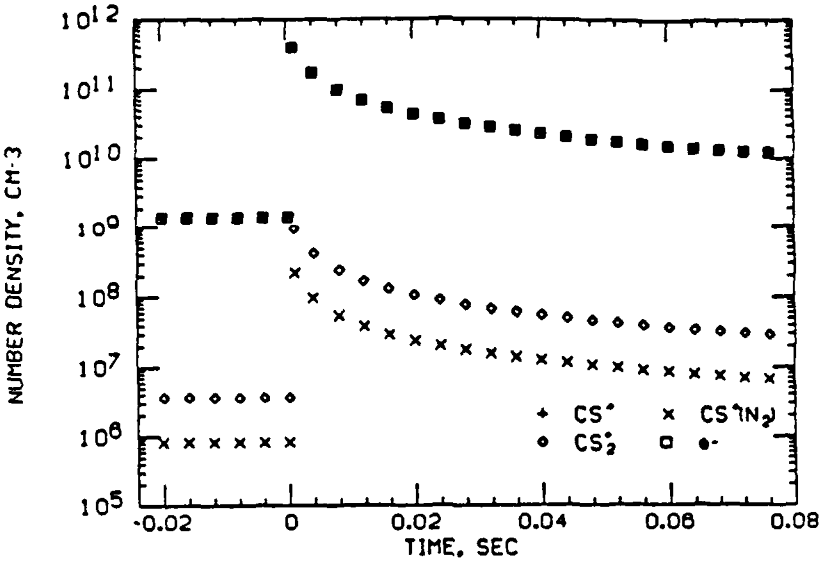

Fig. 1.9a. Species concentrations from numerical solution of kinetics equations for reactions (1.1)-(1.5). T = 1200 K; [Cs] = 4.5×10^{14} cm^{-3}; $[N_2]$ = 10^{19} cm^{-3}; $[H_2O]$ = 10^{13} cm^{-3}. Two distinct regimes are shown: t < 0, complete equilibrium; t > 1 ms, plasma relaxation. Photoionization occurs between these regimes.

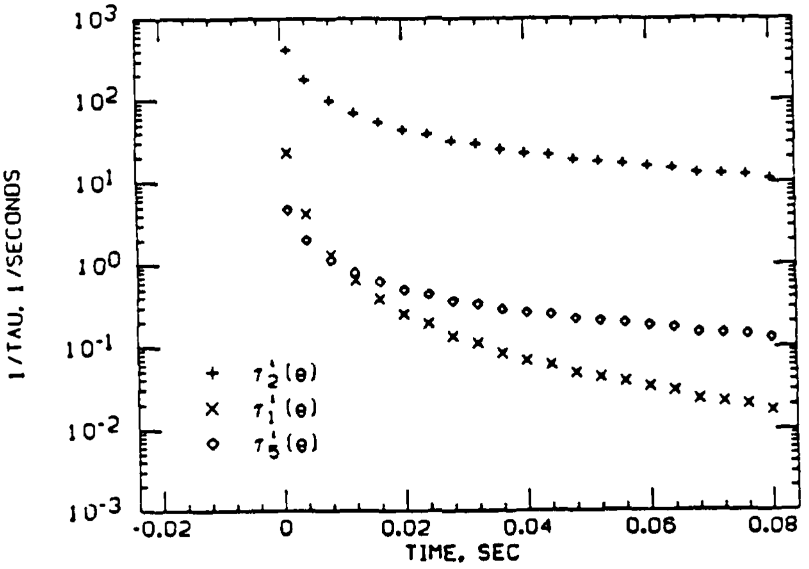

Fig. 1.9b. Electron loss frequencies from numerical solution of kinetics equations for reactions (1.1)-(1.5). T = 1200 K; [Cs] = 4.5×10^{14} cm^{-3}; $[N_2]$ = 10^{19}; $[H_2O]$ = 10^{13} cm^{-3}. $1/\tau_i^{\downarrow}(e) \equiv$ (net electron loss rate)/[e]. For ambipolar diffusion, $1/\tau_{diff}^{\downarrow}(e) \lesssim 10\ sec^{-1}$.

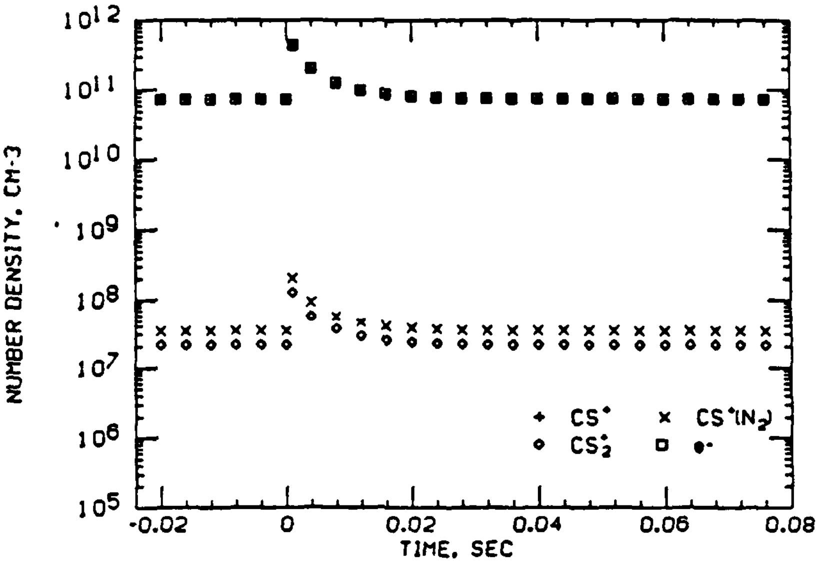

Fig. 1.10a. Species concentrations from numerical solution of kinetics equations for reactions (1.1)-(1.5). T = 1500 K; [Cs] = 4.5×10^{14} cm^{-3}; $[N_2]$ = 10^{19} cm^{-3}; $[H_2O]$ = 10^{13} cm^{-3}. Two distinct regimes are shown: t < 0, complete equilibrium; t > 1 ms, plasma relaxation. Photoionization occurs between these regimes.

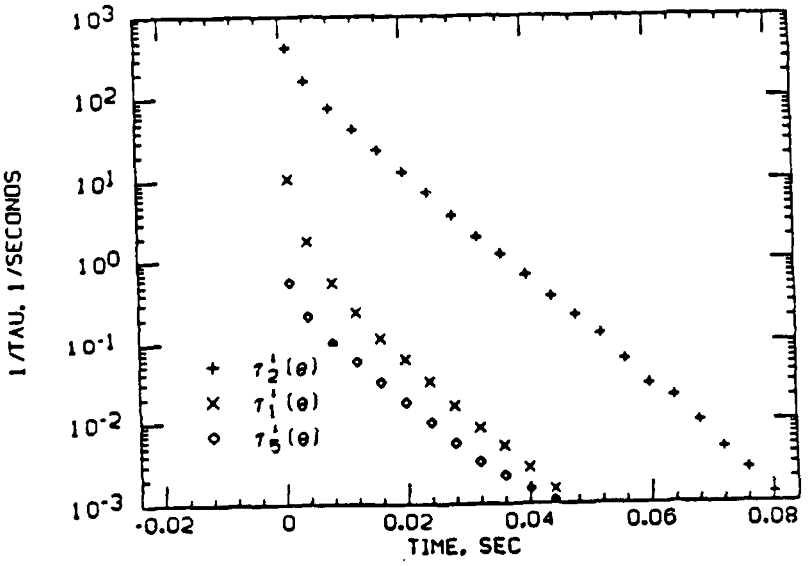

Fig. 1.10b. Electron loss frequencies from numerical solution of kinetics equations for reactions (1.1)-(1.5). T = 1500 K; [Cs] = 4.5×10^{14} cm^{-3}; $[N_2]$ = 10^{19}; $[H_2O]$ = 10^{13} cm^{-3}. $1/\tau_i^{\downarrow}(e) \equiv$ (net electron loss rate)/[e]. For ambipolar diffusion, $1/\tau_{diff}^{\downarrow}(e) \lesssim 10\ sec^{-1}$.

N_2 concentration, and by the temperature of the reaction chamber. Typical values for these quantities were taken to be $[Cs] = 4.5\times10^{14}\ cm^{-3}$, $[N_2] = 10^{19}\ cm^{-3}$, $[H_2O] = 10^{13}\ cm^{-3}$, and $600\ K < T < 1500\ K$.

For a general reaction i where

$$A + B \xrightarrow{k_i} C + D$$

we can obtain order-of-magnitude estimates of the characteristic times for significant decrease or increase of concentration of species respectively by, for example, $\tau_i^{\downarrow}(A) \sim (k_i[B])^{-1}$, or $\tau_i^{\uparrow}(C) \sim [C](k_i[A][B])^{-1}$. In what follows, it is shown how relations such as these may be employed to illustrate the essential physics underlying the numerical solutions presented in Figs. 1.8a, 1.9a, and 1.10a. Impurity reactions (1.3b) and (1.4b) have been included in the numerical solutions shown in Figs. 1.8-1.10, but an explanation of the effect of including these reactions is deferred until the section on impurities.

Using the equilibrium concentrations for t < 0 shown in Fig. 1.9a, characteristic times for significant changes in species concentrations are calculated in Table 1.3, for a temperature of 1200 K. Considering the

Table 1.3

Characteristic Times
t = 0, T = 1200 K, Species Concentrations from Fig. 1.9a

τ_p	duration $= 10^{-3}$ sec
$\tau_2^{\downarrow}(e)$	$= ([Cs^+]\bullet[N_2]\bullet k_2)^{-1} = (10^9\bullet10^{19}\bullet10^{-28})^{-1} = 1$ sec
$\tau_5^{\downarrow}(e)$	$= ([Cs_2^+]\bullet k_5)^{-1} = (3\times10^6\bullet5\times10^{-9})^{-1} \simeq 10^2$ sec
$\tau_1^{\downarrow}(e)$	$= ([Cs^+]\bullet[e]\bullet k_1)^{-1} = (10^9\bullet10^9\bullet10^{-22})^{-1} = 10^4$ sec
$\tau_{3a}^{\downarrow}(Cs^+)$	$= ([N_2]\bullet k_{3a})^{-1} = (10^{19}\bullet6\times10^{-10})^{-1} \simeq 10^{-9}$ sec
$\tau_2^{\downarrow}(Cs^+)$	$= ([e]\bullet[N_2]\bullet k_2)^{-1} = (10^9\bullet10^{19}\bullet10^{-28})^{-1} = 1$ sec
$\tau_{4a}^{\uparrow}(Cs_2^+)$	$= [Cs_2^+]/([Cs^+\bullet N_2]\bullet[Cs]\bullet k_{4a})$
	$= 3\times10^6/(8\times10^5\bullet5\times10^{14}\bullet10^{-9}) \simeq 10^{-5}$ sec
$\tau_5^{\downarrow}(Cs_2^+)$	$= ([e]\bullet k_5)^{-1} = (10^9\bullet5\times10^{-9})^{-1} \simeq 1$ sec

important reactions affecting the electron concentration, the ordering $\tau_{pulse} = 10^{-3}$ sec $<< \tau_1^{\downarrow} < \tau_5^{\downarrow} < \tau_2^{\downarrow}$ demonstrates that the duration of the photoionization reaction (one millisecond) is sufficiently short to throw the plasma out of equilibrium. The recombination reactions (1.1), (1.2), and (1.5) will not affect the change in ion and electron concentrations during and immediately after the flash because these reactions deplete charged particle concentrations in a characteristic time which is much longer than the pulse duration.

The orderings $\tau_{3a}^{\downarrow}(Cs^+) << \tau_2^{\downarrow}(Cs^+)$ and $\tau_{4a}^{\uparrow}(Cs_2^+) << \tau_5^{\downarrow}(Cs_2^+)$ [note that these τ's are calculated at equilibrium where, for any species s, $\tau_i^{\downarrow}(s) = \tau_i^{\uparrow}(s)$] indicate that reactions (1.3a) and (1.4a) will proceed to establish partial equilibrium concentrations of $Cs^+ \cdot N_2$ and Cs_2^+ while the recombination reactions change the ion and electron concentrations relatively slowly.

This partial equilibrium is embodied in the relations

$$\frac{[Cs^+ \cdot N_2]}{[Cs^+][N_2]} = \frac{k_{3a}}{k_{-3a}} \qquad (1.9)$$

and

$$\frac{[Cs_2^+]}{[Cs][Cs^+]} = \frac{k_{4a}}{k_{-4a}} \cdot \frac{k_{3a}}{k_{-3a}} \; . \qquad (1.10)$$

Equilibrium relation (1.10) corresponds to the reaction $Cs_2^+ \longrightarrow Cs + Cs^+$ obtained by adding reactions (1.3a) and (1.4a). Once reactions (1.3a) and (1.4a) are shown to be fast enough to maintain partial equilibrium, the equilibrium relations need not correspond directly to the reaction channel. Relations (1.9) and (1.10) have been chosen to express the equilibrium condition in order to illustrate that the equilibrium concentrations of Cs_2^+ and $Cs^+ \cdot N_2$ are approximately decoupled.

Since N_2 and Cs are present in much larger quantities than Cs^+, Cs_2^+, or $Cs^+ \cdot N_2$ (as can be justified by the results of the calculation being described), the following major species relations can be written:

$$[N_2] = \text{constant} = 10^{19} \text{ cm}^{-3} \; , \qquad (1.11)$$

and

$$[Cs] = \text{constant} = 4.5\times10^{14}\ \text{cm}^{-3}\ . \qquad (1.12)$$

From eqs. (1.9) and (1.11) and Table 1.2, the ratio $[Cs^+\cdot N_2]/[Cs^+] = [N_2]\cdot k_{3a}/k_{-3a}$ can be shown to be less than 1% at all temperatures greater than 500 K. Additionally, it has been shown that the recombination reactions are too slow to significantly affect charge concentration during the flash. Neglecting the $Cs^+\cdot N_2$ concentration and the effects of recombination, charge conservation during the flash can be written

$$[Cs^+] + [Cs_2^+] = [+]\ , \qquad (1.13)$$

where [+] denotes the concentration of positive (or negative) charge produced by the photoionization process. The charge produced by the flash is

$$[+] = [Cs]\cdot k_6\cdot \Delta t = 4.5\times10^{14}\cdot 1\cdot 10^{-3} = 4.5\times10^{11}\ \text{cm}^{-3}\ . \qquad (1.14)$$

Equations (1.10), (1.12), (1.13), and (1.14) are sufficient to determine equilibrium concentrations of Cs_2^+ and Cs^+; the value for $[Cs^+]$ can then be used with eqs. (1.9) and (1.11) to determine the $Cs^+\cdot N_2$ concentration. The species concentrations obtained in this way are shown by the curves plotted in Fig. 1.11, and compare well with the results of the numerical solution at t = 1 ms which have been plotted as individual points over these curves. The results shown in Fig. 1.11 can be used to predict the relative rates of the recombination reactions which follow the flash.

b. Characteristic Times for Recombination

Shown in Fig. 1.12 are the characteristic reciprocal times $1/\tau$ for significant electron recombination by each of the processes (1.1), (1.2), and (1.5), at t = 1 ms, immediately following termination of the flash. The quantity $1/\tau$ is a measure of the frequency of electron loss via a given recombination reaction. The continuous curves were calculated using the formulas shown in Table 1.3 evaluated for the concentrations given in Fig. 1.11. At temperatures above 1000 K, reaction (1.2) is clearly the dominant loss mechanism immediately after the flash.

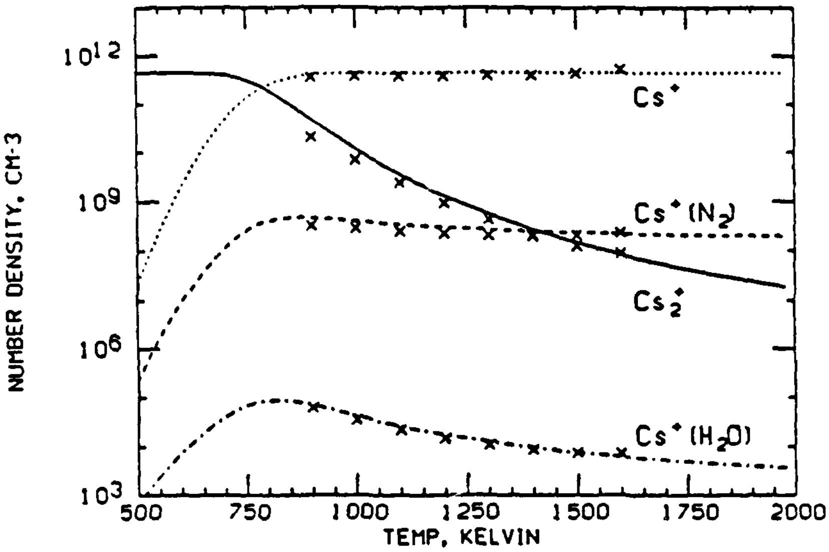

Fig. 1.11. Partial equilibrium species concentrations at t = 1 ms (immediately after photoionization). Continuous lines correspond to analytical solution of eqs. (1.10)-(1.16); discrete points correspond to numerical solutions of kinetics equations as in Figs. 1.8-1.10.

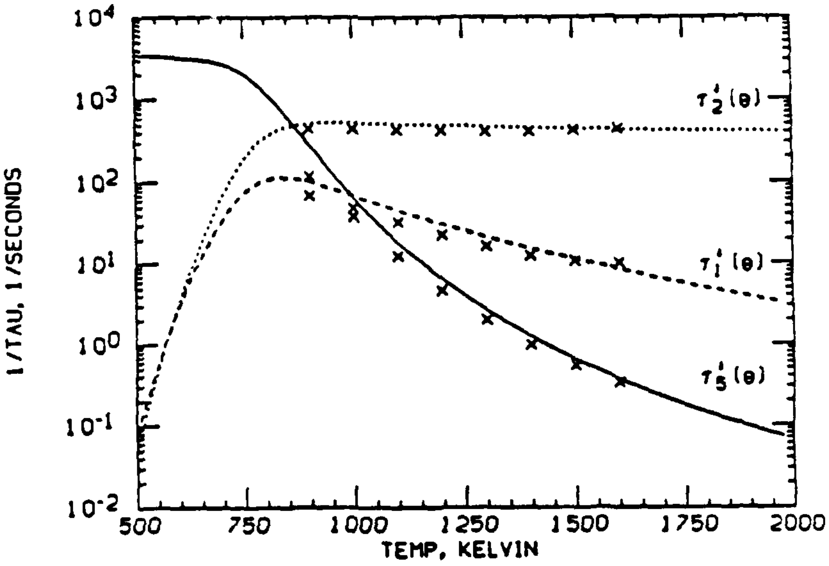

Fig. 1.12. Electron loss frequencies at t = 1 ms (immediately after photoionization). Continuous lines correspond to the formulas of Table 1.2 and the concentrations of Fig. 1.11. Discrete points correspond to numerical solutions as in Figs. 1.8-1.10. For ambipolar diffusion, $1/\tau_{diff}^{\downarrow}(e) \gtrsim 10\ s^{-1}$.

The numerical solutions shown in Figs. 1.8b, 1.9b, and 1.10b give detailed information about electron loss mechanisms for extended times after the flash. These plots correspond in temperature and time to Figs. 1.8a, 1.9a, and 1.10a. The frequency of electron loss by reaction i,

$$\frac{1}{\tau_i^{\downarrow}(e)} = \frac{(\text{forward - backward reaction rate})}{[e]}$$

is shown for recombination reactions (1.1), (1.2), and (1.5) during plasma relaxation. The net reaction rate (forward - backward rate) must be considered for $t > 1$ ms when the reactions can approach equilibrium. At $t = 1$ ms the net rate and forward rate are approximately equal. Generally the electron concentration and the net reaction rate change with time, so that this frequency is usually time dependent.

A recombination reaction is considered to be the dominant electron loss mechanism when its electron loss frequency exceeds the frequencies of all other competing loss mechanisms. If measurement of electron concentration decay is to be useful in determining the rate of reaction (1.2), experimental conditions must be chosen so that reaction (1.2) is the dominant electron loss mechanism. For all temperatures greater than 1000 K, and all times shown, reaction (1.2) dominates reactions (1.1) and (1.5) in electron loss. The electron loss frequency due to ambipolar diffusion, $1/\tau^{\downarrow}_{diff}(e)$, (at about 1200 K and one atmosphere of N_2) is approximately constant at 10 sec^{-1}. As the electron concentration decays with time, $1/\tau^{\downarrow}_{2}(e)$ decreases because the reactions move toward an equilibrium balance where the forward and backward rates are equal. Electron concentration measurements are only useful while the resulting reduced electron loss frequency remains larger than $1/\tau^{\downarrow}_{diff}(e)$. Hence for the conditions of Figs. 1.8-1.10 electron concentration measurements should be made in approximately the first 10 ms of recombination. Electron loss frequencies at 1 ms, which are taken from numerical solutions similar to those shown in Figs. 1.8b, 1.9b, and 1.10b, are plotted as discrete points with the analytical solution shown in Fig. 1.12. Both solutions agree that at temperatures above 1000 K, during the first 10 ms after photoionization, measurement of electron concentration decay will provide direct information about reaction (1.2).

Reaction 1.6 competes directly with reaction 1.2 for electrons, but the electron loss frequency can be expected to be low due to its dependence on the low concentration of $Cs^+ \cdot N_2$. Reactions 1.7 and 1.8 together constitute a channel for electron loss via recombination with Cs^+. These three reactions have been included in an extended computer model of the kinetics. The results of the numerical calculation of concentrations and electron loss frequencies based on reactions (1.1)-(1.8) are shown in Figs. 1.13a and 1.13b (and can be compared with Fig. 1.9). Figure 1.13b indicates that reactions (1.6) and (1.7) are significant secondary electron loss mechanisms, but the primary electron loss mechanism remains reaction (1.2). Measurement of the rate of electron concentration decay will be a valid indication of the rate of reaction (1.2).

c. Impurities

The species Cs, Cs^+, e, and N_2 are necessary for the experiment; other chemical species which may be formed from these cannot be avoided. In addition, the presence in the test cell of impurities due to outgassing or impure reactant gases must be considered. Impurity concentrations can easily be kept small enough to ensure that N_2 is the dominant neutral partner in all reactions, but small amounts of radical species could substantially affect ion-molecule chemistry.

Water vapor is, of all impurities, most likely to be both sufficiently reactive and plentiful to have a significant effect. The amount of H_2O present in the N_2 charge will be minimized by passing the gas through a liquid nitrogen trap. The partial pressure of the H_2O will roughly correspond to the vapor pressure at 100 K, $P_v \sim 10^{-10}$ torr [1.30]. At 300 K this pressure corresponds to $[H_2O] = 5\times10^6$ cm^{-3}. For a baked and pumped metal system a typical outgassing rate is 10^{-10} torr•liter/sec•cm^2 [1.31]. Assuming H_2O is a major constituent of the outgas and using design dimensions of the test cell with a period of about 30 hours between the end of pumping and the end of the experiment, $P_{H_2O} = 10^{-10}(\text{torr}\cdot\text{liter/sec}\cdot\text{cm}^2)\cdot 60\ \text{cm}^2\cdot 10^5\ \text{sec}/1\ \text{liter} = 6\times10^{-4}$ torr. At 300 K this pressure corresponds to $[H_2O] = 2\times10^{13}$ cm^{-3}. For one atmosphere of N_2 this H_2O concentration corresponds to an impurity level

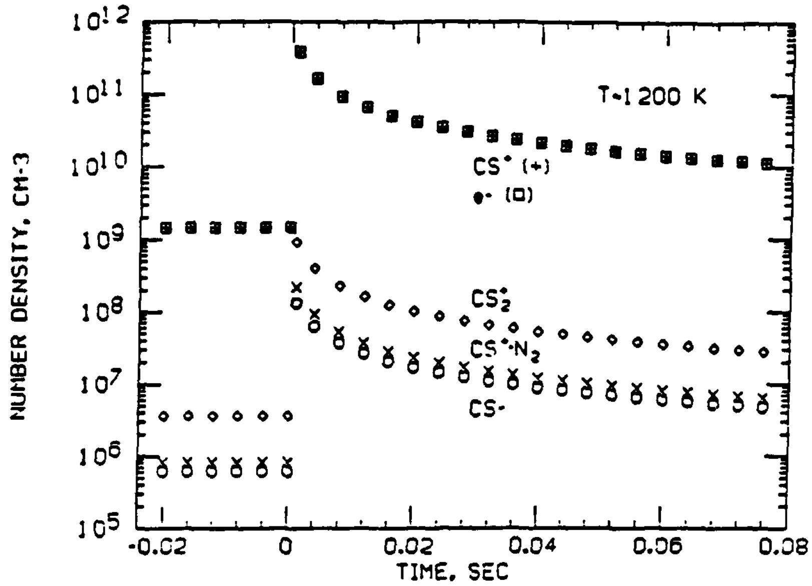

Fig. 1.13a. Species concentrations from numerical solution of kinetics equations for reactions (1.1)-(1.8). T = 1200 K. The following initial species concentrations remain roughly constant: [Cs] = 4.5×10^{14} cm^{-3}; $[N_2]$ = 10^{19} cm^{-3}; $[H_2O]$ = 10^{13} cm^{-3}. Two distinct regimes are shown: t < 0, complete equilibrium; t > 1 ms, plasma relaxation. Photoionization occurs between these regimes.

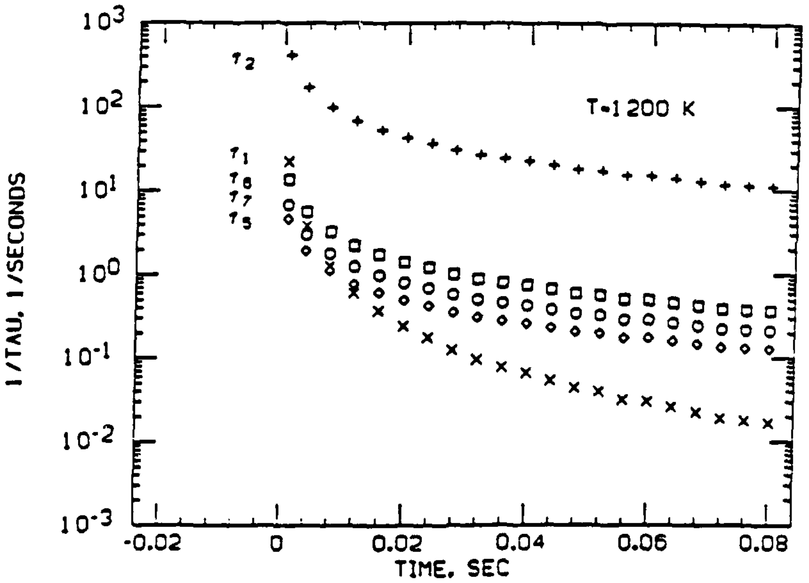

Fig. 1.13b. Electron loss frequencies from numerical solution of kinetics equations for reactions (1.1)-(1.8). T = 1200 K. The following initial species concentrations remain roughly constant: [Cs] = 4.5×10^{14} cm^{-3}; $[N_2]$ = 10^{19}; $[H_2O]$ = 10^{13} cm^{-3}. $1/\tau_i \equiv (d[e]/dt)_i/[e]$.

of one part per million. However, the water present will be very effectively scavenged by reducing reactions with Cs vapor. A reduction in H_2O concentration by a factor of 300 has been achieved by introducing Cs vapor into a 10^{-5} torr vacuum [1.32]. In light of scavenging $[H_2O] = 10^{13}\ cm^{-3}$ appears to be a conservative worst-case estimate.

Even assuming an amount of water vapor impurity equal to this worst-case estimate, it can be shown that ion-molecule chemistry of water vapor in the plasma will not interfere with the primary experimental goal of measuring the rate of reaction (1.2). The association and switching reactions (1.3) and (1.4) can occur with N_2 replaced by H_2O; related bond energies are $E_{Cs^+ \cdot N_2} \approx 6.7$ kcal/mol [1.12], and $E_{Cs^+ \cdot H_2O} = 13.7$ kcal/mol [1.13]. In relation to the measurement of the rate of reaction (1.2), reactions (1.3) and (1.4) provide a channel for the production of Cs_2^+ (which subsequently dissociatively recombines) and a loss mechanism for Cs^+. It has been shown for the relatively fast reactions involving the $Cs^+ \cdot N_2$ cluster that a partial equilibrium calculation can be used to determine species concentrations before recombination begins. Partial equilibrium represents a worst case since it allows the greatest advancement down the reaction channel which produces Cs_2^+ prior to the onset of recombination. Partial equilibrium may therefore be conservatively assumed for the reactions involving the $Cs^+ \cdot H_2O$ cluster in a calculation which is analogous to the $Cs^+ \cdot N_2$ partial equilibrium computation. Agreement between analytical and numerical solutions for $Cs^+ \cdot H_2O$ concentration in Fig. 1.11 supports the validity of the partial equilibrium assumption. For equilibrium involving $Cs^+ \cdot H_2O$ the governing equations are (1.10), (1.12), (1.13), (1.14),

$$\frac{[Cs^+ \cdot H_2O]}{[Cs^+][H_2O]} = \frac{k_{3b}}{k_{-3b}} \tag{1.15}$$

and

$$[H_2O] = \text{constant} = 10^{13}\ cm^{-3} . \tag{1.16}$$

Equation (1.13) still accurately describes charge conservation since from eqs. (1.15) and (1.16) and Table 1.2, $[Cs^+ \cdot H_2O]/[Cs^+] = [H_2O] \cdot k_{3b}/k_{-3b} < 0.01\%$ at all temperatures greater than 500 K. Both the

$Cs^+ \cdot N_2$ and $Cs^+ \cdot H_2O$ clusters have been shown to occur in such small concentrations (relative to Cs^+) that the Cs_2^+ equilibrium concentration can be determined independently. In Fig. 1.11 the values for the Cs_2^+ and Cs^+ concentrations have been calculated first and then used to determine the $Cs^+ \cdot N_2$ and $Cs^+ \cdot H_2O$ concentrations. The $Cs^+ \cdot H_2O$ cluster will not provide a significant loss mechanism for Cs^+ and the presence of water vapor will not affect the equilibrium concentration of Cs_2^+ calculated from eqs. (1.10), (1.12), (1.13), and (1.14). Since the Cs_2^+ concentration is unchanged, previous statements about the negligible effect of dissociative recombination of Cs_2^+ still hold in the presence of water vapor impurities.

d. Conclusions from Reaction Kinetics Model

A model has been constructed to assess the role of several ion-molecule reactions that can, in principle, be present under conditions of relatively low electron number density and high ambient pressure, where experiments will be performed to measure the electron recombination rate. The results of this study, based on numerical and analytical solutions of a full set of kinetic equations with rate coefficients estimated from information in the literature, indicate that for temperatures in the range of 1000 K to 1500 K, electron decay rate measurements during the first 10 ms of plasma relaxation can be identified with the three-body process $e + Cs^+ + N_2 \longrightarrow Cs + N_2$, and can therefore be used to test theoretical predictions for this process. Our analysis of possible difficulties associated with the presence of a water vapor impurity indicates that in this temperature range the impurity effect is negligible.

It should be noted that considerable uncertainty exists for the values of many of the rate constants used in this study. However, the study's conclusions are based on robust arguments about partial equilibria and the ordering of time constants which generally demonstrate that two reaction rates or two characteristic times differ by many orders of magnitude. The strength of the inequalities involved make these conclusions insensitive to reasonable uncertainties in rate constants.

A.2.3 Advantages of the Pulsed Photoionization Experiment

In essence, what is needed to determine $\alpha'_{N_2}(T)$ is a measurement of the recombination rate in a plasma which is out of ionizational equilibrium and which contains only a single molecular species that can act as a third body for recombination. The pulsed photoionization experiment satisfies these requirements while avoiding many of the technical difficulties inherent in the steady-state, rapid expansion experiment. Since the plasma is stationary in the pulsed experiment, diffusion (not convection) determines the residence time of a plasma differential volume element. The characteristic time for the ambipolar diffusion of a Cs plasma in a one-inch-diameter tube containing N_2 at a pressure of one atmosphere is about 500 ms, at 600 K, or 4000 times longer than the convection-limited residence time in a 10-cm long sonic nozzle at 2000 K. If the previously derived formula for r/τ is used with t_{res} replaced by t_{diff}, one obtains $r/\tau = 700$ at $T = 400$ K and $r/\tau = 250$ at $T = 800$ K. For the photoionization experiment, it is necessary to have $\tau\ [=(\alpha_{N_2} n_{N_2} n_e)^{-1}/t_{diff}] \ll 1$ (in contrast to the condition $\tau \simeq 1$ for the rapid expansion experiment). It is possible to have this condition on τ satisfied and at the same time have $r \geq 10$ in the pulsed experiment.

The photoionization experiment creates an isothermal plasma because the kinetic energy of free electrons after photoionization is quickly thermalized. Recombination occurs at a constant temperature, and the temperature dependence of $\alpha'_{N_2}(T)$ is measured directly by simply repeating the experiment at different temperatures. The large r/τ ratio obtainable in the pulsed experiment allows both r and τ to be chosen independently to eliminate ambiguity about the role of the competing recombination on electrons and about the role of diffusion. In these respects the pulsed photoionization experiment appears to be more favorable than the steady-state rapid expansion experiment.

B. Experimental Work

Experimental work on the recombination project has been oriented toward solving the technical problems associated with a reaction cell, handling of reactants, photoionization light sources, and diagnostics.

Our experimental efforts in each of these areas are summarized below along with pertinent information from the literature. Based on this work an experimental system is described in which rates for electron-ion recombination on molecular neutrals can be measured.

B.1 Reaction Cell

The photoionization experiment imposes demanding specifications on the environment in which the recombination reaction should be studied. Nitrogen number density on the order of 10^{19} cm^{-3}, with cesium vapor concentrations of about one part per million and impurity concentrations of much less than one ppm must be maintained. Optical access for the photoionization of the cesium, and access for species concentration measurements must be provided. Pressure differences between the reaction and ambient environments of about one atmosphere must be supported. An isothermal region must be heated up to temperatures as high as 1200°C. This section summarizes our investigation into the technologies of materials, thermal design, seals, and windows that can provide the specified reaction environment.

B.1.1 Materials

Table 1.4 presents a selection of materials which are known to be compatible with cesium. Next to the listed materials are the approximate maximum working temperatures for exposure to cesium, the information reference, and pertinent comments. In general glasses are available for work with cesium at low temperatures, but metals or ceramics must be used at higher temperatures. As temperature is increased, cesium reduces the SiO_2 in glass. Even at low temperatures the oxides in glass-to-metal seals are rapidly attacked by cesium vapor. Some metals (commonly used as brazing alloys), which either react rapidly or have high solubility in alkali metals, are antimony, bismuth, cadmium, calcium, gold, lead, silver, selenium, sulfur, platinum, and tin [1.33]. Ceramics can be useful as dielectric materials for the reaction cell walls, and, in crystalline form, as optical window materials. Single-crystal sapphire has excellent optical transmission qualities, high hardness, and it is commercially available. We have used it for cesium absorption measurements and photoionization experiments. Lucalox [1.34]

Table 1.4

Cesium Compatible Materials

Material	Maximum Temp., °C	Ref.	Comment
Glasses			
Aluminosilicates	500	[1.35]	Lower temp. for Na and K.
Corning 1720 Corning 1723		[1.36]	Temp. dependent transmission below 400 nm.
Borosilicates Corning 7740 Schott 8329	400	[1.35]	(Pyrex). Slowly discolor at higher temp.
Other glasses		[1.35]	
Gehlinite	600		Poor availability.
Calcium Aluminate	700		Limited shapes.
Schott 8436	540		400 nm transmission cutoff.
Refractory Metals	> 900	[1.35]	
Molybdenum	550	[1.37]	
Moly-50 Rhenium	1870	[1.37]	
Tantalum	2000	[1.38]	
Niobium	1400	[1.37]	
Ferrous Metals			
304 S.S.	870	[1.37]	Superior to 316 S.S.
Iron, Steel, Kovar	> 700	[1.35]	
Nickel and Alloys	> 700	[1.39]	Inconel, Nichrome, Monel.
Haynes-25, TD Nickel	1100	[1.39]	
Copper and Alloys	5-600	[1.35]	
Ceramics		[1.35]	
Lucalox	1200	[1.40]	High-pressure sodium lamps.
Polycrystalline Al_2O_3		[1.41]	Temp. could be higher.
Single-Crystal Al_2O_3	700	[1.35]	

is a translucent, polycrystalline alumina product which is far less expensive than sapphire. Imaging through Lucalox is severely impaired by scattering, but Lucalox can be used as a window material for photoionization where diffuse radiation is acceptable. Over 90% of the light from a source inside a standard Lucalox tube is claimed to be transmitted through the tube wall. Other ceramic crystals which exhibit good alkali metal compatibility include CaF_2, BaF_2, BeO, Y_2O_3, and MgO [1.35].

Cesium compatibility may not be the limiting factor in materials selection. The reaction rate of some materials with other reactant or ambient gases can be excessive at temperatures below their cesium compatibility limit. For example, niobium is oxidized rapidly above 400°C, reacts with water at 500°C, and is embrittled by N_2 and by H_2 above 400°C [1.42, 1.43]. Additional factors which affect material selection are mechanical strength to support typical loads at operating conditions, vapor pressure at elevated temperatures, and ease of fabrication.

Our first reaction cell design, as shown in Fig. 1.7, provided an example of complicating factors in material selection. Inconel 601 was initially chosen for the cell wall because of its cesium compatibility and its excellent resistance to oxidation in air at temperatures up to 1200°C. However, Inconel proved to be very difficult to weld to commercial stainless steel vacuum flanges. This problem was circumvented by brazing the flanges to the Inconel. High-temperature vacuum bakeout of the Inconel resulted in dark, sooty deposits on the windows and cooler parts of the reaction cell. Electron dispersive spectroscopic analysis of this deposit indicated it was composed of chromium and manganese or their oxides. These elements are present in Inconel in respective proportions of 20% and 1%. These deposits could be avoided for reaction cell temperatures above 450°C, only when at least an atmosphere of nitrogen is present. For later experiments we used a stainless steel reaction cell. Possible alternatives include nickel plating the inside of the reaction cell or changing to a ceramic material.

B.1.2 Seals

The fabrication of our alkali metal vapor system required seals between components such as the reaction cell, windows, the metal reservoir, and electrical feedthroughs. Often the components were of different materials, and demountable seals were desired. The seals had to be gas tight and resist cesium attack while operating at elevated temperatures. Sealing has been a challenging technical obstacle in all our system designs.

Metal to metal joining can usually be satisfactorily accomplished by tungsten inert gas welding and by copper or nickel brazing. These joints will remain leak tight until the materials begin to react with the gases present or until they melt. A convenient demountable joint can be made with commercially available stainless steel vacuum flanges (e.g., from Varian Corp.). These flanges use opposing knife-edges which deform a copper metal gasket. At 400°C these flanges performed well in our experiments with cesium. Bolt thread galling was prevented with molybdenum disulfide lubricant and silver-plated nuts. Upon disassembly, it was sometimes necessary to employ a wedge to separate the flanges and then the copper gasket had to be pryed off a flange. These vacuum flanges have been reported to seal well up to 650°C [1.35]. An excellent demountable seal for small-diameter metal tubing is the VCR coupling. (VCR is a fitting manufactured by the Cajon Company [1.44].) With nickel, stainless steel, or copper gaskets VCR couplings are rated to 537°C.

Alumina can be joined to metal by metalization and brazing, by an oxide frit seal, or by demountable o-rings and gaskets. A brazed joint is made by applying metalizing paint to the alumina and firing it at high temperature. Alkali-resistant paints should not contain silica; typically they are tungsten based with 2% yittria oxide, and they fire at 1550° to 1825°C. The paint is then plated with nickel and joined to the metal part with a copper or nickel braze material. These joints are reliable to about 700°C, but the seal must be designed to minimize stress due to differences in thermal expansion [1.45]. Sapphire windows brazed to kovar are commercially available in vacuum flanges. We have used two such windows [1.46] at 400°C for over 100 hours of exposure to cesium liquid or vapor. One of the windows developed a small leak at the brazed joint after about 50 hours; the other window is still vacuum tight, yet both windows are brazed with silver (which is not compatible with cesium). Varian Corporation is believed to make a sapphire vacuum window which is alkali resistant.

An alkali-resistant frit seal between niobium and alumina has been developed for sodium lamps. The frit material is composed of oxides of calcium, aluminum, and magnesium. Niobium is used because it is a good thermal expansion match for alumina and will not melt at the 1460°C temperature required to make the seal [1.35]. Frit seals can run for thousands of hours at 700°C [1.40]. Typically niobium is operated in a controlled atmosphere because of its reactions with oxygen, water, nitrogen, and hydrogen.

Metal o-rings or gaskets can be used to make a demountable seal between metal and sapphire. Figure 1.14 illustrates an o-ring design we have tried. A sapphire window, two inches in diameter, and 0.060" thick, was compressed between two metal o-rings which were located in standard vacuum flanges. The o-rings were fashioned from copper-jacketed Inconel springs which were designed to operate at temperatures up to 450°C. They required 2000 lbs/linear inch loading to seal [1.47]. The sapphire easily withstood the compressive stress, but great care was needed to avoid any asymmetric loading which could create bending moments and tensile stress. Windows were broken in assembly and during operation. When the window survived, the seal usually failed after one temperature cycle and required o-ring replacement. We cannot recommend this metal o-ring seal as a reliable technique. Sapphire windows have been sealed between copper gaskets in a VCR fitting [1.35]. This arrangement had a leak rate which increased with the operating temperature and with the number of temperature cycles.

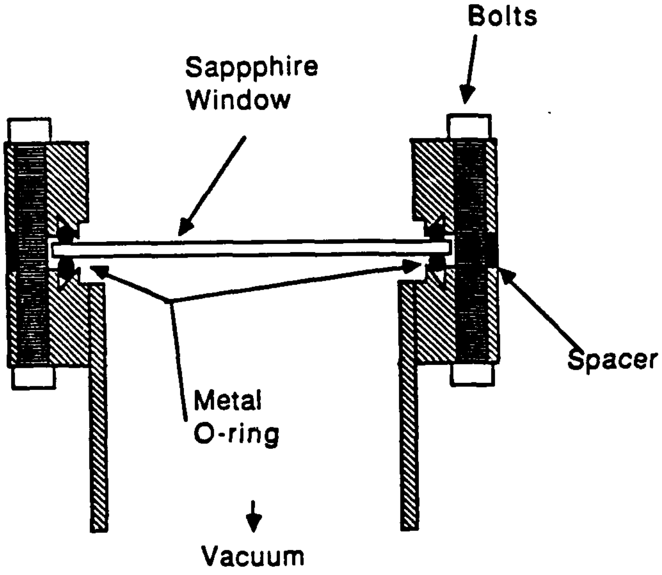

Fig. 1.14. High-temperature, cesium compatible, vacuum window design.

Vacuum-tight, heated, demountable seals between dissimilar materials are easily achieved with elastomeric o-rings if the joints can be designed to operate at less than 200°C (Viton) or 300°C (Kalrez) and to be free from alkali metals. Kalrez costs about 40 times as much as Viton. For low-temperature operation in the presence of alkali metals, the best o-ring materials have been found to be Kel-F 3700 and Buna-N tested in 120°C sodium vapor for nine days, and Neoprene and Buna-N tested in 180°C sodium vapor for seven days. Kel-F and Neoprene are halogenated and they could potentially react explosively with alkali metals [1.48].

B.1.3 Temperature

If cesium vapor contacts regions of the cell which are colder than the saturation (dew point) temperature of the vapor, cesium will condense there. The saturation temperature for our experiments is typically in the range 200°-300°C. To prevent the condensation and loss of cesium, every part of the cell must be heated to at least the dew point temperature, as in a hot-cell design, or the vapor must be prevented from reaching the cold regions, as in a heat pipe oven design. Available sealing technology limits the maximum sapphire window or ceramic feedthrough temperature to less than 700°C. A reaction environment maximum temperature of 1200°C implies that temperature gradients will necessarily exist between the windows or feedthroughs and the region where recombination is measured.

A hot cell was constructed in the course of the present work. The heating system was composed of three separate ovens. Referring to Fig. 1.15, these were F4, the reservoir over (25°-400°C), F8, the reaction cell oven (400°-1000°C), and F9, the box oven (400°C) The respective purposes of the ovens were to control the cesium vapor pressure, to heat reactants to elevated temperatures, and to maintain vacuum windows and seals at a temperature above that of the reservoir but below the operating limit of 450°C. Figure 1.7 shows a typical high-temperature profile through the reaction cell. The experiment was designed to measure reaction rates in the central isothermal region of the cell.

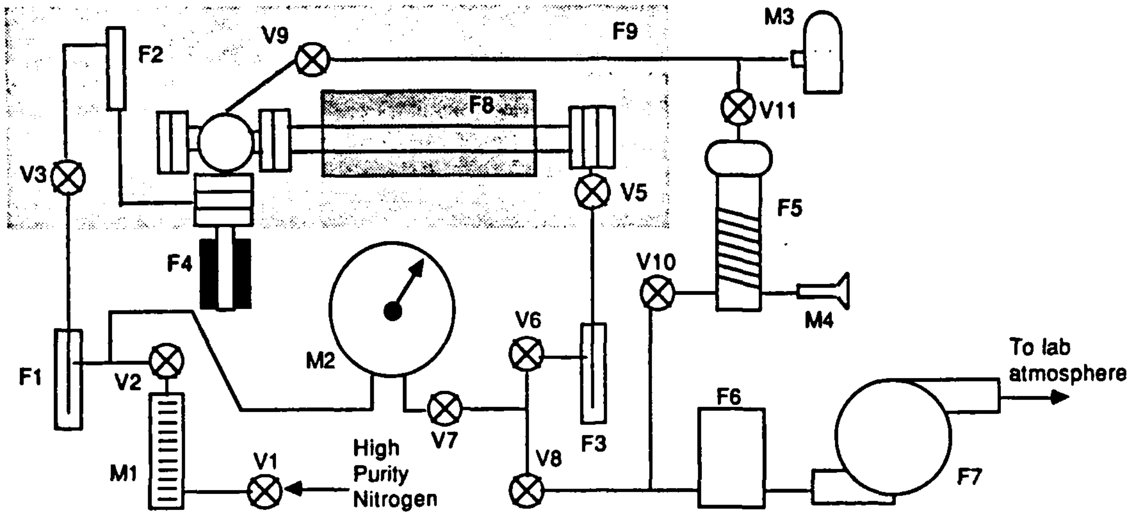

VALVES
1.regulator shut off, Hoke
2.needle 0-400 cc/min, Porter
3.bakeable bellows, Nupro
4.bakeable bellows, Nupro
5.needle 0-400 cc/min, Porter
6.on-off inline o-ring
7.bellows o-ring
8. bakeable bellows 1 1/2",Varian
9. bellows o-ring
10.gate valve o-ring

METERS
1.flowmeter 50-300 cc,min, Porter
2. diff. press. gage, 800 torr, W&T
3. ion gage
4. thermocouple gage

FIXTURES
1.Cs trap
2. Cs ampuole holder
3. Cs trap
4. reservoir oven
5. diffusion pump
6. zeolite trap
7. roughing pump
8. hi temp oven
9. med. temp oven

Fig. 1.15. Heating, vacuum, and gas flow systems for a hot cell design.

Heat pipe ovens [1.49] utilize evaporation, condensation, and a metal wick to maintain cold cell ends in which a nonreactive buffer gas is confined, and a heated interior in which a homogeneous, steady-state concentration of alkali metal vapor is confined. In typical operation, the metal vapor pressure is equal to and controlled by the pressure of the buffer gas. The vapor and gas do not mix except in a thin interface. Materials such as o-rings which only operate at low temperature without alkali contact can be used on the ends. These ovens have been operated in a regime where the metal vapor pressure was determined by temperature control of the wick, so the buffer gas pressure could be arbitrarily selected [1.50]. The central region of the heat pipe has been operated without a wick and it has been heated to create a region of superheated vapor and buffer gas of arbitrary number density [1.51, 1.52]. Turbulence and alkali mist or rain has been observed in the condensation region of heat pipe ovens which were operated at high buffer gas and alkali vapor pressures. The turbulence and mist adversely affect optical transmission through the pipe, but conditions at the center and ends are not affected [1.35].

B.2 Gas Handling

The design of a system to supply gases to the reaction environment is influenced by chemical reactions with impurities and by mass transport. These reactions can have two effects: First, cesium atom reactions with impurities can reduce the concentration of cesium vapor which is available for photoionization, and secondly, reactions between charged species and impurities during recombination can interfere with the intended measurement of the $Cs^+-e^--N_2$ recombination reaction. Mass transport is necessary to move cesium to the reaction zone as it vaporizes from a liquid state. Other mass transport processes, such as diffusion to a colder region, may simultaneously reduce the vapor concentration. The net mass transport must produce a steady-state vapor concentration in the reaction zone.

The cesium vapor design concentration is nominally 1 ppm in 10^{19} cm^{-3} of nitrogen, but the design figure could vary between 0.1 ppm and 10 ppm. Cesium vapor is a strong reducing agent, and it readily reacts with oxygen and water vapor. The concentrations of these common impurities must be maintained far below the lowest cesium concentration to prevent substantial loss of cesium (in this case, much less than 0.1 ppm). With respect to the second effect of impurities, kinetics modeling of the role of water vapor as a participant in an undesirable electron loss mechanism indicated that water concentrations of up to 1 ppm would be acceptable. In the case of water vapor, reactivity with cesium determined the upper limit of acceptable impurity concentration. Potential impurities, such as hydrocarbons or chromium, may not react directly with cesium vapor, but they might form negative ions, clusters with cesium ions, or otherwise react with charged species during recombination. We have not modeled the effect of such impurities on the recombination kinetics, but have assumed that a reaction environment which is pure enough to preserve low cesium concentrations will not introduce undesirable charged species reactions.

Impurities can enter the system through leaks, from outgassing surfaces, and with entering reactants. Leak rates can usually be kept acceptably low with proper seal design. If leaks are unavoidable, the reaction cell pressure should be higher than ambient pressure, so reactants will flow out and impurities will not flow in. Outgassing can be reduced by preparatory cleaning. Standard vacuum-cleaning procedure, including degreasing, acid pickle, deionized water, and alcohol wash should be followed [1.53]. The system should be baked out at operating temperature or at least 200°C, in vacuum better than 10^{-5} torr or under flowing gas of high purity, before cesium is admitted. A flowing system which continually flushes the reaction cell with a fresh supply of reactants can reduce the concentration of impurities due to leaks and outgassing by increasing the flow rate. Because cesium vapor is constantly mixed with new nitrogen in a flowing system, the nitrogen purity must be very high to avoid depletion of the cesium. Nitrogen with less than 5 ppm total impurities is commercially available, and purification to < 1 ppm impurities is commonly done in industry, but it can be costly. A convenient gettering technique for impurities which react with alkali metals is to bubble the nitrogen through hot NaK [1.39]. Gettering is inherent in a static system, such as a heat pipe oven, which is charged with a fixed amount of nitrogen and cesium. The nitrogen is purified by reactions with cesium before the cesium charge is depleted. Lower purity standards for the nitrogen charge are acceptable in a static system than in a flowing system. Additionally, a heat pipe tends to move impurities away from the reaction zone with constant evaporation, condensation, and wicking action. Impurities in the cesium are generally other alkali metals, and the most common purification technique is vacuum distillation [1.39]. To prevent contamination during installation the cesium should be handled under positive pressure of cover nitrogen or under vacuum.

Techniques of mass transport vary with system design, but diffusion velocity is usually an important parameter. Molecular diffusion of relatively low concentrations of cesium vapor through nitrogen has a binary diffusion coefficient of [1.53]

$$D_{Cs-N_2} = \frac{1}{3} \lambda_{Cs} C_{avg} = \frac{2}{3d^2 p} \left[\frac{k^3 T^3}{\pi^2 m_{Cs}}\right]^{1/2} .$$

Here λ_{Cs} denotes the cesium mean free path, C_{avg} is the cesium average thermal speed, d (= 4.5 Å) is the average atomic diameter for Cs and N_2, p is the pressure of N_2, $k = 1.38 \times 10^{-23}$ J/K, and m_{Cs} is the mass of a cesium atom. For our conditions, D_{Cs-N_2} is on the order of 0.1 cm^2/sec, and taking the characteristic dimension for density gradients to be one centimeter, maximum diffusion velocities are on the order of 0.1 cm/sec.

B.2.1 Flowing System Design

The gas delivery system shown in Fig. 1.15 was designed and built to meet the above requirements. The system was designed to provide a flow of high-purity nitrogen, saturated with cesium vapor. Nitrogen flow is measured by rotometer M1, and pressure gauge M2. The flow is throttled by valved V2 and V6. The nitrogen is bubbled through a ring of radial holes in the end of the feed tube in the cesium reservoir, as shown in Fig. 1.16. The copper wool in the bottom of the reservoir was intended to act as a sparger, creating small bubbles. Later the wool was removed

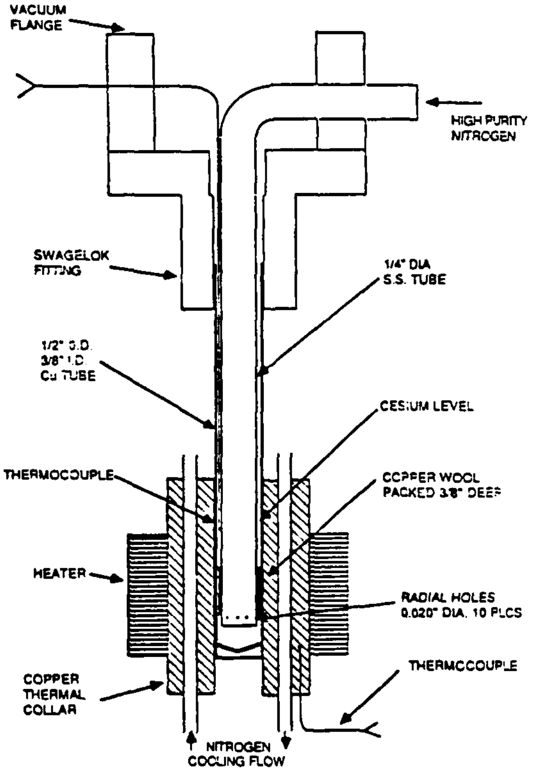
VACUUM FLANGE
HIGH PURITY NITROGEN
SWAGELOK FITTING
1/4" DIA S.S. TUBE
1/2" O.D. 3/8" I.D. Cu TUBE
CESIUM LEVEL
THERMOCOUPLE
COPPER WOOL PACKED 3/8" DEEP
HEATER
RADIAL HOLES 0.020" DIA. 10 PLCS
THERMOCOUPLE
COPPER THERMAL COLLAR
NITROGEN COOLING FLOW

Fig. 1.16. Cesium reservoir for flowing system design.

from the apparatus. A minimum flow rate was chosen to sweep out impurities which might have entered the system at a rate corresponding to the measured vacuum leak rate. The residence time in the region of the cell where recombination was to be observed needed to be much greater than the predicted two-millisecond reaction time, so the maximum flow rate through the 2-cm-diameter reaction cell was limited to 10 liters/min.

The tightest constraint on gas flow rate was calculated to be the time required to saturate nitrogen bubbles with cesium in the reservoir. This calculation was based on the time, t_{diff}, necessary for saturated cesium vapor to diffuse from the outer boundary of a nitrogen bubble of radius r to the center. Diffusion was considered complete when the cesium number density at the bubble center was 96% of the value at the bubble boundary. The diffusion time was given by [1.54]

$$t_{diff} = 0.4\ r^2/D_{Cs-N_2}\ .$$

The residence time, t_{res}, of the bubble in the cesium was found by solving the bubble's equation of motion for its terminal velocity [1.55], and by estimating a 1-cm path through the cesium. The bubble diameters expected from the 0.020" holes in the nitrogen nozzle (Fig. 1.16) were in the range 0.04"-0.1". These bubbles were found to have Reynolds numbers of about 1000, and a pressure drag coefficient of 0.4 was estimated [1.55]. The 0.1"-diameter bubbles are the largest acceptable due to the requirement $t_{res}/t_{diff} \geq 1$. This ratio is proportional to $r^{-2.5}$. Gas flow rates were limited by the maximum diameter bubble and minimum residence time to less than 40 std cc/min. Convective transport of vapor through the bubble was not considered here, but it could be a dominant transport mechanism [1.55]. Hence the flow-rate limit set by this bubble saturation calculation is thought to be conservative.

Aerosols of liquid cesium were found to be generated by the bubbling in the cesium reservoir. The aerosols were detected with scattering from a laser beam. They would control the cesium vapor number density based on the cell temperature, and the reservoir temperature could not be used as a direct indication of number density. In order to prevent the aerosols from leaving the reservoir, the reservoir diameter above the cesium was increased three-fold to 1.5", and packed copper wool and stainless steel mesh were inserted 1.5" above the cesium level. Trapping in this manner was not effective.

To avoid the aerosol problem, an alternative approach would be to replace bubbling with evaporation from a wick. The wick serves to increase the ratio of surface area to volume for the liquid cesium, thereby increasing the evaporation rate. Capillary action limits the wick vertical dimension. Metal wicks have been used successfully for evaporation in alkali metal heat pipes [1.49]. In a heat pipe oven the wick is adjacent to the reaction zone; the wick may also be placed in a separate reservoir for a flowing system. Diffusion and natural convection transport vapor in a heat pipe, so bulk velocities are low and wick size can be smaller than in a flowing system which uses forced convection with higher bulk velocities.

B.2.2 Cesium Number Density Measurement

Ideally the value of the cesium number density in the reaction cell should be given from equilibrium and saturated vapor pressure relations [1.39] as

$$(n_{Cs})_{cell} = \frac{T_{res}}{T_{cell}} \cdot (n_{Cs})_{res}$$

$$(n_{Cs})_{cell} = \frac{T_{res}}{T_{cell}} \cdot \left[\frac{7.34\times 10^{21}}{T_{res}} \exp\left(-\frac{8483.}{T_{res}} + 8.98\right)\right] .$$

Here T_{cell} and T_{res} are respectively the temperatures (in Kelvins) of the vapor in the reaction zone and the hottest portion of cesium liquid in the system. (The units of number density are cm^{-3}.) The actual number density might vary from this equilibrium prediction because of cold spots, hot spots, aerosols, adsorption, desorption, or convection. To test that a system is performing as expected, a direct measurement of cesium concentration is required. Possible techniques for measuring the cesium number density, n_{Cs}, can be divided into intrusive and non-intrusive categories. The intrusive techniques require collection of the Cs vapor. Intrusive techniques, which we have looked into, are based on the density, the chemical properties, and the dew point of cesium. Non-intrusive techniques, which we have used, depend on the optical properties of the vapor.

The density-based technique measures the weight of Cs collected in a cold trap in a flowing system over a known time period. The chemistry method reacts collected Cs with alcohol to form CsOH and then titrates the CsOH with HCl to determine the amount of Cs collected. The dewpoint method varies the temperature of a specular surface which is in contact with the Cs vapor. When the surface temperature equals the dew point, condensation can be observed (e.g., with an increase in diffuse scattering of a laser beam). The frequency response of this technique will decrease at higher N_2 pressures and at lower n_{Cs}.

The three optical techniques mentioned below involve observing a Cs absorption line using a tungsten halogen lamp, a monochromator, and a photomultiplier tube. These techniques are relatively fast and can be used for real-time monitoring of n_{Cs}. The range of Cs number density over which the technique is useful depnds on the absorption path length, the monochromator resolution, and the line chosen. The technique of matching actual and calculated line shapes requires both good spectral resolution and knowledge about broadening. The equivalent-width technique needs knowledge about the broadening but less resolution, and the integrated-absorption technique requires good spectrometer resolution but no knowledge of broadening to determine n_{Cs}.

For our conditions, the absorption line shape was dominated by nitrogen pressure broadening. In this case the line shape is Lorentzian and the absorption cross section is [1.56]

$$\sigma(\omega) = \frac{\pi e^2 f_{12}}{2\varepsilon_o m_e c} \left(\frac{\Delta\omega}{[\omega-\omega_{12}]^2 + [\Delta\omega/2]^2} \right) .$$

Here f_{12} denotes the oscillator strength for absorption from the ground to the first excited level of Cs, ω is the angular frequency (radians/sec), e is the charge of one electron, m_e is the mass of an electron, c is the speed of light, ε_o is the permittivity of free space, and $\Delta\omega$ [$= 2\pi c\delta(n_{N_2}/n_0)$; with $\delta = 1.0$ cm^{-1} and $n_0 = 2.7\times10^{19}$ cm^{-3}] is the Lorentzian full width at half maximum.

The value of $\Delta\omega$ for N_2-Cs broadening was inferred from Miles [1.57] and Chen [1.58]. A good source for oscillator strengths is Fabry [1.59]. When this cross section is used in Beer's law,

$$I(\omega,L)/I(\omega,0) = \exp[-n_1\sigma(\omega)L] \ ,$$

the width of the absorption profile, $I(\omega,L)$ can be much greater than $\Delta\omega$. Here L denotes the path length in meters, $I(\omega,x)$ is transmitted light intensity at the specified frequency and position, and n_1 denotes the ground state cesium number density.

The expression for the absorption cross section can be used to match the measured absorption profile with a theoretical profile. A sophisticated routine could optimize both the parameters n_1 and $\Delta\omega$ for the fit. A fit is especially useful in checking for anomalies due to aerosols, dimer band absorption, or systematic errors.

The expression for the cross section can be used to evaluate an equivalent width defined as [1.56]

$$W = \int_{\text{line}} \{1 - \exp[-n_1\sigma(\omega)L]\}d\omega \ .$$

Evaluating the equivalent width in the optically thin and optically thick limits gives expressions for the ground state Cs number density,

$$n_1 = \frac{2\varepsilon m_e W}{\pi e^2 f_{12} L} \ , \qquad n_1\sigma(\omega)L << 1 \ ;$$

$$n_1 = \frac{\varepsilon m_e c W^2}{e^2 f_{12} L \Delta\omega} \ , \qquad n_1\sigma(\omega)L >> 1 \ .$$

Between these two limits a curve of growth technique is necessary to establish the relationship between n_1, $\Delta\omega$, and W. The equivalent width is simply a measure of total absorption, and it can be obtained directly with a monochromator of resolution which is coarse relative to the Cs line. This technique avoids the need to scan the absorption line, but it is susceptible to errors due to effects which would change the absorption profile from the expected one.

By integrating Beer's law over the frequency range contributing to the line, it can be shown [1.60] that the ground state Cs number density is given by

$$n_1 = \frac{2\varepsilon_o m_e c}{\pi e^2 f_{12} L} \int_{\text{line}} \ell n\left[\frac{I(\omega,0)}{I(\omega,L)}\right] d\omega .$$

This integration approach requires a means to integrate the spectral transmission, but no information about the line shape is needed.

B.3 Light Sources

Photoionization of the Cs by Xe flashlamp radiation occurs through both one- and two-proton processes. The single-photon process converts a ground state 6s electron to a free electron as represented by

$$Cs(6^2S_{1/2}) + h\nu_1 \longrightarrow Cs^+ + e$$

The photon energy, $h\nu_1$, must exceed the ionization potential of Cs, i.e., 3.89 eV or $\lambda \leq 318$ nm. Two-photon ionization first excites a ground state electron with a resonant photon; a second photon then ionizes the excited atom. The two steps are

$$Cs(6^2S_{1/2}) + h\nu_2 \longrightarrow Cs^*(6^2P_{3/2,1/2})$$

$$Cs^*(6^2P_{3/2,1/2}) + h\nu_3 \longrightarrow Cs^+ + e$$

The resonance wavelengths are $\lambda_2 = 852$ nm ($J = 3/2$) or $\lambda_2 = 894$ nm ($J = 1/2$), and ionization from the 6p state can occur with any photon of wavelength $\lambda_3 \leq 508$ nm ($J = 3/2$) or $\lambda_3 \leq 494$ nm ($J = 1/2$). The cross sections for ionization from the 6s and 6p levels are approximately 10^{-19} cm^2 and 10^{-17} cm^2, respectively. The single-photon process has been included in our kinetics calculations; the ionization rate is proportional to the light intensity. The contribution to ionization rate from the two-photon process was estimated to be significant; this contribution is proportional to the square of light intensity [1.61].

B.3.1 Short Arc Lamps

The experimental arrangement of Fig. 1.7 has the simplifying feature that the light source is positioned away from the heat of the reaction zone. Placing the source outside the cell necessitated directing the light through a sapphire window at the end of the Inconel tube. To produce a well-collimated, intense photon flux, we used a 5-atm xenon short arc lamp and an ellipsoidal reflector.

The flashlamp dissipated a maximum of 300 Joules in 4 ms, corresponding to an average electrical input power of 75 kW. A circuit diagram of the pulsed power supply is shown in Fig. 1.17. The circuit design was determined by two principal factors: the very low lamp impedance combined with the need to keep the pulse length no longer than a few milliseconds, and the requirement of a high-voltage (30 kV) trigger pulse to initiate the discharge. The current pulse trace of the final circuit, shown in Fig. 1.18, was obtained with 0.010F of storage capacitor charged to 375 V. The peak current was 2.2 kA and the total pulse

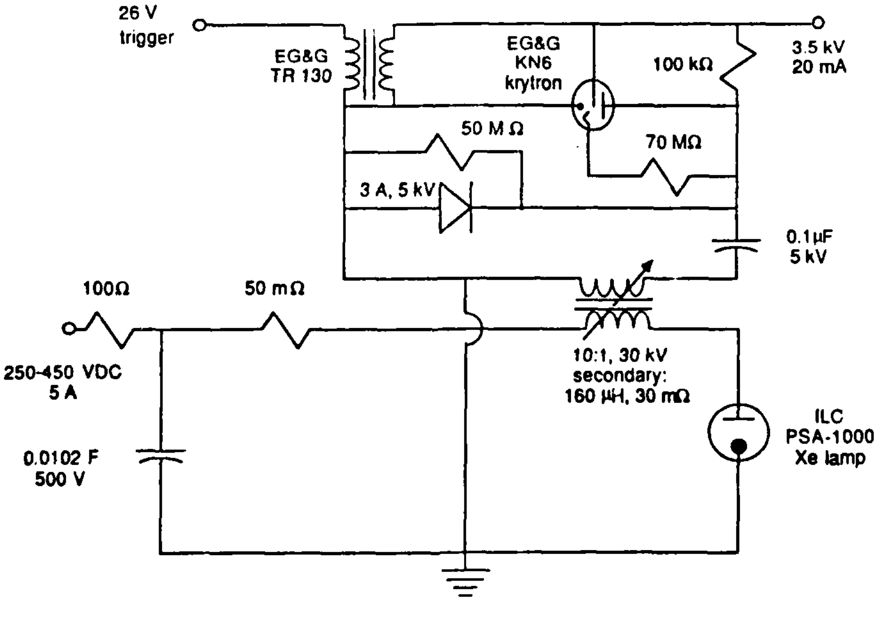
26 V
trigger
EG&G
TR 130
EG&G
KN6
krytron
100 kΩ
3.5 kV
20 mA
50 M Ω
70 MΩ
3 A, 5 kV
0.1µF
5 kV
100Ω
50 mΩ
250-450 VDC
5 A
0.0102 F
500 V
10:1, 30 kV
secondary:
160 µH, 30 mΩ
ILC
PSA-1000
Xe lamp

Fig. 1.17. Flashlamp circuit.

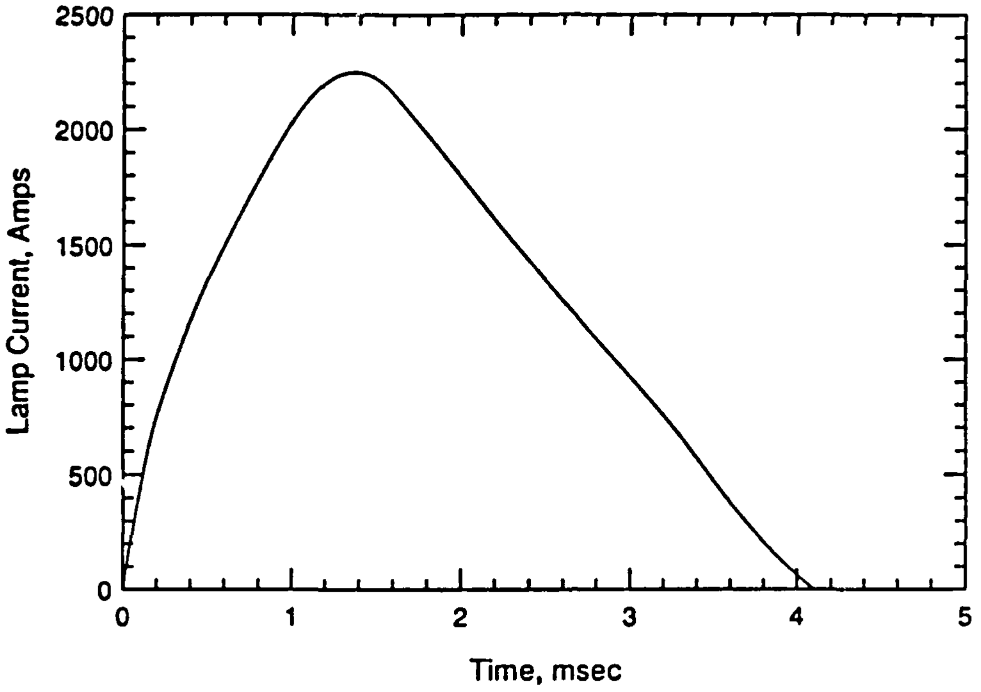

Fig. 1.18. Flashlamp pulse shape. Broadband light output follows the current.

length was 4 ms. The energy input could be varied by changing the voltage of the DC power supply used to charge the capacitor. Although the kinetics calculations indicate the need for a shorter pulse length, the present power supply was deemed to be satisfactory for performing exploratory experiments.

B.3.2 Linear Lamps

The low impedance of the short arc lamp resulted in a pulse duration which was about as long as the expected recombination times. A shorter pulse can be produced by crowbarring the short arc lamp or by using a linear, low-pressure lamp with greater lamp impedance. The linear lamp typically would have a length of 10 cm and a diameter of 0.4 cm. Light would be produced throughout this volume. Light from the linear lamp could be coupled to a reaction cell by placing the lamp parallel to and outside a cylindrical cell with transmissive walls (e.g., a Lucalox tube), or by placing the lamp coaxially, inside a cell of arbitrary wall material. The former arrangement could employ commercially available flashlamps which must be operated below 400°C to protect their glass-to-metal seals. The lamps would be cooled by an annular flow of air between the lamp and a quartz tube sheath. Experiments in our laboratory have demonstrated the feasibility of such cooling. The latter arrangement would require a lamp which could withstand the high temperature and alkali environment of the reaction cell.

A lamp capable of serving in the coaxial configuration has been built and tested. A lucolox tube, 4 mm I.D. and 26" long, was fitted with tungsten electrodes which formed a 4" central gap. The lamp ends were sealed with o-rings and the lamp was filled with 200 torr of argon. The lamp circuit was similar to the short arc circuit of Fig. 1.17, except that the discharge capacitor's characteristics were 5 μF and 10 kV, the trigger transformer saturated inductance was 18 μH, and no lumped series resistance was used. The lamp was tested in an oven with a center temperature of 1050°C and cold ends. The capacitor energy was 22 Joules and the pulse duration was 30 μsec. This lamp had a pulse duration much shorter than the expected recombination times. In the case of single-photon ionization, the final electron number density depends on the lamp energy, which was a factor of 12 smaller for the linear lamp compared to the short arc. In the case of two-photon ionization, the final electron number density depends on the product of the square of lamp intensity and pulse duration. This product was about equal for the two lamps we have built.

B.4 Diagnostics

The number density of reactants (electrons or cesium ions), or alternatively, the number density of the products (cesium atoms) must be measured in order to determine the recombination reaction rate. In this section various pertinent diagnostic techniques are discussed. These techniques are based on electromagnetic wave propagation through the plasma, determination of the plasma electrical impedance or optical spectroscopy. The cesium ions are generally not useful for diagnostic purposes because they have a small effect on the electrical characteristics of the plasma compared to the electrons, and the ions are difficult to access spectroscopically. The plasma to be diagnosed can be characterized by the following representative conditions: a constant nitrogen number density, n_{N_2}, of 10^{19} cm^{-3}, and initial cesium number density, n_{Cs}, of 10^{13} cm^{-3}, and an afterglow electron number density, n_e, of 10^8 to 10^{12} cm^{-3}; the electron collision frequency, ν, is 1.3×10^{11} sec^{-1} and independent of temperature [1.62], and the inverse of the characteristic time for recombination on nitrogen is 10^3 sec^{-1}; the temperature is 1000°C and the plasma is contained in a cylinder of 5-cm diameter and 10-cm length. Values of plasma frequency, $\omega_p = (n_e e^2/\varepsilon_o/m_e)^{1/2}$, and d.c. electron electrical conductivity, $\sigma_o = n_e e^2/\nu m_e$, are listed in Table 1.5 for the broadest anticipated range of n_e during recombination.

Table 1.5

Plasma Afterglow Electrical Characteristics

n_e, cm^{-3}	10^8	10^9	10^{10}	10^{11}	10^{12}
ω_p,sec^{-1}	5.6×10^8	1.8×10^9	5.6×10^9	1.8×10^{10}	5.6×10^{10}
σ_o,mho/m	2.2×10^{-5}	2.2×10^{-4}	2.2×10^{-3}	2.2×10^{-2}	2.2×10^{-1}

B.4.1 Microwave Diagnostics

The plasma dimensions must be much larger than the wavelength of electromagnetic radiation which is used to diagnose the plasma if plane wave propagation is assumed. A technique which uses a resonant cavity generally requires the plasma dimensions to be on the order of a wavelength. If the wavelength range of useable radiation is 10 cm (the length of the plasma cylinder) or shorter, the corresponding angular frequency range is $\omega \geq 1.8\times10^{10}$ sec^{-1}. Plane electromagnetic waves propagating in the z-direction, in a uniform medium have the phase factor $\exp[j(\omega t-\beta z) - \alpha z]$. Here α and β are respectively the attenuation and phase coefficients which are given by the following expressions [1.63]:

$$\alpha = \frac{\omega}{c} \left\{ -\frac{1}{2} \left[1 - \frac{\omega_p^2}{\omega_p^2 + \nu^2} \right] + \frac{1}{2} \left[\left(1 - \frac{\omega_p^2}{\omega_p^2 + \nu^2} \right)^2 + \left(\frac{\omega_p^2}{\omega_p^2 + \nu^2} \frac{\nu}{\omega} \right)^2 \right]^{1/2} \right\}^{1/2} ,$$

$$\beta = \frac{\omega}{c} \left\{ \frac{1}{2} \left[1 - \frac{\omega_p^2}{\omega_p^2 + \nu^2} \right] + \frac{1}{2} \left[\left(1 - \frac{\omega_p^2}{\omega_p^2 + \nu^2} \right)^2 + \left(\frac{\omega_p^2}{\omega_p^2 + \nu^2} \frac{\nu}{\omega} \right)^2 \right]^{1/2} \right\}^{1/2} .$$

For the plasma conditions of Table 1.5, it is generally true that $\nu^2 >> \omega_p^2$. In this limit

$$\alpha = \frac{\omega}{c} \left\{ -\frac{1}{2} + \frac{1}{2} \left[1 + \left(\frac{\omega_p^2}{\omega_p^2 + \nu^2} \frac{\nu}{\omega} \right)^2 \right]^{1/2} \right\}^{1/2} ,$$

$$\beta = \frac{\omega}{c} \left\{ \frac{1}{2} + \frac{1}{2} \left[1 + \left(\frac{\omega_p^2}{\omega_p^2 + \nu^2} \frac{\nu}{\omega} \right)^2 \right]^{1/2} \right\}^{1/2} .$$

The plane wave will be altered by the plasma if

$$\frac{\omega_p^2 \nu}{(\omega^2 + \nu^2)\omega} \approx 1 .$$

This condition is satisfied only when $\omega^2 < \nu^2$, and

$$\frac{\omega_p^2}{\nu\omega} \approx 1 .$$

The last relation in conjunction with Table 1.5 establishes the range of useful probe frequencies, $2.4\times10^6 < \omega < 2.4\times10^{10}$ sec^{-1}. Recall that the size of the plasma raises the lower limit on probe frequency to 1.8×10^{10} sec^{-1}. Therefore the range of electron number density which can be diagnosed by electromagnetic wave propagation diagnostics, based on measurable attenuation or phase shift and plasma size, is $7.5\times10^{11} < n_e < 1.0\times10^{12}$. Only a small part of the anticipated range of n_e (see Table 1.5) is included, and the included range is too small to measure appreciable recombination.

B.4.2 Plasma Impedance Diagnostics

The electrical character of the plasma afterglow is dominated by the electrons; ions play a negligible role. Applied electromagnetic fields and collisions with neutrals control the behavior of the electrons. Assuming the applied fields are electric, and proportional to exp($j\omega t$), the complex plasma electrical conductivity is given by [1.63]

$$\sigma = \frac{n_e e^2}{m_e \nu} \frac{1 - j\omega/\nu}{1 + (\omega/\nu)^2} .$$

When the wavelength of the applied field is much longer than the length of plasma filling the space between opposed electrodes across which the field is applied, the plasma may be treated as a lumped impedance. Taking the electrode spacing to be one centimeter, an impedance measurement can be made when $\omega << 1.8\times10^{11}$ sec^{-1}. If an impedance measurement is made in the afterglow, where $\nu = 1.3\times10^{11}$ sec^{-1}, then $\omega << \nu$, and the plasma conductivity is essentially the d.c. conductivity, $\sigma_{dc} = n_e e^2/m_e \nu$. Measurement of the d.c. conductivity yields information about the ratio n_e/ν, but data are available [1.62] to enable independent determination of the electron neutral collision frequency. The electrical circuit which measures the plasma conductivity may be directly, capacitively, or inductively coupled to the plasma.

Electrodes contact the plasma in a directly coupled conductivity measurement. Account must be taken of the sheath impedance between the electrode and the plasma. Although theory exists for spherical Langmuir probes in collision-dominated plasmas [1.64], the accuracy of the theory for such probes is still in question [1.65]. To avoid calculation of the sheath impedance, a four-electrode probe was fabricated and tested. As shown in Fig. 1.19, the probe consists of a linear array of three electrically insulated, cylindrical (wire) electrodes with a short length of the free ends uninsulated and in contact with the plasma. The inside surface of the reaction cell wall serves as the fourth electrode.

The design and operation of the probe have been described in an earlier report [1.66]. The basic idea is that a measured current, I, is

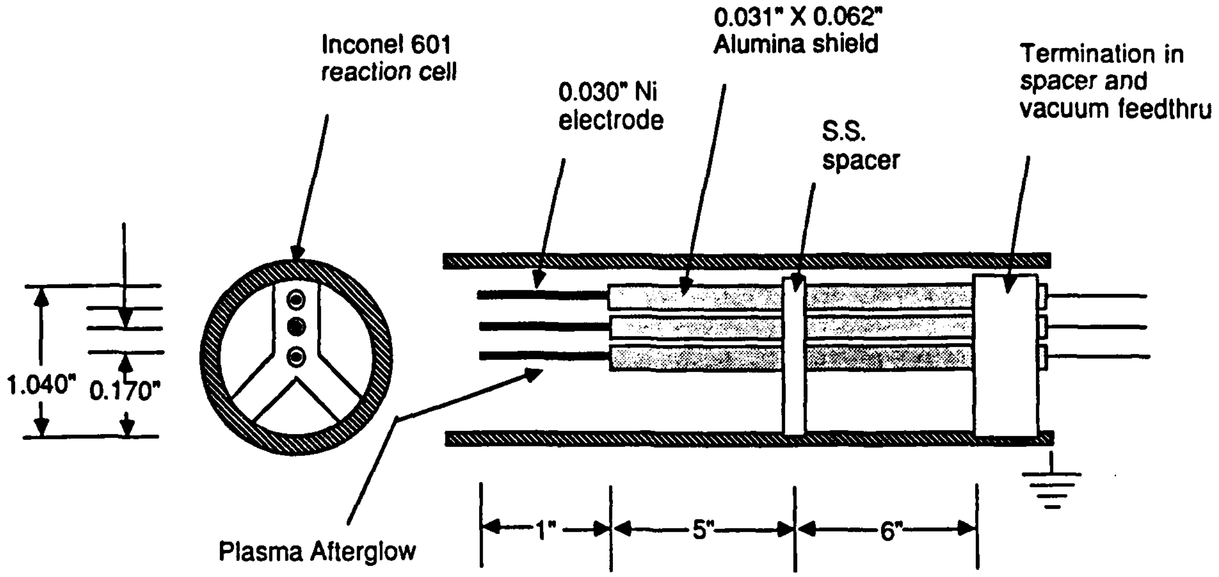

Inconel 601
reaction cell
0.030" Ni
electrode
0.031" X 0.062"
Alumina shield
S.S.
spacer
Termination in
spacer and
vacuum feedthru
1.040"
0.170"
Plasma Afterglow
1"
5"
6"

Fig. 1.19. Conductivity probe electrode configuration.

driven through the plasma between the outer electrodes consisting of the pin on the axis of the cell and the reaction cell wall, while the voltage δV picked up between the two off-center inner pins is recorded. By measuring the voltage between the inner, floating pins, sheath drops can be canceled, and the probe interpretation is simplified. A detailed schematic of the probe circuitry is shown in Fig. 1.20.

Given the concentric arrangement of the current-carrying, outer electrodes, the voltage difference $V = V(a) - V(b)$ between the outer electrodes can be calculated (assuming plasma resistance dominates sheath drops, and neglecting end effects) from the relation

$$- \int_a^b dV(r) = \int_a^b \rho J \, dr \ .$$

Here a and b are the radii of the on-axis and outer electrodes, respectively, ρ is plasma resistivity (ohm meters), J is current density (amps/m^2), and r is the radial coordinate. The result of the integration is

$$\frac{V(a) - V(b)}{I} = \frac{\rho}{2\pi L} \cdot \ln\left(\frac{b}{a}\right) \approx R_{plasma} \ .$$

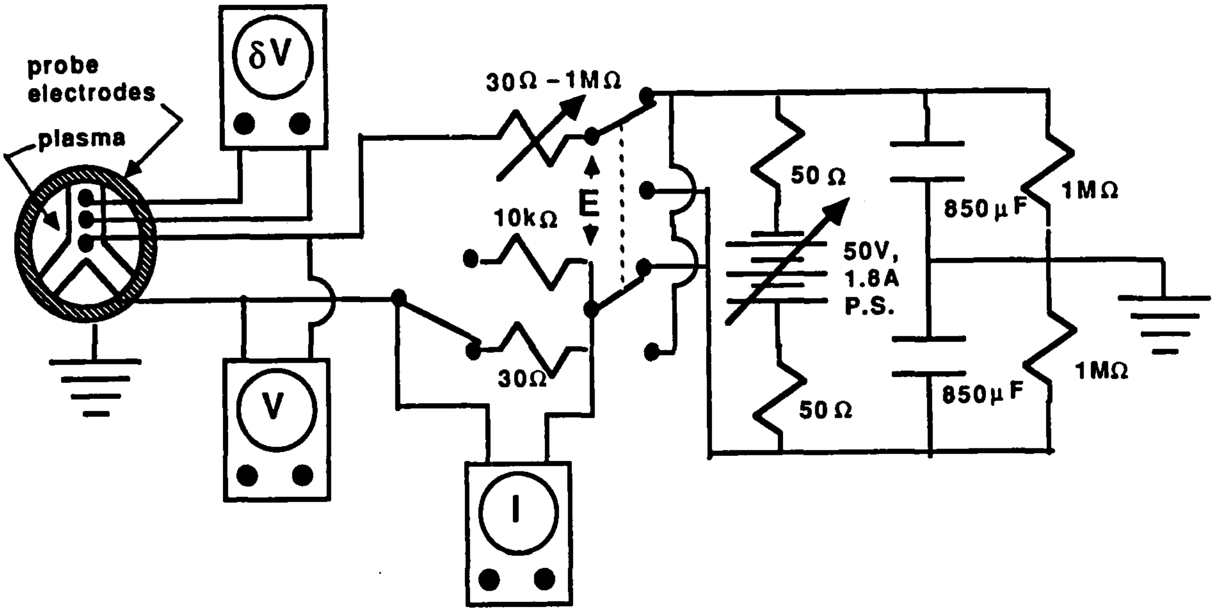

Fig. 1.20. Conductivity probe circuitry.

The voltage difference δV between the inner electrodes is given by a similar expression. Inserting values for the actual radii, the locations of the inner electrodes, and the electrode length L, the following values for the effective resistances (in ohms) between the electrodes are obtained:

$$\frac{\partial V}{\partial I} = 22.0\ \rho; \quad \frac{\partial \delta V}{\partial I} = 4.34\ \rho\ .$$

With reference to Fig. 1.20, let R represent the sum series resistance of the 1 MΩ potentiometer and the 10 kΩ or 30 Ω current resistors, let R_{plasma} represent dV/dI, and let E represent the voltage applied to the outer electrodes (assumed to be constant). By differentiating the circuit equation,

$$E = I(R + R_{plasma})\ ,$$

the effect of a change in the plasma resistance (such as a sudden decrease during photoionization) on the measurable parameters V, δV, and I can be predicted:

$$\frac{\partial I}{\partial R_{plasma}} = \frac{-E}{(R_{plasma} + R)^2} ,$$

$$\frac{\partial V}{\partial R_{plasma}} = \frac{E}{R_{plasma} + R} \left[1 - \frac{R_{plasma}}{R_{plasma} + R}\right] ,$$

$$\frac{\partial \delta V}{\partial R_{plasma}} \approx 0.2 \frac{\partial V}{\partial R_{plasma}} .$$

The probe can be run under two limiting regimes. In the constant-voltage regime, $R << R_{plasma}$ (generally R is set for 30 Ω), and only the current is affected by a change in R_{plasma}. In the constant-current regime the inequality is reversed (generally R is set to 1 MΩ), and only V and δV are affected by a change in R_{plasma}.

Testing of the four-electrode probe has not been completed, but some general observations can be stated. The capacitive susceptance, ωC, between electrodes should be kept much less than the conductance, 1/R, so that the probe measures conduction, not displacement current. This condition applied to two electrodes in a uniform plasma is

$$\omega << 1/(RC) = \sigma_{dc}/\varepsilon_o = \omega_p^2/\nu .$$

For the lowest ω_p of Table 1.5, this condition is met when $\omega << 2\times10^6$ sec^{-1}. For the lowest σ_{dc} of Table 1.5, the signal source impedance of the probe was $\partial\delta V/\partial I = 2\times10^5$ Ω. This large source impedance could limit frequency response and induce noise without careful circuit design. The high source impedance required good electrical insulation of the electrodes, which was difficult to achieve in the high-temperature, liquid metal environment. Recombination on the probe surface could create local plasma conductivity non-uniformity. Photoemission from the electrode surfaces during photoionization may significantly affect the measurement.

A capacitively coupled measurement operates at a frequency where the capacitive susceptance of the sheaths is large compared with the total admittance of the electrodes, i.e., $\omega C_{sheath} >> \omega C + 1/R_{plasma}$. The electrodes can be separated from the plasma by a dielectric wall if this inequality holds when the sheath capacitance is replaced by the series capacitance of the wall and sheath, i.e., $C_{sheath} \longrightarrow C_{sheath}C_{wall}/(C_{sheath} + C_{wall})$. In the case of parallel plate electrodes of area A and separation d, where impedance is dominated by the inter-electrode capacitance, C, and uniform plasma conductivity, σ_{dc}, current through the electrodes, I exp(jωt), due to an applied voltage, V exp(jωt), is given by $I = (VA/d)(j\omega\varepsilon_o + \sigma_{dc})$. A high-frequency bridge can be used to separate the conduction and displacement currents to determine the plasma conductivity [1.67]. In the actual circumstance of a non-uniform plasma conductivity, the current is given by

$$I = VA\left[\int_0^d \frac{dx}{(j\omega\varepsilon_o + \sigma_{dc})} \right]^{-1} .$$

The plasma conductivity spatial dependence determines if the electrode conduction current is proportional to the average plasma conductivity. Conductivity in the afterglow is controlled by volume and surface recombination, and ambipolar diffusion. We have mathematically modeled the spatial and temporal behavior of the afterglow conductivity field, and we have used the result to numerically integrate the expression for I. The integral always yields proportionality between conduction current and conductivity in the limit $(\omega\varepsilon_o/\sigma_{dc})^2 >> 1$. For the largest conductivity listed in Table 1.5, this limit would require $\omega >> 2\times10^{10}$ sec^{-1}, but our numerical calculations indicate that this is an unnecessarily extreme constraint on ω.

The impedance measuring circuit may also be coupled to a cylindrical plasma inductively through axial magnetic fields [1.68], or azimuthal magnetic fields [1.69]. Inductive coupling may have some advantages over capacitive coupling in working at lower applied field frequencies, and in working with a conductive plasma container.

B.4.3 Optical Spectroscopy Diagnostics

Optical diagnostics are attractive because the diagnostic hardware can usually be located outside the harsh environment of the reaction cell, and optical access to the afterglow plasma often can be compatible with access for photoionization. Line and continuum emission, and atomic absorption have been considered as the basis for measurement of electron number density and temperature in our plasma.

The specific power, $P_{u-\ell}$ (watts/m^3), of line emission from an upper state, u, to a lower state, ℓ, of the cesium atom is proportional to the upper state number density, n_u, and can be written [1.70]

$$P_{u-\ell} = n_u h\nu_{u-\ell} A_{u-\ell} ,$$

where $A_{u-\ell}$ is the Einstein coefficient for spontaneous emission, and $h\nu_{u-\ell}$ is the energy difference between the states. If the upper state is chosen to be close to the continuum, the population of that state will be in equilibrium with the free electron population throughout recombination. Assuming the ion and electron number densities are equal, n_u and n_e are then related by the Saha equilibrium relation,

$$n_u = n_e^2 \left[\frac{g_i}{g_u} \left(\frac{2\pi m_e kT}{h^2}\right)^{3/2} \exp\left(\frac{-\varepsilon_{ui}}{kT}\right)\right]^{-1} ,$$

where g denotes the degeneracy of the cesium ion or excited state, ε_{ui} is the energy difference between the excited state u and the ground state ion, and T is the equilibrium temperature of the system. Collisions with nitrogen rapidly bring the photo-electrons to the equilibrium temperature. An absolute intensity measurement of line emission can be related, by the preceding equations, to electron number density.

The specific power, $P_{e-\ell}$, of continuum emission accompanying capture of free electrons of speed distribution $F_e(u_e)$ to a bound state, ℓ, in the cesium atom in the frequency range ν_1 to ν_2 is given by [1.71]

$$P_{e-\ell} = \int_{u_1}^{u_2} h\nu_{e-\ell}\, \sigma(u_e) u_e F_e(u_e) du_e ,$$

where u_e is the free electron velocity, $h\nu_{e-\ell}$ is the kinetic plus potential energy difference between the free and bound electron, and $\sigma(u_e)$ is the cross section for radiative capture. Measurement of the continuum emission can yield information about the electron number density and the electron velocity distribution. If F_e is a Maxwellian distribution, the electron temperature can be determined.

Diagnostics based on line and continuum emission share several common features. Since both forms of emission are present in the spectrum simultaneously, care must be taken to chose regions of observation where overlap is minimized. Additional interference can come from the overlap of continuum bands. Although the photoionization source should be extinguished during recombination measurements, the optical detector must be protected from damage during photoionization. These emission measurements require absolute intensity calibration; relative intensity measurements can determine temperature, but not electron number density. The measured intensity is proportional to the square of electron number density when ion and electron number density are assumed to be equal. The ratio of signal to shot-noise is proportional to the square root of the signal. To observe a factor of 10 decay in n_e, a factor of 10 decrease in signal-to-noise must be tolerated. At low electron number density the emission signal at the start of recombination is near the shot noise detection limit and further signal reduction may not be acceptable. For example, we have calculated the signal-to-shot noise ratio for continuum emission in the 4700 Å to 5000 Å range due to recombination to the 6P level of cesium, and for line emission at 6326 Å due to the 10F to $5D_{3/2}$ transition. The regions of observation were chosen to minimize line and continuum overlap [1.72]. With the assumptions of an emitting volume of 20 cm^3, 2% optical collection efficiency, 25% detector quantum efficiency, 10^{-4} sec temporal resolution, and n_e = 3×10^{10} cm^{-3}, the signal-to-noise ratio for the continuum and line emission, respectively, were 55 and 245. Careful optical design, perhaps utilizing filters for spectral selectivity with large etendue, is required to use emission-based techniques to diagnose the plasma conditions of Table 1.5.

Cesium atomic absorption has been used extensively in our reservoir development efforts. When substantial photoionization of the ground state of cesium occurs, a corresponding reduction in absorption by the ground state will result. It has been shown [1.73, 1.74] for conditions of our plasma (where the number density of excited atoms is much less than the number density of free electrons, and the mean thermal energy is much less than the first excitation energy) that the relaxation times for the excited levels are much shorter than the relaxation time for the ground level or for the free electrons. This display in relaxation times (i.e., partial equilibrium) allows us to equate the negative of the time derivative of the ground state population with the time derivative of the electron population. Thus the recombination rate can be determined by observation of ground state absorption, provided the fractional change in the ground level population is not too small. To examine the feasibility of this approach, a photoionization experiment was performed to measure the fractional degree of ionization, under the same assumptions. For this experiment, the monochromator was kept at a single spectral location, as shown in Fig. 1.21, and the change in absorption during photoionization was monitored. A flashlamp served as the source both for the absorption measurements and for photoionization.

The data were interpreted by inverting Beer's law to get the following expression for ground state cesium number density as it varied with time,

$$n_1(t) = \{\ell n[I_o(t)/I(t)]\}/[L\sigma(\omega)] \ .$$

Here L is the optical path length, assumed to be constant during the flash, $\sigma(\omega)$ is the optical cross section for absorption, assumed not to be a function of time or location. The quantity I(t) is the time-varying transmitted source spectral intensity and $I_o(t)$ is the source spectral intensity without absorption. Note that $I_o(t)$ also varied with

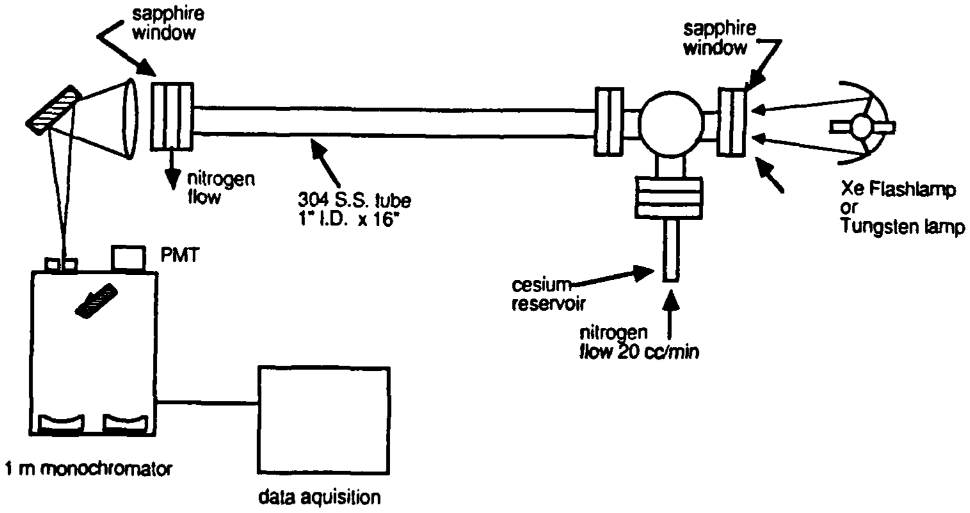
sapphire window
sapphire window
nitrogen flow
304 S.S. tube 1" I.D. x 16"
Xe Flashlamp or Tungsten lamp
PMT
cesium reservoir
nitrogen flow 20 cc/min
1 m monochromator
data aquisition

Fig. 1.21. One-beam ionization experiment.

time. By manipulating this expression, the following expression for relative change in number density is derived:

$$\frac{n(t_1) - n(t_2)}{n(t_1)} = 1 - \frac{\ln[I(t_2)/I_o(t_2)]}{\ln[I(t_1)/I_o(t_1)]} .$$

Here, t_1 is typically the time immediately preceding photoionization, and t_2 refers to any time during which the cesium was not in equilibrium.

First an absorption scan was taken with the tungsten lamp and the spectral locations for transmission fractions equal to 0.2, 0.8, and 1.0 were identified. Then the tungsten halogen lamp was replaced by the xenon short-arc flashlamp and the cesium vapor was photoionized. The light which passed through the vapor, during the flash, was monitored at a single wavelength by the monochromator. The data indicated that ground state depletion occurred, but scatter due to pulse-to-pulse variation of the flashlamp output made the results inconclusive.

Two-beam experiments which utilize orthogonal photoionization and probe beams to remove the measurement dependence on pump beam variations were also performed. No indication of ground state depletion was observed in these experiments. However, the interpretation of these ground state absorption measurements were complicated by absorption in cesium vapor which is not within the photoionizing beam, and by attenuation of the photoionizing beam before it crossed the probe beam.

B.5 Conclusions

The work described above leads to the following conclusions with respect to the design of a new experiment. Reaction cell materials could be polycrystalline alumina, stainless steel, or Inconel. The metals should be plated on the interior with nickel to prevent the outgassing of alloys. These materials are relatively inexpensive, available, oxidation-resistant, and easy to use, in addition to being compatible with cesium vapor to 1200°C. Window material, to separate the cesium vapor and the photionization source, could be fused silica, Lucalox, or single-crystal alumina. The latter two materials could withstand the reaction cell environment while the silica must be protected with a heat-pipe configuration. Sealing should be accomplished with elastomeric o-rings which are protected from high temperature and alkali attack with a heat-pipe configuration. Metalized and brazed seals, although quite competent, are much more expensive and difficult to use than o-ring seals.

The heat-pipe-oven design obviates many of the gas-handling difficulties inherent in the flowing system design. The main advantages are elimination of aerosol in the high-temperture region, low bulk velocities, and continuous purification of the alkali metal vapor and reactant gas. A potential difficulty of the heat-pipe approach lies in the generation of aerosols in the region of vapor condensation. These aerosols are problematic only if photoionizing or diagnostic light must pass through them, and if extinction is unacceptably high.

The recombination rate is most easily measured in the high-collision-frequency, low-plasma-frequency conditions of the afterglow with a lumped impedance conductivity measurement. Directly, capacitively, or inductively coupled measurements are all possible. The latter two coupling approaches alleviate concerns of plasma perturbation through surface recombination on the probe or photoemission, and of operation in the alkali environment by coupling through the reaction cell wall. Optical diagnostics should be explored as a check on the recombination rate measurement and as a possible measure of the electron temperature. The success of optical diagnostic techniques will depend on the plasma emission signal level and on the extent of photoionization, quantities which are best determined experimentally.

A design for the next-generation experiment which draws on the above features would employ a polycrystalline alumina 2"-diameter tube. A 4-mm diameter Lucalox flashlamp like the high-temperature version we have previously built would be mounted coaxially. A split wick, over-pressured heat-pipe-oven design would be used having cold ends, a wick region of controlled intermediate temperature, and a center high-temperature reaction region. A conductivity probe could be capacitively coupled through the ceramic cell wall. Optical diagnostic access would be provided through fused silica end windows sealed with o-rings.

2.2 Discharge Effects: Plasma-Electrode Interaction

2.2.1 Introduction

The operation of plasma devices, such as magnetohydrodynamic generators, thermionic converters, and magnetoplasmadynamic thrusters, depends on their ability to transfer current to and from the plasma via electrodes, yet little is known about the current transfer process or the electrical boundary layer which forms in the near-electrode region.

Current transfer at the electrode can be either diffuse or constricted in nature. The diffuse mode occurs for relatively low current densities. In this mode, the boundary layer resistance is large, and a substantial voltage drop occurs across the layer. The resulting power loss to the plasma decreases the overall device efficiency. For larger current densities, current constrictions form, and the current is transferred to the electrode through one or more highly conductive channels or arcs. The high temperatures within the arc rapidly erode the electrode surface, shortening the device life.

The work described herein, is aimed at improving the present understanding of the diffuse current transfer mode, for the case of a seeded thermal plasma at pressures on the order of one atmosphere, flowing between plane-parallel electrodes. In addition, the dominant mechanisms and conditions which lead to the transition to the constricted current transfer mode have been investigated.

The plasma-electrode boundary layer consists of four major overlapping regions. For a plasma flowing over a plane electrode (see Fig. 2.1), at an arbitrary streamwise (z) location one finds

i) The **Gasdynamic Boundary Layer**, of scale

$$\delta \propto \frac{T_\infty - T_{electrode}}{\partial T(x)/\partial x|_{x=0}} \approx 10^{-2}\,\mathrm{m},$$

which includes both the thermal and velocity boundary layers. Here, T_∞ is the core plasma temperature at the edge of the boundary layer and $T_{electrode}$ is the plasma temperature at the electrode surface. In this region, the plasma is in thermodynamic equilibrium at the local temperature $T(x)$ and the electric field $E(x) = J/\sigma(x)$ is established where [illegible] is

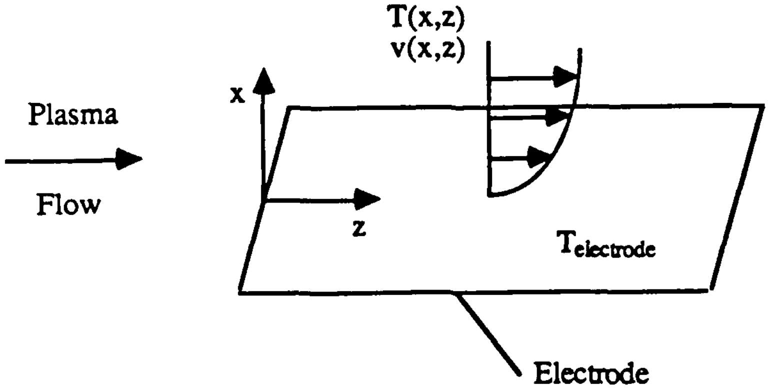

Fig. 2.1. Coordinate system for plasma flow over a plane electrode.

the current density and $\sigma(x)$ is the equilibrium electrical conductivity;

ii) The **Ionization Nonequilibrium Layer**, of scale

$$\ell_R \equiv \sqrt{2D_a/\beta(T_e)\,n_\infty^2} = \begin{matrix}\text{Ion Recombination}\\ \text{Length}\end{matrix} \approx 10^{-3}\,\text{m}.$$

Here, $\beta(T_e) \approx 10^{-20}T_e^{-9/2}$ m^6/sec is the three-body recombination coefficient divided by the plasma concentration in the freestream, n_∞. T_e is the electron temperature, and D_a is the ambipolar diffusion coefficient. In this region, the generation rate of electron-ion pairs exceeds the recombination rate to supply net fluxes of charged particles;

iii) The **Sheath**, of scale

$$\lambda_{D_\infty} \equiv \sqrt{\epsilon_0 kT_\infty/n_\infty e^2} = \begin{matrix}\text{Debye}\\ \text{Length}\end{matrix} \approx 10^{-6}\,\text{m}.$$

In this layer, charge neutrality is not preserved and large electric fields develop which must be calculated from Poisson's equation. The sheath matches the fluxes from the ionization nonequilibrium layer to the emission, absorption, and recombination processes at the electrode surface; and

iv) The **Knudsen Layer**, of scale

$$\ell_i = (c_i/\nu_i) \sim \ell_e = (c_e/\nu_e) = \begin{matrix}\text{Mean Free}\\ \text{Path}\end{matrix} \approx 10^{-6}\,\text{m},$$

> where free molecule flow takes over from a continuum description. While the mean free path and Debye length are of the same order, the sheath is normally several Debye lengths thick, so that the sheath is, for the most part collision dominated.

As indicated above, the scale lengths are ordered according to the relation $\ell_e \sim \ell_i \sim \lambda_D \ll \ell_R \ll \delta$. These divisions are quite arbitrary, and no distinct boundaries exist.

2.2.2 Research Objectives

1. To develop analytical and computer models and to predict the diffuse mode current-voltage characteristics for anodes and cathodes under a wide range of operating conditions.
2. To use the computer model to investigate the conditions whereby electron temperature nonequilibrium effects become dominant and lead to the transition from a diffuse to a constricted mode of current transfer.

2.2.3 Status of Research

A 1-D, continuum model has been developed to examine the DC discharge characteristics for a collision-dominated weakly ionized, thermal plasma contacting a plane electrode.

A novel feature of this formulation is that a single set of governing equations is solved throughout the entire boundary layer region, hence a solution is obtained which is valid through both the ionization nonequilibrium layer and the sheath. Solutions are found over a wide range of plasma and electrode conditions; our goal has been to examine the *nature* of the plasma-electrode interaction instead of simply modeling one specific experiment or set-up.

The current approach is in contrast to asymptotic methods where differing approximations are made for each of the overlapping sublayers, separate sets of equations are solved for each sublayer, and the solutions are matched at the boundaries. The latter method may only be used in the limit of some small parameter (the sheath thickness in this case), and it is complicated by the difficulty in choosing the (non-physical) boundary positions.

A. Governing Equations and Non-Dimensionalization

The charged particle behavior is governed by the electron and ion conservation equations for mass and momentum, together with Poisson's equation and the electron energy equation. The dependent variables include the electron and ion number densities $\left(n_e(x) \text{ and } n_i(x)\right)$, the electron and ion particle fluxes $\left(\Gamma_e(x) \text{ and } \Gamma_i(x)\right)$, the electric field $\left(E(x)\right)$, and the electron temperature $\left(T_e(x)\right)$. Additionally, the electric field may be integrated to obtain the scalar potential $\left(\Phi(x)\right)$. The independent variable (x) is the normal distance from the electrode surface.

The basic equations were developed subject to the following assumptions:

1) One-dimensional, steady-state system with a plane electrode contacting a semi-infinite plasma in the half-space $0 \leq x \leq \infty$;
2) Ions and background neutral particles are at the same temperature $T_{neutral}(x) = T_i(x) = T(x)$;
3) Net production (or loss) of charged particles $\dot{n}(x)$, is included via rate expressions for electron impact ionization and three-body recombination on electrons;
4) Charged particle inertia is neglected due to the highly collisional nature of the plasma;
5) There is no external magnetic field, and such fields due to plasma currents are neglected;
6) A net current to or from the electrode is allowed, and is assumed to be due to an applied potential between the electrode and the distant plasma; and
7) The electrode surface is assumed to absorb incident electrons and ions. No electron- or ion-emission mechanism is specifically imposed, but such emission as is required by the solution is assumed to be provided by thermionic emission of electrons or surface ionization of positive ions.

To keep the model as general as possible, all variables are written in non-dimensional form (denoted with an overbar). Then the governing equations are written:

Mass Conservation

$$\frac{d\overline{\Gamma}_i}{d\overline{x}} = \overline{\dot{n}} = \overline{n}_e \overline{T}_e^{-9/2} \left\{ \overline{T}_e^{3/2} \exp\left[\overline{\epsilon}_i \left(1 - \frac{1}{\overline{T}_e} \right) \right] - \overline{n}_e \overline{n}_i \right\} \tag{2.1a}$$

$$\frac{d\overline{\Gamma}_e}{d\overline{x}} = \overline{\dot{n}} \tag{2.1b}$$

Momentum Conservation

$$\frac{d\overline{n}_i}{d\overline{x}} = -\frac{\overline{n}_i}{\overline{T}} \left(\frac{d\overline{T}}{d\overline{x}} - \overline{E} \right) - \frac{4}{1+\mu} \frac{\overline{\Gamma}_i}{\overline{T}} \tag{2.2a}$$

$$\frac{d\overline{n}_e}{d\overline{x}} = -\frac{\overline{n}_e}{\overline{T}_e} \left(\frac{d\overline{T}_e}{d\overline{x}} + \overline{E} \right) - \frac{4\mu}{1+\mu} \frac{\overline{\Gamma}_e}{\overline{T}_e} \tag{2.2b}$$

Poisson's Equation

$$\frac{d\overline{E}}{d\overline{x}} = \frac{1}{\epsilon^2} (\overline{n}_i - \overline{n}_e) \tag{2.3}$$

Electron Energy Conservation

$$\begin{aligned} -\frac{6}{5} \frac{d}{d\overline{x}} \left(\overline{n}_e \overline{T}_e \frac{d\overline{T}_e}{d\overline{x}} \right) + \frac{5\mu}{1+\mu} \frac{d}{d\overline{x}} (\overline{\Gamma}_e \overline{T}_e) + \frac{2\mu}{1+\mu} \overline{\Gamma}_e \overline{E} \\ = -\frac{6\mu}{1+\mu} \Theta \overline{n}_e (\overline{T}_e - \overline{T}) - \overline{\epsilon}_i \frac{2\mu}{1+\mu} \overline{\dot{n}} \end{aligned} \tag{2.4}$$

with the two ancillary relations

Current Conservation

$$\overline{J} \equiv \overline{J}_e + \overline{J}_i = \frac{4\mu}{(1+\mu)^2} (\overline{\Gamma}_i - \overline{\Gamma}_e) \tag{2.5}$$

and

Potential

$$\overline{\Phi}(\overline{x}) \equiv -\int_0^{\overline{x}} \overline{E}(\varsigma)\, d\varsigma \tag{2.6}$$

The variables are non-dimensionalized as follows:

$$
\begin{array}{ll}
\bar{x} \equiv x/\ell_R & \bar{\dot{n}}(\bar{x}) \equiv \dot{n}(x)/\dot{n}_R \\
\bar{n}_i(\bar{x}) \equiv n_i(x)/n_R & \bar{n}_e(\bar{x}) \equiv n_e(x)/n_R \\
\bar{\Gamma}_i(\bar{x}) \equiv \Gamma_i(x)/\Gamma_R & \bar{\Gamma}_e(\bar{x}) \equiv \Gamma_e(x)/\Gamma_R \\
\bar{E}(\bar{x}) \equiv E(x)/E_R & \bar{\Phi}(\bar{x}) \equiv \Phi(x)/\Phi_R \\
\bar{T}_e(\bar{x}) \equiv T_e(x)/T_{e_R} & \bar{T}(\bar{x}) \equiv T(x)/T_{e_R} \\
\multicolumn{2}{c}{\bar{J} \equiv J/J_R}
\end{array}
\tag{2.7}
$$

with the reference quantities:

$$\ell_R = \text{Ion Recombination Length}$$

$$\equiv \sqrt{2\, D_a/\beta(T_{e_R})\, n_R^2} \tag{2.8a}$$

$$n_R = \begin{array}{c}\text{Zero Current, Far-Field, Equilibrium} \\ \text{Charged Particle Concentration}\end{array}$$

$$\equiv n_{i,e}(x \to \infty, J = 0) \tag{2.8b}$$

$$\dot{n}_R \equiv \beta(T_{e_R})\, n_R^3 \tag{2.8c}$$

$$\Gamma_R \equiv 2\, D_a\, n_R/\ell_R \tag{2.8d}$$

$$T_{e_R} \equiv \text{Zero Current, Far-Field, Electron Temperature} \tag{2.8e}$$

$$E_R \equiv k\, T_{e_R}/e\, \ell_R \tag{2.8f}$$

$$\Phi_R \equiv k\, T_{e_R}/e \tag{2.8g}$$

$$J_R \equiv \sigma_R\, E_R \tag{2.8h}$$

and

$$\sigma_R \equiv n_R\, e\, (\mu_i + \mu_e) \tag{2.8i}$$

where $D_a = (D_i\,\mu_e + D_e\,\mu_i)/(\mu_i + \mu_e)$ is the ambipolar diffusion coefficient and $\beta(T_e) = 1.09 \times 10^{-20}\, T_e^{-9/2}\ \mathrm{m}^6/\mathrm{sec}$ is the three-body (electron) recombination coefficient.

Nine free parameters must be specified: 1) the ion/electron mobility ratio $\mu \equiv \mu_i/\mu_e \ll 1$, a function of the type of ion and background gas;

2) $\epsilon \equiv \lambda_D/\ell_R \ll 1$, the ratio of the Debye length $\lambda_D \equiv \sqrt{\epsilon_0 k T_{e_R}/n_R e^2}$ to the ion recombination length; 3) $\Theta \equiv m_e \nu_{en}\delta/[m_n \beta(T_{e_R})\, n_R^2]$, the ratio of the elastic to ionizing collision frequencies weighted by the average factional energy loss in electron-neutral collisions, where m_n is the *mass of the neutral particles and* ν_{en} is the electron-neutral collision frequency; 4)the total current density $\overline{J}$, where $\overline{J} < 0$ for cathodes and $\overline{J} > 0$ for anodes; 5) the non-dimensional ionization energy , $\overline{\epsilon}_i \equiv \epsilon_i/kT_{e_R}$, where ϵ_i is the ionization energy for the ionizing species and k is Boltzmann's constant; 6) $\overline{T}(\overline{x}) \equiv T(x)/T_{e_R}$, the non-dimensional temperature of the ion and background neutral particles, which is normalized on the reference temperature T_{e_R}; and 7) boundary values for the quantities $\overline{n}_i(0)$, $\overline{n}_e(0)$ and either $\overline{T}_e(0)$ or $d\overline{T}_e/d\overline{x}|_0$.

B. Boundary Conditions

The governing equations comprise a seventh-order, coupled, non-linear set of ordinary differential equations, so seven boundary conditions are required. Four values are known in the far field, $\overline{x} \rightarrow \infty$. They are the *particle fluxes* $\overline{\Gamma}_{i_\infty}$ *and* $\overline{\Gamma}_{e_\infty}$, *the electric field* $\overline{E}_\infty$, and the electron temperature $\overline{T}_{e_\infty}$. Three remaining boundary conditions are set at the electrode surface, $\overline{x} = 0$, and include the charged particle concentrations ($\overline{n}_i(0)$, $\overline{n}_e(0)$) and either the electron temperature $\overline{T}_e(0)$ or the electron temperature gradient ($d\overline{T}_e/d\overline{x}|_0$).

To evaluate the far-field conditions, we recognize that far from the electrode surface the plasma is uniform and the electrons and ions are in equilibrium. The charged particle concentrations are assumed equal, $\overline{n}_e(\overline{x} \rightarrow \infty) = \overline{n}_i(\overline{x} \rightarrow \infty) \equiv \overline{n}_\infty$, and may be calculated from the Saha equation

$$\overline{n}_\infty = \overline{T}_{e_\infty}^{3/4} \sqrt{\exp\left[\overline{\epsilon}_i\left(1 - \frac{1}{\overline{T}_{e_\infty}}\right)\right]} \tag{2.9}$$

where $\overline{T}_{e_\infty} = T_e(\overline{x} \rightarrow \infty, \overline{J})/T_{e_R}$. Equation (2.9) is necessary because $\overline{n}_{e,i}(\overline{x})$ and $\overline{T}_e(\overline{x})$ are normalized on their values for $\overline{x} \rightarrow \infty$ and $\overline{J} = 0$, that is $\overline{T}_{e_\infty} = \overline{n}_\infty = 1$ *for* $\overline{J} = 0$. *Both* $\overline{T}_{e_\infty}$ *and* $\overline{n}_\infty$ *may be* > 1 *for* $\overline{J} \neq 0$ *as a result of* Joule heating ($\overline{J} \cdot \overline{E}$). The flux and electric field boundary conditions are then

$$\overline{\Gamma}_{i_\infty} = \frac{1+\mu}{4}\overline{J} \tag{2.10a}$$

$$\overline{\Gamma}_{e\infty} = \frac{1+\mu}{4\mu}\overline{J} \qquad (2.10b)$$

$$\overline{E}_{\infty} = \frac{\overline{J}}{\overline{n}_{\infty}} \qquad (2.11)$$

At the electrode surface, $\overline{x} = 0$, for a species which is perfectly absorbed (no reflection or emission), the usual continuum boundary condition for a diffusion-type equation is to let $\overline{n}_{i,e}(0) = 0$. As is well known, this boundary condition is strictly invalid because, for a non-zero flux at the boundary $\left(\overline{\Gamma}(0) \neq 0\right)$, the mean velocity becomes infinite. The diffusion equation fails within a distance on the scale of the mean free path, and a kinetic description is necessary to treat the Knudsen layer where the velocity distribution changes from a nearly isotropic form to a purely one-sided form as the boundary is approached. Such an analysis [2.1] shows that the exact solution is well modeled by the diffusion equation with the boundary condition $\overline{n}(0) = 0$ applied at a position approximately one mean free path outside the physical boundary. Within the continuum approximation, the mean free path is implicitly assumed to be much smaller than any other length scale of interest, and the boundary condition is normally applied right at the physical boundary. In the present problem, use of the boundary condition $\overline{n}_{e,i}(0) = 0$ for an absorbing electrode implies that the mean free path is much smaller than the sheath thickness. This requirement is satisfied for many plasmas of practical interest.

Letting $\overline{n}_e(0) = 0$ does, however, lead to difficulty with regard to the electron temperature and the electron energy equation. As $\overline{n}_e \rightarrow 0$, the electron thermal conductivity goes to zero and the electron energy equation terms for thermal conduction and collisional energy exchange with the background neutral particles both vanish. $\overline{n}_e = 0$ is a regular singular point for this equation, since the thermal conduction term contains the highest derivative in the electron energy equation. The fundamental problem is that for a perfectly absorbing electrode where $\overline{n}_e(0) = 0$, the electron velocity is one-sided and the concept of temperature is no longer valid. This problem and the electron temperature boundary conditions will be addressed more completely when we discuss the solutions which include the electron energy equation ,eq. (2.4). Use of the condition $\overline{n}_e(0) = 0$ is quite acceptable within the isothermal limit where $\overline{T}_e(\overline{x})$ is assumed to be known, and the electron energy equation may be neglected.

When there is electron emission or ion emission from the electrode, the boundary condition generally corresponds to $\overline{n}_{i,e}(0) > 0$. The value of $\overline{n}_{i,e}(0)$ can be related to the emission current density by the following approximate argument, which is discussed on a dimensional basis, for the case of electrons.

The electron velocity distribution at any point may be represented as the sum of an outwardly-directed half-Maxwellian of concentration $n_e^+(x)$ and an inwardly-directed half-Maxwellian of concentration $n_e^-(x)$, so that

$$n_e(x) = n_e^+(x) + n_e^-(x). \tag{2.12}$$

The outwardly and inwardly directed random fluxes are then $n_e^+(x)\,[\overline{c}_e(x)/2]$ and $n_e^-(x)\,[\overline{c}_e(x)/2]$ where $\overline{c}_e(x) \equiv \sqrt{8\,kT_e(x)/\pi\,m_e}$ is the mean thermal speed. Hence the net flux is

$$\Gamma_e(x) = \left(n_e^+(x) - n_e^-(x)\right)\frac{\overline{c}_e(x)}{2}. \tag{2.13}$$

From eqs. (2.12-2.13) we find

$$n_e^+(x) = \frac{1}{2}\left[n_e(x) + \frac{\Gamma_e(x)}{(\overline{c}_e(x)/2)}\right] \tag{2.14a}$$

and

$$n_e^-(x) = \frac{1}{2}\left[n_e(x) - \frac{\Gamma_e(x)}{(\overline{c}_e(x)/2)}\right]. \tag{2.14b}$$

Using the definition $\Gamma_e(x) \equiv n_e(x)\,v_e(x)$, where $v_e(x)$ is the electron mean velocity, the condition that n_e^+ and $n_e^- \geq 0$ requires that $|v_e(x)| \leq \overline{c}_e(x)/2$, a requirement which is usually met for conditions of interest. At the electrode surface, $x = 0$,

$$n_e^+(0) = \frac{1}{2}\left[n_e(0) + \frac{\Gamma_e(0)}{(\overline{c}_e(0)/2)}\right]. \tag{2.15}$$

The positively directed flux at the electrode surface is

$$\Gamma_e^+(0) = n_e^+(0)\,\frac{\overline{c}_e(0)}{2} = \frac{1}{2}\left[n_e(0)\,\frac{\overline{c}_e(0)}{2} + \Gamma_e(0)\right] \tag{2.16}$$

and the emitted current density is

$$J_e^+(0) = -\frac{e}{2}\left[n_e(0)\,\frac{\overline{c}_e(0)}{2} + \Gamma_e(0)\right]. \tag{2.17}$$

Note that at positions other than $x = 0$, it is not possible to identify Γ_e^+ as due to emitted electrons because of the interchange of Γ_e^+ and Γ_e^- due to collisions. An equivalent expression for the electron emission flux was derived by Kalnavarns and Bienkowski [2.2] by a different approximate argument.

Physically, $J_e^+(0)$ is the electron emission saturation current density given by the Richardson-Dushman law

$$J_e^+ = -A T_{electrode}^2 \exp -(\phi_w / k T_{electrode}) \tag{2.18}$$

where ϕ_w is the surface work function, $T_{electrode}$ is the electrode temperature, and $A \approx 1.2 \times 10^6\,\mathrm{A/m^2\,K^2}$. Equation (2.18) is applicable when the electric field at the electrode is zero or decelerating ($E(0) \geq 0$). When there is an accelerating field at the electrode ($E(0) < 0$), field enhanced emission due to the Schottky effect [2.3] is applicable:

$$J_e^+ = -A T_{electrode}^2 \exp - \left\{ \left[\phi_w - \sqrt{-e^3 E(0) / 4\pi\epsilon_0} \right] / k T_{electrode} \right\} \tag{2.19}$$

$$\approx J_{e0}^+ \exp\left(0.44 \sqrt{-E(0)} / T_{electrode}\right) \tag{2.19a}$$

where J_{e0}^+ is the emission given by eq. (2.18). In practice, extremely large electric fields are required to significantly enhance the electron emission.

C. Solutions

The above equations and boundary conditions completely define the behavior of the electrons and ions for the diffuse discharge with or without charged particle emission by the electrode. The solutions to these equations describe the spatial profiles for the charged particle concentrations and fluxes, the electric field, and the electron temperature as a function of the nine free parameters. This is a notable quantity of information. It is important to keep in mind that from a practical standpoint, the current-voltage characteristics are what is usually measured, and that we are really trying to determine how the current-voltage characteristics depend on the plasma and electrode conditions (the free parameters).

Our approach was first to simplify the governing equations to a level for which an analytical solution could be found. The simplifying assumptions were then relaxed in three steps, and the effect of each assumption on the solution was observed.

The problem was solved in the following four limits:

1) **Isothermal, Quasi-Neutral Plasma (no Sheath)** – Poisson's equation and the electron energy equation are neglected, and the mass and momentum conservation equations are simplified.
2) **Isothermal Plasma** – The electron energy equation is neglected but Poisson's equation is retained and the sheath is included in the solution.
3) **Non-Isothermal Plasma, Simplified Energy Equation** – The electron energy equation is included in a simplified form which does not include energy transfer due to conduction, convection and ionization/recombination. The background gas is assumed isothermal, but the electron temperature may vary.
4) **Non-Isothermal Plasma, Complete Set of Equations** – The complete system of equations defined by eqs. (2.1–2.4) is solved for an isothermal background gas.

C.1 Isothermal, Quasi-Neutral Solution (Analytic)

If we consider an isothermal plasma where the electrons, ions, and neutral particles all remain at the same temperature, the electron energy equation is redundant and may be neglected. This approximation is valid so long as the net current density is small and there is little Joule heating of the electrons, or the collisional coupling between the electron and the background neutral particles is strong ($\Theta \rightarrow \infty$).

We also require the plasma conditions be such that the sheath is infinitely thin, that is, $\epsilon \rightarrow 0$. In this case, $\bar{n}_i(x) = \bar{n}_e(x) = \bar{n}(x)$ throughout, Poisson's equation may be neglected, and the solution does not include the sheath.

The mass and momentum conservation equations simplify to

$$\frac{d\bar{\Gamma}_i}{d\bar{x}} = \bar{\dot{n}} = \bar{n}\,(1 - \bar{n}^2) \qquad (2.20a)$$

$$\frac{d\bar{\Gamma}_e}{d\bar{x}} = \bar{\dot{n}} \qquad (2.20b)$$

and

$$\Gamma_i = \frac{1+\mu}{4}\left(\bar{n}\bar{E} - \frac{d\bar{n}}{d\bar{x}}\right) \tag{2.21a}$$

$$\Gamma_e = \frac{1+\mu}{4\mu}\left(-\bar{n}\bar{E} - \frac{d\bar{n}}{d\bar{x}}\right). \tag{2.21b}$$

Eliminating the fluxes between (2.20) and (2.21) yields

$$-\frac{d\,(\bar{n}\bar{E})}{\bar{x}} - \frac{d^2\bar{n}}{d\bar{x}^2} = \frac{4\mu}{1+\mu}\left[\bar{n}\,(1-\bar{n}^2)\right] \tag{2.22a}$$

$$\frac{d\,(\bar{n}\bar{E})}{\bar{x}} - \frac{d^2\bar{n}}{d\bar{x}^2} = \frac{4}{1+\mu}\left[\bar{n}\,(1-\bar{n}^2)\right] \tag{2.22b}$$

which may be added to produce a single nonlinear equation for $\bar{n}$:

$$\frac{d^2\bar{n}}{d\bar{x}} + 2\bar{n}\,(1-\bar{n}^2) = 0, \tag{2.23}$$

subject to the boundary conditions $\bar{n}(0) = 0$ (no particle emission at the electrode) and $\bar{n} \to 1$ for $\bar{x} \to \infty$.

The solution to eq. (2.23) is

$$\bar{n}(\bar{x}) = \tanh(\bar{x}), \tag{2.24}$$

shown in Fig. 2.2. The net generation rate is given by

$$\bar{\dot{n}}(\bar{x}) = \mathrm{sech}^2(\bar{x})\,\tanh(\bar{x}) \tag{2.25}$$

which, as shown in Fig. 2.2 is zero for $\bar{x} = 0$ and $\bar{x} \to \infty$. The center of the ionization nonequilibrium region is located at $\bar{x} = \tanh^{-1}(3^{-1/3}) \sim 0.658$, where the net generation rate has a maximum value of $(2/3)^3/2 \sim 0.385$. We shall find later that the magnitude of the total net generation rate in the boundary layer determines the saturation current for both anodes and cathodes in the absence of emission. We note, for reference, that both $\bar{n}(\bar{x})$ and $\bar{\dot{n}}(\bar{x})$ are independent of μ and $\bar{J}$, and that

$$\begin{matrix}\text{Total Net}\\ \text{Generation Rate}\end{matrix} \equiv \int_0^\infty \bar{\dot{n}}(\bar{x})\,d\bar{x} = \frac{1}{2}. \tag{2.26}$$

The other dependent variables are found by back-substituting the solution for $\bar{n}(\bar{x})$ into eqs. (2.20-2.21). The electric field is given by

$$\bar{E}(\bar{x}) = \left[-\left(\frac{1-\mu}{1+\mu}\right)\mathrm{sech}^2(\bar{x}) + \bar{J}\right]\coth(\bar{x}) \tag{2.27}$$

which may be separated into two components: an ambipolar field which decreases exponentially with $\bar{x}$, and a resistive component which is

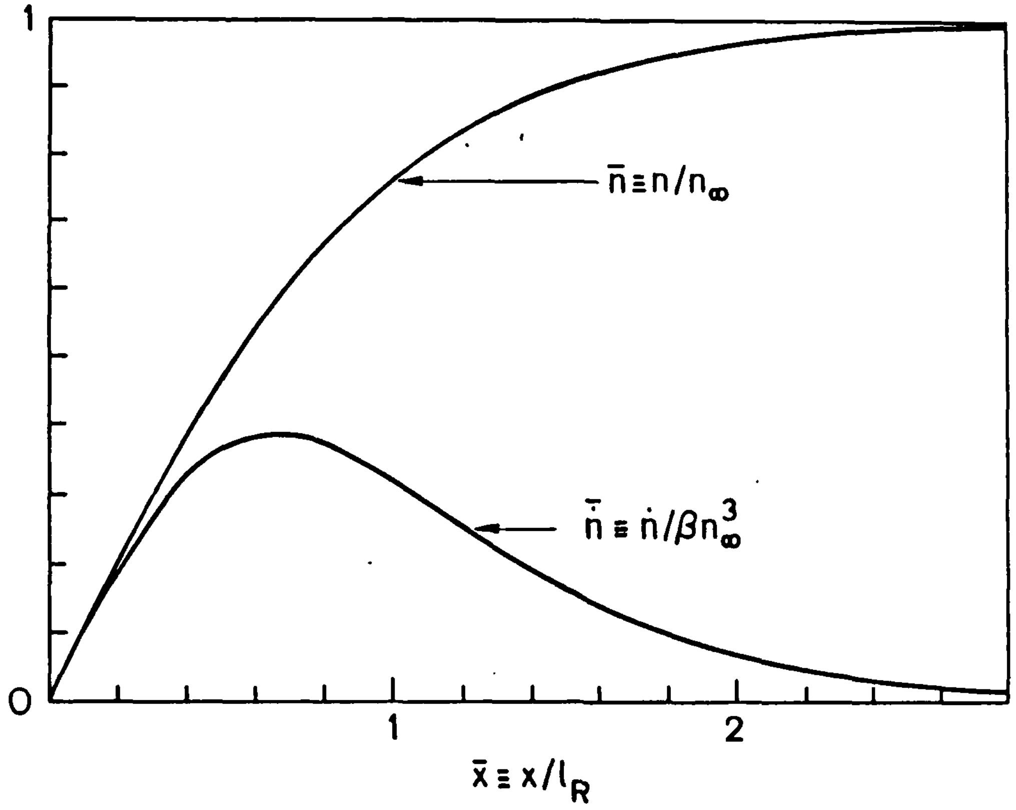

Fig. 2.2. Profiles of normalized charged particle concentrations and net generation rate.

necessary to drive the current through the plasma. Both components have a simple pole at $\bar{x} = 0$ due to the $\coth(\bar{x})$ factor.

The ambipolar field is always negative, i.e., directed towards the electrode. The resistive field is in the same direction for a cathode ($\bar{J} < 0$), but in the opposite direction for an anode ($\bar{J} > 0$). If $\bar{J}$ is positive and large enough, the field at the anode can become positive. Conventionally, in gas discharge terminology, this is termed a transition from a negative anode fall to a positive one. The condition for this to happen is

$$\bar{J} \geq \bar{J}_I \equiv \frac{1-\mu}{1+\mu} \approx 1. \tag{2.28}$$

The potential is given by

$$\bar{\Phi}(\bar{x}) = \left(\frac{1-\mu}{1+\mu}\right) \ln \tanh(\bar{x}) - \bar{J} \ln \sinh(\bar{x}) \tag{2.29}$$

with the limiting forms

$$\overline{\Phi}(\overline{x}) \rightarrow \left[\frac{1-\mu}{1+\mu} - \overline{J}\right] \ln(\overline{x}) \qquad \text{for } \overline{x} \ll 1 \tag{2.30a}$$

and

$$\overline{\Phi}(\overline{x}) \rightarrow -\overline{J}\left(\overline{x} - \ln 2\right) \qquad \text{for } \overline{x} \gg 1 \tag{2.30b}$$

where the zero of potential has been taken at $\overline{x} \rightarrow \infty$ for $\overline{J} = 0$ because of the logarithmic singularity at $\overline{x} = 0$. Potential profiles for both cathodes and anodes are shown in Fig. 2.3, which includes cases for which the anode fall is negative $(0 > \overline{J} > \overline{J}_I)$ and positive $(\overline{J} > \overline{J}_I \approx 1)$. The curves are asymptotic to the broken lines ,eq. (2.30*b*), whose slopes represent the electric field $\overline{E}_{\infty} = \overline{J}$ in the distant plasma.

The solutions for the electron and ion fluxes are also composed of two terms

$$\overline{\Gamma}_i(\overline{x}) = -\frac{1}{2}\left[\operatorname{sech}^2(\overline{x}) - \frac{1+\mu}{2}\overline{J}\right] \tag{2.31a}$$

$$\overline{\Gamma}_e(\overline{x}) = -\frac{1}{2}\left[\operatorname{sech}^2(\overline{x}) + \frac{1+\mu}{2\mu}\overline{J}\right]. \tag{2.31b}$$

The first term represents the equal ambipolar fluxes to the electrode; this flux is independent of the current density and originates from the net generation of electron-ion pairs in the ionization nonequilibrium layer. The second term represents the fluxes associated with the current. The saturation behavior of the electrode current-voltage characteristics may be explained by considering eqs. (2.31) in more detail.

For a cathode $(\overline{J} < 0)$, the ion flux is always directed towards the cathode and increases with current magnitude. However, the electron flux to the cathode decreases with increasing current magnitude until $\overline{J} \leq -2\mu/(1+\mu)$, at which point there must be a net electron flux leaving the cathode. This means that the cathode must emit electrons for currents greater than the relatively small value $\overline{J}_C$, given by

$$\overline{J}_C \equiv \frac{-2\mu}{1+\mu}. \tag{2.32}$$

$\overline{J}_C$ is interpreted as the cathode saturation current in the absence of electron emission by the cathode.

For $\overline{J} = \overline{J}_C$, the current at the cathode surface is carried entirely by the arriving ion flux, which is only a factor $(1+\mu)$ times the equal

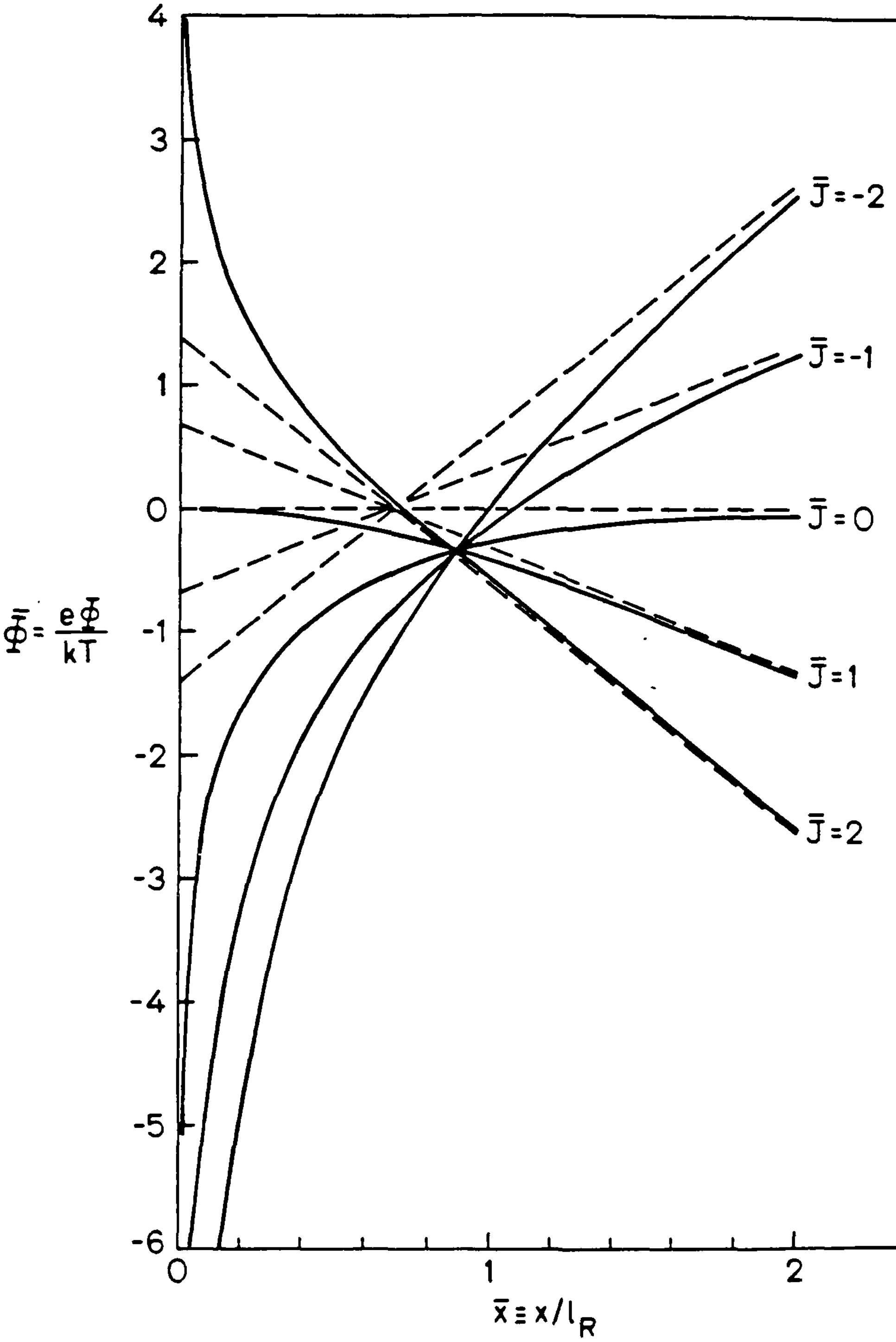

Fig. 2.3. Profiles of normalized potential for several values of normalized current density: $\bar{J} < 0$, cathode; $\bar{J} > 0$, anode. Broken lines indicate the asymptotes corresponding to the uniform electric field in the distant plasma.

electron and ion fluxes arriving at the electrode for zero current. In previous analyses of the cathode sheath in the absence of electron emission [2.4,5], it has often been assumed that the maximum ion flux which can be drawn from the plasma to the electrode is the random one-way flux, $n_\infty \bar{c}_i/4$. The results derived here indicate otherwise.

For a given current density $\overline{J}$, the electron flux in the distant plasma must always be larger that the ion flux by the ratio $(1/\mu)$.

$$\overline{\Gamma}_{i_\infty} = \frac{1+\mu}{4}\overline{J} \qquad \overline{\Gamma}_{e_\infty} = \frac{1+\mu}{4\mu}\overline{J} \tag{2.33}$$

Thus for a cathode ($\overline{J} < 0$) there is an ion flux drawn out of the distant plasma toward the cathode, and a much larger electron flux drawn away from the cathode into the plasma. By mass conservation,

$$\overline{\Gamma}_{e_\infty} = \overline{\Gamma}_e(0) + \int_0^\infty \bar{\dot{n}}\, d\bar{x}. \tag{2.34}$$

At the critical current density $\overline{J}_C$, in the absence of electron emission, $\overline{\Gamma}_e(0) = 0$, so that

$$\overline{\Gamma}_{e_\infty} = \int_0^\infty \bar{\dot{n}}\, d\bar{x}. \tag{2.35}$$

Physically, this means that for $\overline{J} = \overline{J}_C$ the total net generation rate of electrons in the ionization nonequilibrium layer is used to supply the electron flux in the distant plasma. As discussed previously, the total net generation rate is given by

$$\begin{matrix}\text{Total Net}\\ \text{Generation Rate}\end{matrix} = \int_0^\infty \bar{\dot{n}}(\bar{x})\, d\bar{x} = \frac{1}{2} \tag{2.26}$$

and is independent of $\overline{J}$. Thus the maximum electron flux in the distant plasma, in the absence of electron emission, is $\overline{\Gamma}_{e_\infty} = 1/2$, corresponding to a maximum current of $(-\overline{J}) = 2\mu/(1+\mu)$.

It is clear that the current limitation is caused not by a limitation on the flux of *ions* which may be drawn to the cathode *from* the plasma, but by a limitation on the total net generation rate of electrons-ion pairs in the ionization nonequilibrium layer which supply the *electron* flux *to* the distant plasma.

In the case of an anode, a similar current limitation phenomenon arises. For an anode ($\overline{J} > 0$) the electron flux is always directed towards the electrode and increases with increasing current density. The ion flux decreases with increasing current until for $\overline{J} \geq 2/(1+\mu)$, a current approximately twice $\overline{J}_I$ for the transition to a positive anode fall, there is a net flux of ions leaving the anode. This implies that the anode must emit ions for currents greater than

$$\overline{J}_A \equiv \frac{2}{1+\mu}. \tag{2.36}$$

For $\overline{J} = \overline{J}_A$ the current at the anode surface is carried entirely by the arriving electron flux which is a factor $(1+\mu)/\mu \sim 1/\mu \gg 1$ times the arriving electron flux in the absence of current.

The physical reason for this limitation parallels that for the current limitation in the case of a cathode. In the distant plasma, a given current implies an ion flux $\overline{\Gamma}_{i_\infty} = (1+\mu)\overline{J}/4$ directed away from the anode. In the absence of ion emission by the anode, the flux in the distant plasma must originate from ions generated in the ionization nonequilibrium layer. Hence, the maximum ion flux in the distant plasma is limited by the total net generation rate of electron-ion pairs in this layer, and the maximum current which corresponds to this maximum ion flux is given by $\overline{J}_A$.

Thus, the anode current limitation is not set by a limitation on the flux of electrons that can be drawn to the anode from the plasma, but by a limitation on the ion current in the distant plasma set by the total net generation rate of ions in the ionization nonequilibrium layer. Cheng et al. [2.6] recognize this current limitation, and derive an equivalent expression for the value of saturation current.

To summarize, in the absence of charged particle emission by the electrode, current saturation occurs due to a limitation on the flux of charged particles drawn away from the electrode in the distant plasma, set by the finite supply of particles generated in the ionization nonequilibrium region.

In general, a fraction of the repelled species (electrons for cathodes, ions for anodes) which are generated in the ionization nonequilibrium layer are drawn to the electrode, with the remaining particles drawn into the plasma. The saturation currents $\overline{J}_C = -2\mu/(1+\mu)$ and $\overline{J}_A = 2/(1+\mu)$ are the limiting cases whereby the total net generation rate in the ionization nonequilibrium layer is used to supply the repelled particle flux in the distant plasma (directed away from the electrode). A third notable case occurs for the absence of current, $\overline{J} = 0$, where the total net generation rate supplies the equal ion and electron fluxes to the electrode, since there is no net flux in the distant plasma. We have also found that the sign of the electric field at the surface of the electrode changes for $\overline{J} = \overline{J}_I = (1-\mu)/(1+\mu) \sim 1$, which is approximately half the value of the anode saturation current.

Note that these critical currents $\overline{J}_C, \overline{J}_A$ and $\overline{J}_I$ depend only on the mobility ratio μ. In the limit of $\mu \to 1$, the anode and cathode saturation behavior becomes symmetric in $\overline{J}$ (i.e., $\overline{J}_A \to |\overline{J}_C| \to 1$), and the surface electric field changes sign for $\overline{J} = 0$.

While much has been learned from the quasi-neutral solution, it is unable to describe the sheath, and hence cannot be used to calculate current-voltage characteristics, for which solutions which include Poisson's equation, are required.

C. Isothermal Solution (Numerical)

In this part, we consider $\epsilon \neq 0$. Poisson's equation is included in the set of governing equations, and the solution includes the sheath. We still assume an isothermal plasma for which the electrons, ions and neutral particles all remain at the same temperature $(\overline{T}_e(\overline{x}) = \overline{T}(\overline{x}) = 1)$, and we neglect the electron energy equation.

Letting $(\overline{T}_e(\overline{x}) = \overline{T}(\overline{x}) = 1)$ simplifies the continuity and momentum equations significantly from eqs. (2.1-2.2). The governing equations reduce to

Mass Conservation

$$\frac{d\overline{\Gamma}_i}{d\overline{x}} = \overline{\dot{n}} = \overline{n}_e\,(1 - \overline{n}_e\overline{n}_i) \tag{2.37a}$$

$$\frac{d\overline{\Gamma}_e}{d\overline{x}} = \overline{\dot{n}} \tag{2.37b}$$

Momentum Conservation

$$\frac{d\overline{n}_i}{d\overline{x}} = \overline{n}_i\overline{E} - \frac{4}{1+\mu}\overline{\Gamma}_i \tag{2.38a}$$

$$\frac{d\overline{n}_e}{d\overline{x}} = -\overline{n}_e\overline{E} - \frac{4\mu}{1+\mu}\overline{\Gamma}_e \tag{2.38b}$$

and

Poisson's Equation

$$\frac{d\overline{E}}{d\overline{x}} = \frac{1}{\epsilon^2}\,(\overline{n}_i - \overline{n}_e) \tag{2.3}$$

along with the five free parameters $\overline{n}_i(0)$, $\overline{n}_e(0)$, $\overline{J}$, $\epsilon = \lambda_D/\ell_R$ and $\mu = \mu_i/\mu_e$.

These equations were solved numerically by the method of quasilinearization, combined with orthonormalization and superposition. Use of a numerical method required that the far-field boundary ($\overline{x} \rightarrow \infty$) be located at a finite value of $\overline{x}$. We chose a position located sufficiently far into the plasma (at $\overline{x} = \overline{x}_b$ say $\gg 0.658$) to ensure quasi-neutrality, and well past the ionization nonequilibrium layer, i.e., where $\overline{n} \ll 1$. Equations (2.27,2.31) are then used with $\overline{x} = \overline{x}_b$ ($\sim$ typically 5) for the boundary values of the dependent variables $\overline{E}_\infty, \overline{\Gamma}_{e_\infty}$ and $\overline{\Gamma}_{i_\infty}$.

A solution database has been generated for a wide range of the parameters $\overline{J}, \epsilon$, and μ, and for several values of ion and electron emission by the electrode. Our aim has been to observe how charged particle emission by the electrode and the presence of the sheath modify the conclusions drawn from the quasi-neutral solution.

The results have been organized into three major areas: (*i*) an electrically isolated (floating) electrode ($\overline{J} = 0$) with and without electron emission; (*ii*) a cathode ($\overline{J} < 0$) with and without electron emission; and (*iii*) an anode ($\overline{J} > 0$) with and without ion emission.

We shall examine only the results for the critical currents discussed in the previous section. For illustrative purposes, we choose to discuss solutions for $\epsilon = 10^{-1}$. This permits both the sheath and the ionization nonequilibrium layer to be displayed together on a linear scale. Atmospheric pressure plasmas of practical interest tend to have much smaller values of ϵ, so we have computed solutions in the range $10^{-3} < \epsilon < 10^{-1}$. Comments made about the solutions for $\epsilon = 10^{-1}$ apply equally well for smaller values of ϵ, unless stated otherwise. The solutions are also calculated for $\mu = 1/300$, but all of the dependent variables are quite insensitive to the value of μ.

C.2.1 Non-Emitting, Floating ($\bar{J} = 0$) Electrode

This is the familiar case of a non-emitting, perfectly absorbing, insulating surface or floating electrode contacting the plasma. Profiles of $\bar{n}_e, \bar{n}_i$ and $\bar{\dot{n}}$ are compared with their quasi-neutral values $\bar{n}_{QN}$ and $\bar{\dot{n}}_{QN}$ in Fig. 2.4 (a), with the corresponding profiles of $\bar{\Gamma}_e, \bar{\Gamma}_i, \bar{E}$ and $\bar{\Phi}$, shown in Figs. 2.4 (b) and (c).

All of the electrons and ions generated in the ionization nonequilibrium layer flow to the surface and constitute equal (negative) fluxes $\bar{\Gamma}_e$ and $\bar{\Gamma}_i$ at every point. These fluxes increase with decreasing $\bar{x}$. Both $\bar{n}_e$ and $\bar{n}_i$ are significantly lower than $\bar{n}_{QN}$ except that $\bar{n}_i$ exceeds $\bar{n}_{QN}$ in a very thin diffusion layer very close to the surface. Throughout the electrical boundary layer $\bar{n}_i > \bar{n}_e$, so there is a positive ion sheath which merges smoothly with the ionization nonequilibrium layer. Because the profiles of $\bar{n}_e$ and $\bar{n}_i$ differ from that of $\bar{n}_{QN}$, the peak of the net generation rate profile $\bar{\dot{n}}$ is significantly shifted away from the surface, but retains the same general shape. In fact, the total net generation rate is only very slightly changed from the quasi-neutral value of 1/2.

If we (arbitrarily) define the outer edge of the ion sheath $\bar{x}_{is}$ as the point where

$$\Delta \equiv \frac{|\bar{n}_i - \bar{n}_e|}{(\bar{n}_i + \bar{n}_e)/2} = 0.1, \qquad (2.39)$$

then we find $\bar{x}_{is} = 0.85$. Hence, since $\epsilon = 0.1$, the sheath thickness in terms of Debye lengths (of the distant plasma) is 8.5. It is found that as ϵ decreases, the sheath thickness increases as measured in Debye lengths, reaching a value of 36.3 for $\epsilon = 10^{-3}$. This result justifies the use of continuum theory, even when the mean free path for electrons and ions is comparable to or greater than the Debye length, because the sheath is collision dominated.

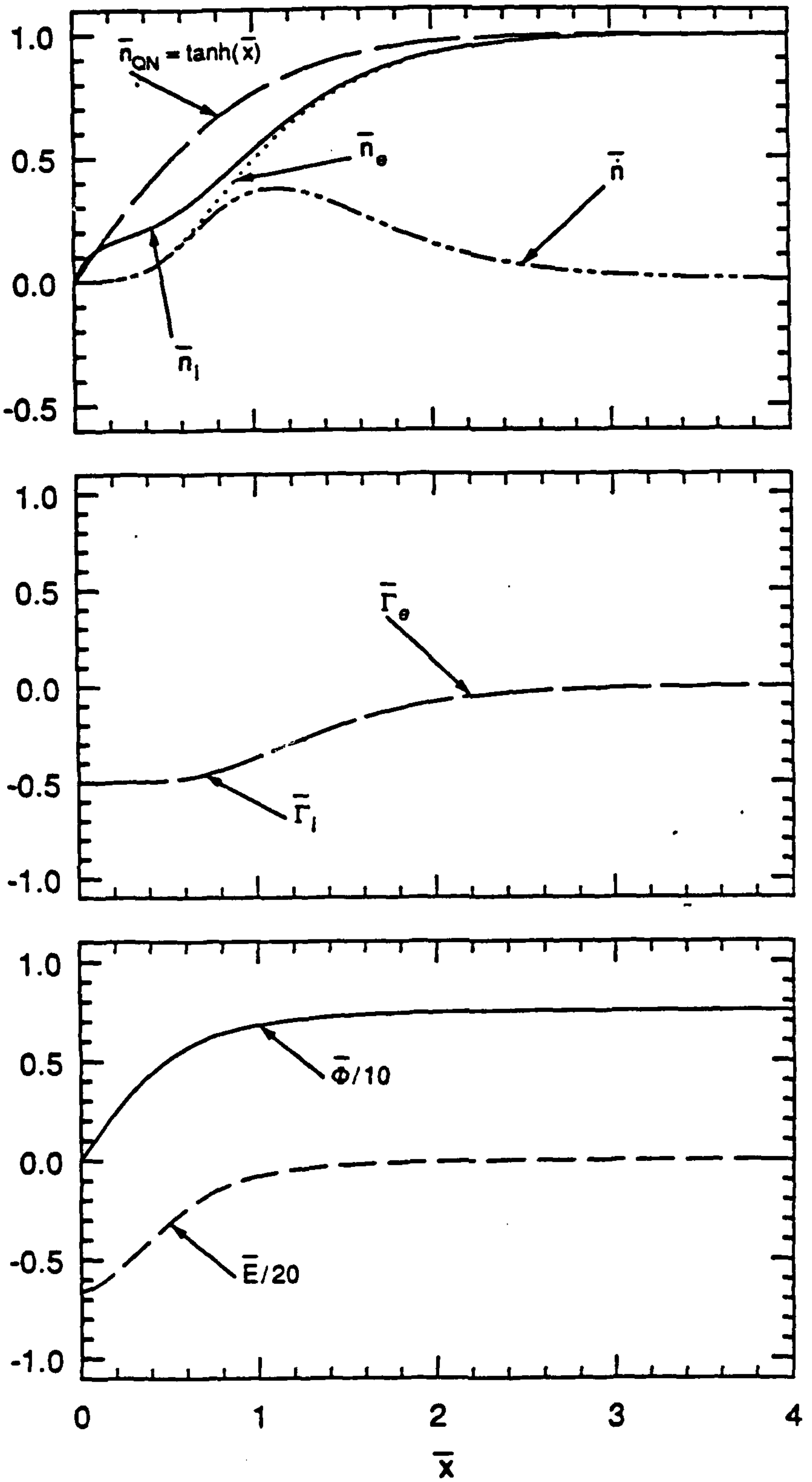

Fig. 2.4. Profiles of the dependent variables for a non-emitting, floating electrode, with the quasi-neutral solution (subscript QN) for comparison. Parameter values $\epsilon = 10^{-1}$, $\bar{J} = 0$, $\bar{n}_e(0) = \bar{n}_i(0) = 0$.

The potential decreases toward the electrode and the total potential drop is -7.33 (kT_∞/e) for $\epsilon = 10^{-1}$. The magnitude of this potential drop increases slowly with decreasing ϵ, reaching a value of -10.6 (kT_∞/e) for $\epsilon = 10^{-3}$.

C.2.2 Electron-Emitting, Floating ($\overline{J} = 0$) Electrode

When the above conditions are modified to allow electron emission ($\overline{n}_e(0) > 0$), an electron sheath forms immediately against the electrode surface, and merges smoothly into the ion sheath further out. The ion sheath is weakened as compared with the non-emitting case, that is $|\overline{n}_i - \overline{n}_e|$ decreases everywhere, and the potential fall decreases in magnitude.

With increasing electron emission, the width and strength of the electron sheath increases while the strength and width of the ion sheath decreases. As a result, the total potential drop decreases dramatically; the electrode floats up towards the plasma potential, becoming equal to it for $\overline{n}(0) = 1$. This behavior is consistent with the use by Langmuir [2.7] and others [2.2,8,9] of a thermionically emitting probe to measure the plasma potential. For a given value of ϵ, there exists a critical value of electron emission, measured by $\overline{n}_{e_{crit}}(0)$, equal to 0.223 for $\epsilon = 10^{-1}$, at which the surface field changes sign from negative to positive and a potential minimum occurs at the electrode surface. As $\overline{n}_e(0)$ is increased above the critical value, the potential minimum moves out from the electrode surface and the depth of the potential well increases. There is also a minimum in $\overline{n}_e$ associated with the potential minimum, due to the fact that electrons approximately satisfy the Boltzmann relation $\overline{n} \propto \exp\overline{\Phi}$. It should also be noted that although the electrode potential floats up to the plasma potential for $\overline{n}_e(0) = 1$, the plasma-sheath is not, by any means, a region of uniform potential and charged particle concentration, as is clear from Fig. 2.5.

To our knowledge, this work represents the first satisfactory quantitative analysis of an emitting, floating electrode, apart from the very approximate treatment originally done by Langmuir. Figure 2.6 shows the total potential drop as a function of electron emission for various values of ϵ. It indicates that except for very small values of emission, the potential drop is independent of ϵ, and that while the electrode

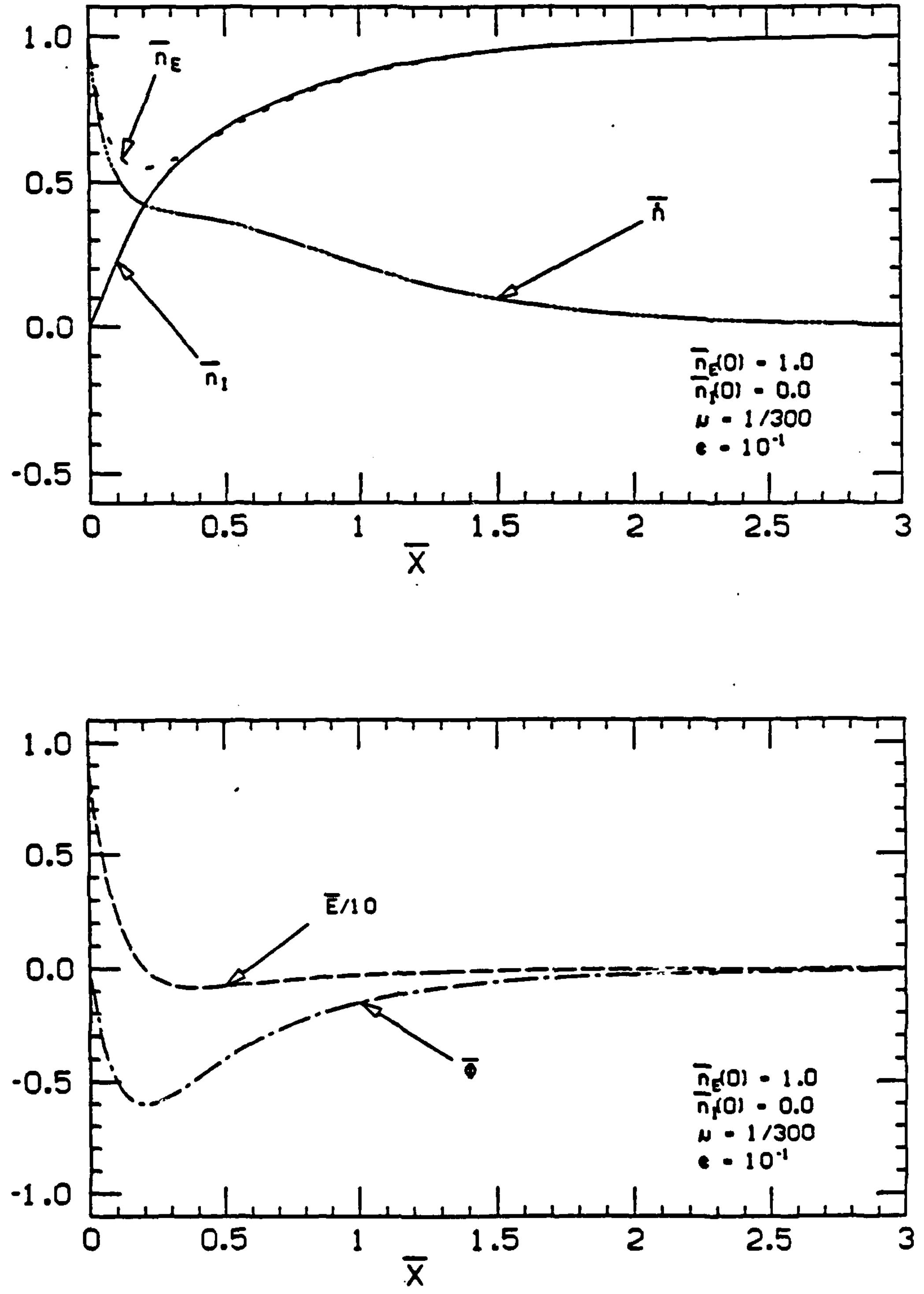

Fig. 2.5. Profiles of $\overline{n}_e$, $\overline{n}_i$, $\overline{n}$, $\overline{E}$ and $\overline{\Phi}$ variables for an electron-emitting, floating electrode. Parameter values are $\epsilon = 10^{-1}$, $\overline{J} = 0$, $\overline{n}_e(0) = 1$ and $\overline{n}_i(0) = 0$.

potential approaches the plasma potential for relatively small values of $\bar{n}_e(0)$, it only tends to exact equality as $\bar{n}_e(0)$ tends to unity.

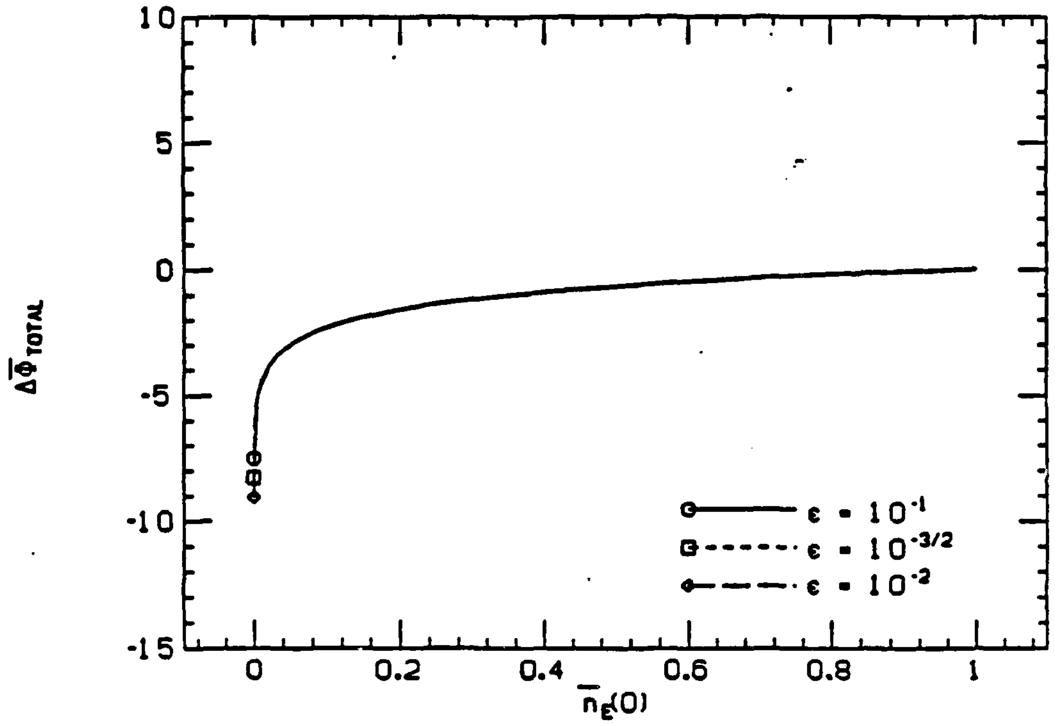

Fig. 2.6. Total potential drop $\Delta\bar{\Phi}_{total}$ as a function of $\bar{n}_e(0)$, for various ϵ. Parameter values $\mu = 1/300, \bar{J} = 0, \bar{n}_i(0) = 0$.

One other, unexpected, result should be mentioned. With increasing electron emission, there is a significant shift of the region of net generation towards the electrode surface, because of the enhanced value of $\bar{n}_e$ in the electron sheath. However, despite the dramatic change in the profile of $\bar{n}$, the total net generation rate remains essentially invariant at the value 1/2 given by the quasi-neutral approximation.

C.2.3 Non-Emitting Cathode

We now consider what happens when a non-emitting electrode draws a net current, or equivalently, is biased more negative with respect to the plasma than its floating potential for $\bar{J} = 0$. Due to resistive losses, the plasma is no longer at a uniform potential, so we define the total potential drop in the layer, $\Delta\overline{\Phi}_{total}$, as the integral of the *space-charge-induced* electric field. In this way, the current-dependent electric field needed to overcome the finite plasma conductivity is neglected. Hence,

$$\Delta\overline{\Phi}_{total} = -\int_0^{\overline{x}_b} [\overline{E}(\overline{x}) - \overline{E}_\infty]\, d\overline{x} \tag{2.40}$$

$$= -\left\{\overline{\Phi}(\overline{x}_b) \quad + \quad \underbrace{\overline{x}_b \overline{E}_\infty}_{\text{Resistive Potential Drop}}\right\} \tag{2.40a}$$

where the zero of potential is taken at the electrode surface ($\overline{\Phi}(0) = 0$). This is shown graphically in Fig. 2.7.

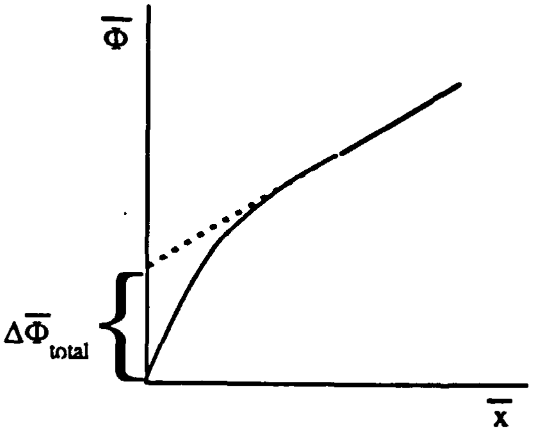

Fig. 2.7. Total potential drop in the boundary layer.

As the current is increased, the ion sheath becomes wider and stronger because the electron concentration has a very small value for greater distances from the surface. At the same time, the (negative) potential fall and sheath field increase and tend to very large values as the saturation current $\overline{J}_C$ is approached. As was noted earlier, in practical terms, the saturation current density for non-emitting cathodes is quite small.

Figure 2.8 shows the solution near saturation, for $\overline{J} \approx \overline{J}_C = -2\mu/(1+\mu)$. A thick, strong ion sheath drives the ionization nonequilibrium region away from the electrode surface and into the plasma. There is negligible net generation within the strong part of the sheath, because of the lack of ionizing electrons. The bulk of the net generation occurs in the weak part of the sheath where it merges into the ionization nonequilibrium layer. This tail would comprise the overlap region for an analysis matching inner and outer expansions, and illustrates the difficulty in trying to match approximate solutions.

All of the dependent variables vary smoothly through the sheath, the ionization nonequilibrium region, and into the uniform distant plasma. The quasi-neutral solution ($\overline{n}_{QN} = \tanh(\overline{x})$) is drawn for reference in the top figure, to show the significant effect that the sheath has on number density profiles throughout the entire boundary layer.

The electron flux at the cathode surface ($\overline{x} = 0$) is essentially zero; the presence of the sheath only perturbs the number density profiles, it does not affect the total net generation rate in the layer. This conclusion is valid, independent of the value of ϵ.

C.2.4 Electron-Emitting Cathode

When electron emission from the cathode is allowed, $\overline{n}_e(0) > 0$, it considerably changes the appearance and behavior of the sheath as compared to a non-emitting cathode. An electron sheath is formed immediately in front of the cathode, and merges smoothly into the ion sheath. The emitted electrons weaken (partially neutralize) the ion sheath, and as a result, the magnitude of the potential fall decreases for a given current.

As $\overline{n}_e(0)$ is increased for a given current $\overline{J}$, the electron sheath becomes stronger and thicker, and one finds a critical value $\overline{n}_{e_{crit}}(\overline{x} = 0, \overline{J})$ for which the electric field at the cathode surface changes sign from negative to positive, and a potential minimum occurs at the electrode surface. As $\overline{n}_e(0)$ is increased further, the potential minimum moves out from the cathode and into the plasma.

The condition whereby $\overline{E}(0) > 0$ is known as (electron) space-charge-limited emission, to distinguish it from emission- (or temperature-) limited emission when $\overline{E}(0) < 0$ and there is no potential minimum. In the space-charge-limited case, the full emission capability of the cathode is not realized. The slower electrons in the half-Maxwellian distribution

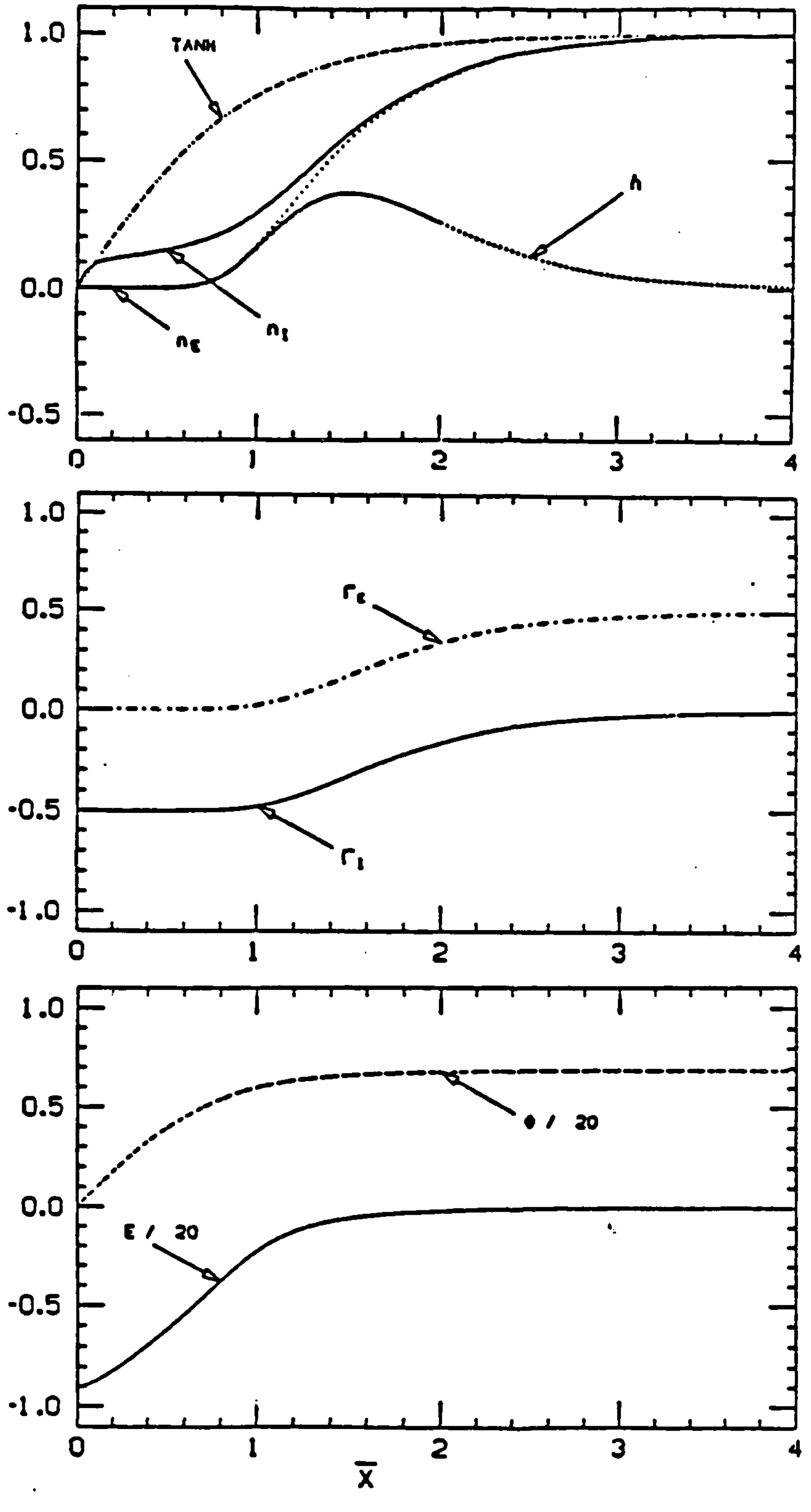

Fig. 2.8. Profiles of the dependent variables for a non-emitting cathode close to saturation. Parameter values $\epsilon = 10^{-1}$, $\overline{J} = -2\mu$, $\overline{n}_e(0) = \overline{n}_i(0) = 0$.

of emitted electrons are reflected by the retarding electric field and are returned to the cathode. Only the electrons with sufficient energy to overcome the potential "hill" presented by the potential minimum are able to contribute to the current leaving the cathode.

For a given value of $\overline{n}_e(0) < \overline{n}_{e_{crit}}(0, \overline{J})$, the cathode is emission limited. If $\overline{n}_e(0)$ is held fixed and the current magnitude is increased (made more negative), the system remains emission limited and the (negative) potential fall increases rapidly.

When $\overline{n}_e(0) > \overline{n}_{e_{crit}}(0, \overline{J})$, the cathode is space-charge limited. As the current is increased, the electron sheath thins, the potential fall slowly increases, and the potential minimum becomes shallower and moves back toward the cathode surface. Eventually a value of $\overline{J}$ is reached where the cathode becomes emission limited, and the potential fall increases much more rapidly.

This behavior is summarized in Fig. 2.9, where the cathode potential fall is plotted versus $\overline{n}_e(0)$ with $\overline{J}$ as a parameter. The contour separating the space-charge-limited and emission-limited operation, where $\overline{E}(0) = 0$ is shown as a dashed line.

C.2.5 Non-Emitting Anode

Starting with a floating, non-emitting electrode, we let the plasma draw a net current from the anode, or conversely, the electrode is biased more positive relative to the floating potential. As the current is increased, the flux of collected electrons rapidly increases, while the flux of collected ions slowly decreases; the ion sheath becomes thinner and weaker with increasing current; and the negative anode fall decreases in magnitude.

The electron flux increase is large compared with the ion flux decrease, and most of the current is carried by electrons which are drawn from the plasma. This contrasts with the behavior of the cathode, where the ions were the dominant charge carrier because the electron flux decreased with increasing current, leaving only the ions to carry the current.

As $\overline{J}$ approaches $\overline{J}_I \equiv (1 + \mu)/(1 - \mu)$, the ion sheath almost completely dissapears, an electron sheath forms at the anode surface, and the

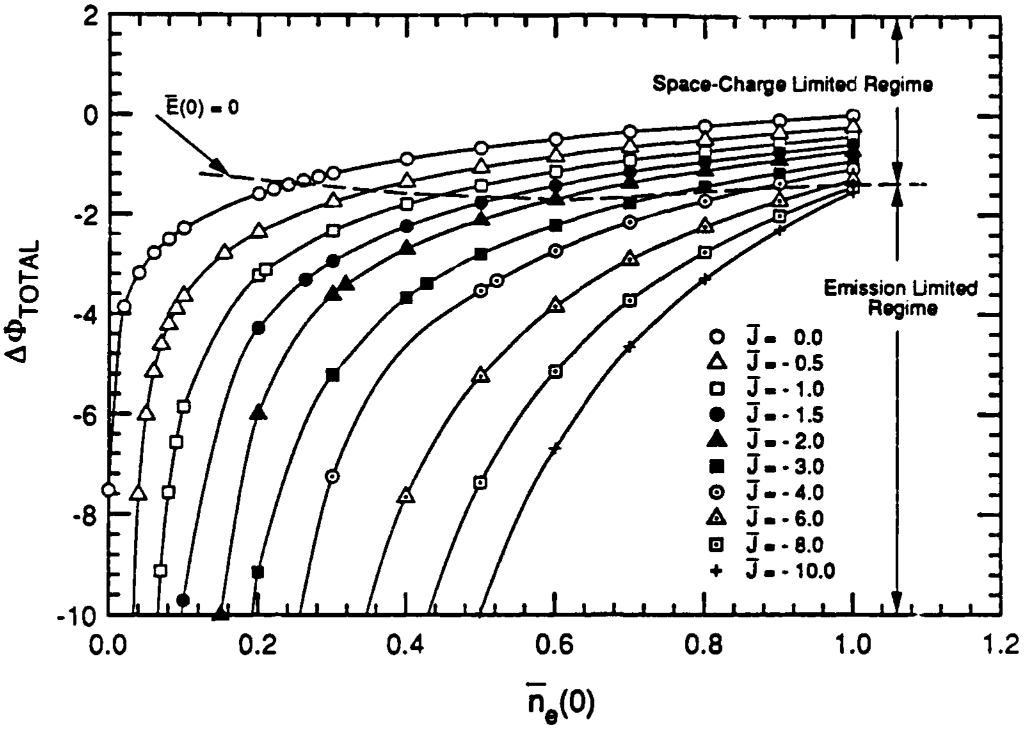

Fig. 2.9. Cathode potential fall $\Delta\overline{\Phi}_{total}$ versus $\overline{n}_e(0)$ with current $\overline{J}$ as a parameter, showing the distinction between the space-charge-limited and emission-limited regimes.

electric field at the anode surface changes sign from negative to positive. This is shown in Fig. 2.10.

While a floating electrode ($\overline{J} = 0$) differentiates anodes from cathodes, one can argue that the current $\overline{J} = \overline{J}_I$ for field inversion is the natural division determining the plasma-electrode behavior. This asymmetry is strictly a result of the unequal electron and ion mobilities. As was stated earlier, in the limit $\mu \rightarrow 1$, $\overline{J}_I \rightarrow 0$, and hence the field inversion and floating electrode conditions merge.

For $\overline{J} > \overline{J}_I$ the anode electron sheath becomes thicker and stronger and the positive potential fall increases. Figure 2.11 shows that near saturation (for $\overline{J} \approx \overline{J}_A \equiv 2/(1+\mu)$), the anode boundary layer is composed of an electron sheath adjacent to the electrode which merges into the ionization nonequilibrium region, followed by the uniform plasma. As before, the presence of the sheath does not alter the value of the

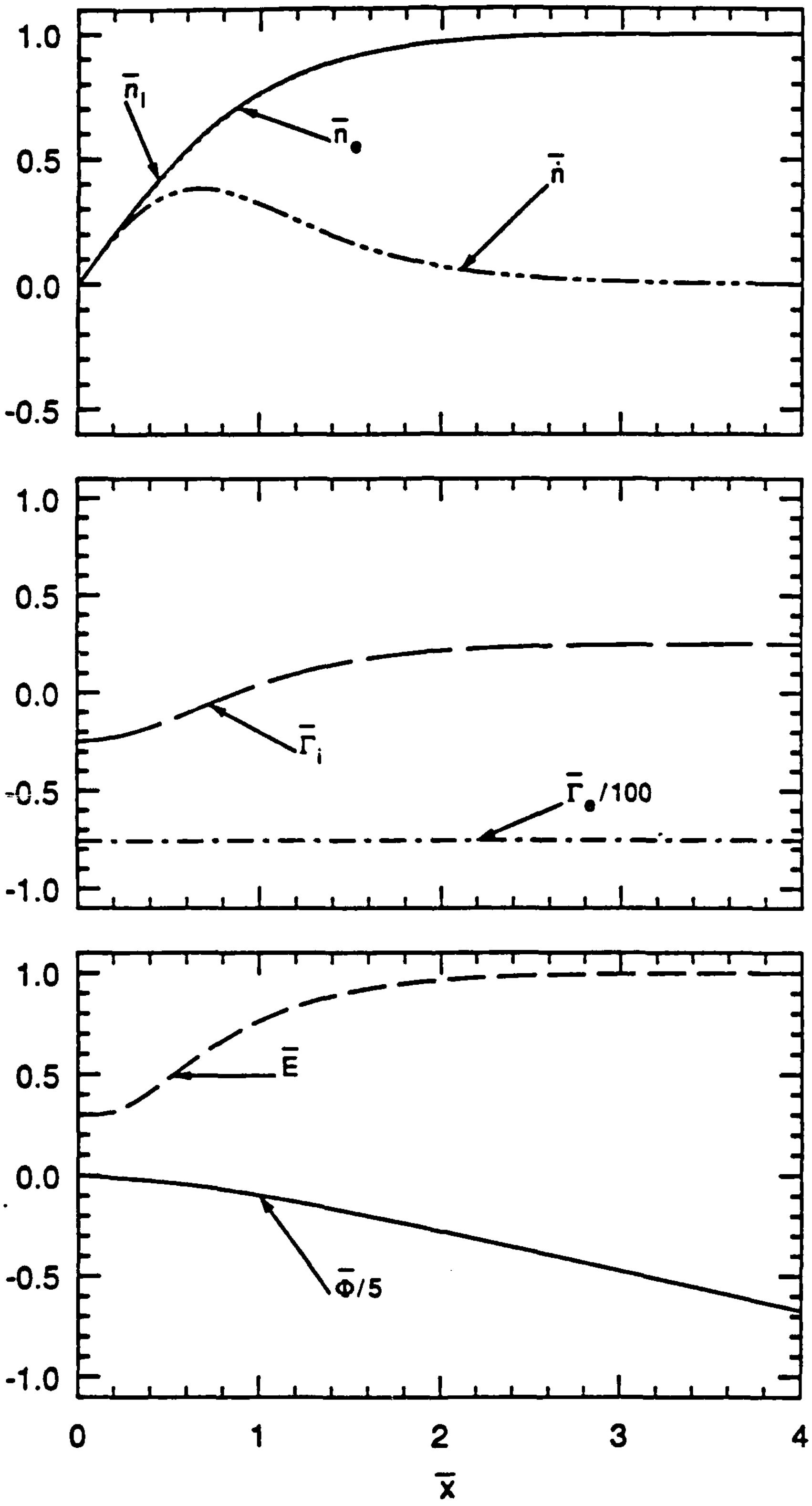

Fig. 2.10. Profiles of the dependent variables for a non-emitting anode near the potential fall inversion. Parameter values $\epsilon = 10^{-1}$, $\bar{J} = -2\mu$, $\bar{n}_e(0) = \bar{n}_i(0) = 0$.

saturation current found from the quasi-neutral solution.

Comparing Figs. 2.8 and 2.11, at saturation the anode sheath is clearly much thinner than the cathode sheath, and the net generation region is very nearly identical in size and position to that of the quasi-neutral solution. As the current is increased for a non-emitting anode, the charged particle profiles remain similar to their quasi-neutral values. The opposite is true for cathodes; as the current increases to a cathode, the charged particle concentration profiles deviate strongly from those of the quasi-neutral solution.

C.2.6 Ion-Emitting Anode

The possibility of ion emission from an anode is relevant to the cases of the emitter of a thermionic converter, and the anode of a noble gas MHD generator, seeded with an alkali metal and having hot electrodes made of a refractory metal. Basically, ion emission is significant only when the work function of the electrode is higher than the ionization of the seed, and significant surface ionization can occur. Moreover, ion emission from an anode only makes a significant difference for $\overline{J} > \overline{J}_I$, when there is an electron sheath and the ion emission (partially) neutralizes it, reducing the positive potential fall and allowing more electron current to be drawn from the plasma.

The effect is analogous to the effect of electron emission from a cathode which partially neutralizes the ion sheath, reducing the potential fall and allowing more current to flow.

To summarize, Poisson's equation has removed the singularity for the electric field and potential at the electrode surface which was found with the quasi-neutral solution. As a result, we have been able to calculate the current-voltage characteristics for both cathodes and anodes with and without charged particle emission by the electrode. We have also found that for non-emitting electrodes, the sheath does not alter the saturation behavior predicted by the quasi-neutral solution, so long as the electrons remain at the same temperature as the background neutral particles.

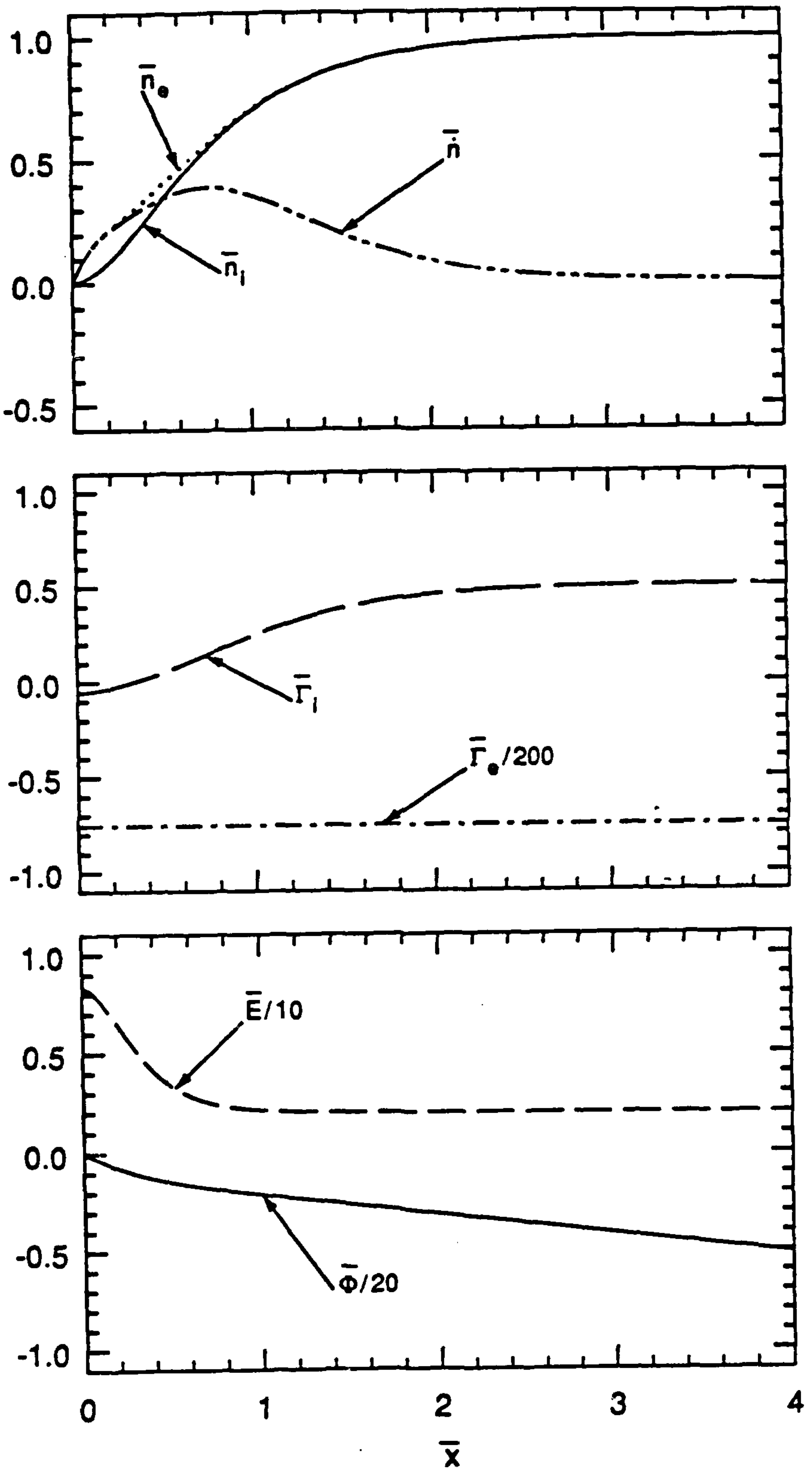

Fig. 2.11. Profiles of the dependent variables for a non-emitting anode close to saturation. Parameter values $\epsilon = 10^{-1}$, $\bar{J} = 2$, $\bar{n}_e(0) = \bar{n}_i(0) = 0$.

C.3 Non-Isothermal Solution, Simplified Energy Equation (Numerical)

Results from the quasi-neutral and isothermal models show that the ionization and recombination reactions play an important role in the current saturation behavior.

A necessary condition for true current saturation is that the total net generation rate in the boundary layer must be independent of current. This condition is satisfied for the quasi-neutral solution and for non-emitting electrodes with the isothermal model, primarily because we have assumed that the electron temperature remains constant. However, for many plasma conditions, Joule dissipation ($\overline{J} \cdot \overline{E}$) may heat (or cool) the electrons, whence the electron temperature profile becomes a function of the current density. The ionization and recombination reaction rates vary with the electron temperature such that heating the electrons also increases the total net generation rate. The end result is that by increasing the electron temperature and total net generation rate, Joule heating can change the value of the saturation currents, or may remove the saturation phenomenon entirely.

To investigate this effect, the electron energy equation is added to the model so that the electron temperature may differ from the ion and neutral particle temperatures, which we still assume to be equal. For the moment, we consider a simplified form of the electron energy equation given by

$$\overline{\Gamma}_e \overline{E} = -3\Theta \overline{n}_e (\overline{T}_e - \overline{T}), \qquad (2.41)$$

which balances the rate of energy exchange between the electrons and the electric field (Joule heating/cooling), and the rate of collisional energy exchange between the electrons and the background neutral particles. The free parameter Θ is a measure of the collisional coupling between the electrons and the background neutral particles. For $\Theta \to \infty$, the electrons become perfectly coupled to the neutral particles, the electron temperature and neutral temperature become equal, and the solutions go over to the isothermal solution of the previous section.

An equivalent expression for eq. (2.41) has been used in previous analyses [2.10,11] and we include it in eq. (2.41) to form a basis for comparison with the solutions for the full electron energy equation.

Neglected here, are the electron energy equation terms which account for thermal conduction, energy loss by the electrons due to the net generation rate of electron-ion pairs, and energy convected by the electron flux. These terms will be considered in the next section.

The electron temperature is now a dependent variable of the problem, hence the temperature-dependent forms of the mass and momentum conservation equations, eqs. (2.1*and*2.2), are solved with Poisson's equation, eq. (2.3), and the electron energy equation, eq. (2.41). In review:

Mass Conservation

$$\frac{d\overline{\Gamma}_i}{d\overline{x}} = \overline{\dot{n}} = \overline{n}_e \overline{T}_e^{-9/2} \left\{ \overline{T}_e^{3/2} \exp\left[\overline{\epsilon}_i \left(1 - \frac{1}{\overline{T}_e} \right) \right] - \overline{n}_e \overline{n}_i \right\} \tag{2.1a}$$

$$\frac{d\overline{\Gamma}_e}{d\overline{x}} = \overline{\dot{n}} \tag{2.1b}$$

Momentum Conservation

$$\frac{d\overline{n}_i}{d\overline{x}} = -\frac{\overline{n}_i}{\overline{T}} \left(\frac{d\overline{T}}{d\overline{x}} - \overline{E} \right) - \frac{4}{1+\mu} \frac{\overline{\Gamma}_i}{\overline{T}} \tag{2.2a}$$

$$\frac{d\overline{n}_e}{d\overline{x}} = -\frac{\overline{n}_e}{\overline{T}_e} \left(\frac{d\overline{T}_e}{d\overline{x}} + \overline{E} \right) - \frac{4\mu}{1+\mu} \frac{\overline{\Gamma}_e}{\overline{T}_e} \tag{2.2b}$$

Poisson's Equation

$$\frac{d\overline{E}}{d\overline{x}} = \frac{1}{\epsilon^2} \left(\overline{n}_i - \overline{n}_e \right) \tag{2.3}$$

Using an algebraic form for the electron energy equation does not change the order of the system of equations from that of the isothermal problem. Hence, five boundary conditions are required; $\overline{\Gamma}_{e\infty}$, $\overline{\Gamma}_{i\infty}$, and $\overline{E}_\infty$ in the far-field and $\overline{n}_{e,i}(0)$ at the electrode surface. However, solving eq. (2.41) for the electron temperature,

$$\overline{T}_e = \overline{T} - \frac{\overline{\Gamma}_e \overline{E}}{3\Theta \overline{n}_e} \tag{2.42}$$

shows that $\overline{T}_e$ has a singularity for $\overline{n}_e \rightarrow 0$. This is, in part, due to the fact that Joule dissipation and electron collisions with neutral particles are no longer the dominant electron energy exchange mechanisms when $\overline{n}_e \rightarrow 0$. Also, $\overline{n}_e = 0$ is only a reasonable assumption for distances on the order of one mean free path from the surface of a perfectly absorbing electrode. In this region, the velocity distribution for the electrons becomes completely one-sided and the translational electron temperature becomes undefined.

To avoid this difficulty, we examine solutions for $0 \neq \overline{n}_e(0) \ll 1$ (i.e., for very low levels of electron emission) and submit that the solutions convey the same practical results as one would find for a *perfectly* absorbing electrode ($\overline{n}_e(0) = 0$). The results have been divided into two groups; those for weak electron emission by the electrode and those for strong emission by the electrode.

An electrode is termed weakly-emitting when the the electric field at the surface is negative for $\overline{J} = 0$, and the emitted electrons are accelerated into the plasma (the electrode is emission limited). Strongly-emitting electrodes are space-charge limited for $\overline{J} = 0$, i.e., the electric field at the surface is positive and most of the emitted electrons are returned to the electrode.

As with the isothermal results, for the purpose of discussion it is convenient to use a moderate value of ϵ, e.g. $\epsilon \equiv \lambda_D/\ell_R = 10^{-1}$, so that the structure of the sheath and the ionization non- equilibrium region can both be resolved on a linear scale. All solutions are for the typical value of $\mu = 1/300$, but as before, the solutions are quite insensitive to μ when $\mu \ll 1$. A value of $\overline{\epsilon}_i = 16.7$ has been chosen, which is consistent with a potassium-seeded plasma at 3000 K.

In addition, we consider only anodes ($\overline{J} > 0$) in the results presented here.

C.3.1 Weakly-Emitting Anode

Current-voltage characteristics are plotted in Fig. 2.12 for an anode with $\overline{n}_e(0) = 0.02$ and $\overline{n}_i(0) = 0$.

The solid lines are solutions for $5 \times 10^3 \leq \Theta \leq 5 \times 10^4$ and the dotted line is the solution to the isothermal model (neglecting Joule dissipation). From this figure, we see that as $\Theta \rightarrow \infty$, the isothermal result is reproduced as expected. However, for smaller values of Θ (less collisional coupling), Joule heating produces a *significant* electron

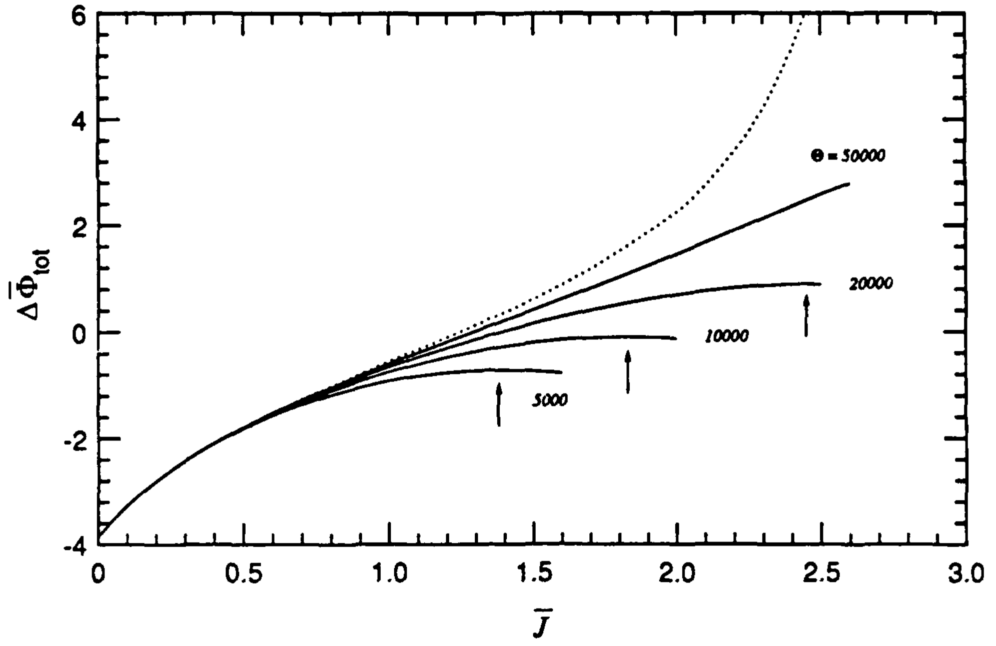

Fig. 2.12. Current-voltage characteristics for a weakly-emitting anode ($\overline{n}_e(0) = 0.02$, $\overline{n}_i(0) = 0$) with $\epsilon = 10^{-1}$, $\overline{\epsilon}_i = 16.7$ and $\mu = 1/300$. The solid lines are solutions for $5 \times 10^3 < \Theta < 5 \times 10^4$ and the dotted line is a solution for the isothermal model ($\Theta \rightarrow \infty$). Vertical arrows indicate the point where the incremental resistance of the plasma-electrode boundary layer equals zero, i.e., $d\Delta\overline{\Phi}_{total}/d\overline{J} = 0$.

temperature elevation at large currents. The resulting increase in the net generation rate of electron-ion pairs decreases the incremental resistance of the boundary layer as the current increases, where we define

$$\frac{d\Delta\overline{\Phi}_{total}}{d\overline{J}} = \text{Incremental Resistance of the Boundary Layer} \qquad (2.43)$$

Eventually, the incremental resistance becomes negative and the potential drop decreases with increasing current. We interpret this to be the initial stage in the transition from a diffuse to a constricted mode of current transfer. For each curve, a vertical arrow indicates the point where the incremental resistance of the plasma-electrode boundary layer equals zero, i.e., $d\Delta\bar{\Phi}_{total}/d\bar{J} = 0$.

In Fig. 2.13, the total net generation rate is plotted vs $\bar{J}$ for the same solutions shown in Fig. 2.12. The solid lines are solutions for $5 \times 10^3 < \Theta < 5 \times 10^4$ and the dotted line is the solution for the isothermal model ($\Theta \rightarrow \infty$).

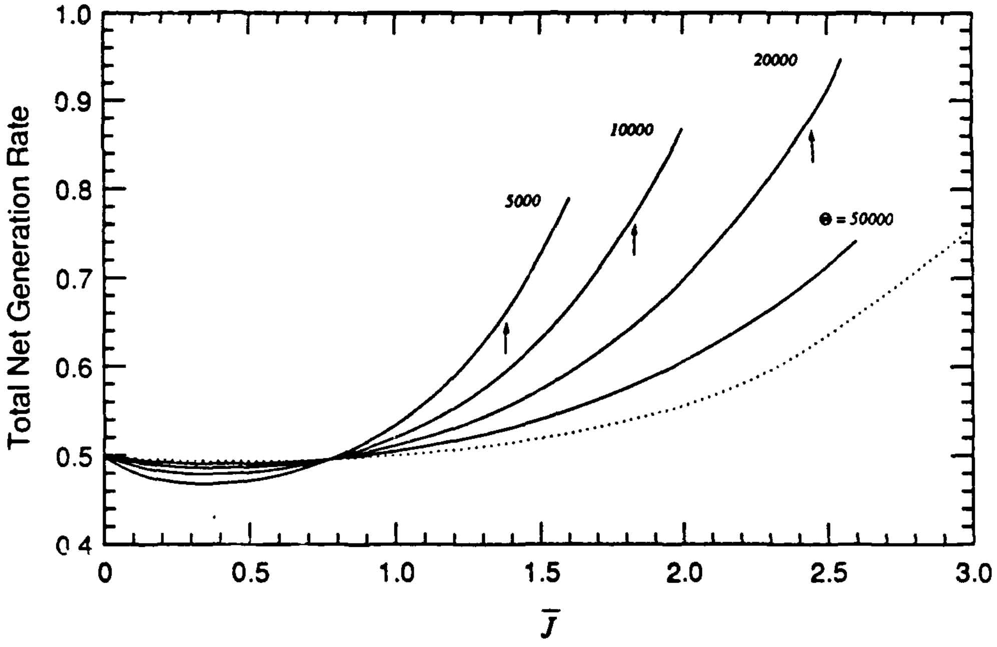

Fig. 2.13. Total net generation rate vs $\bar{J}$ for a weakly-emitting anode ($\bar{n}_e(0) = 0.02$, $\bar{n}_i(0) = 0$) with $\epsilon = 10^{-1}$, $\bar{\epsilon}_i = 16.7$ and $\mu = 1/300$. The solid lines are solutions for $5 \times 10^3 < \Theta < 5 \times 10^4$ and the dotted line is a solution for the isothermal model ($\Theta \rightarrow \infty$).

For a weakly-emitting, floating electrode ($\bar{n}_i(0) = \bar{n}_e(0) = 0, \bar{J} = 0$), an ion sheath forms and the electron temperature in the sheath is decreased below the background neutral temperature as shown in Figs. (2.14) and (2.15). When the electrode is emission limited ($0 \leq \bar{J} \leq 0.8$, in this case), the electrons move against the field which decelerates and cools them. This also decreases the total net generation rate to a value below that of the isothermal solution. The ion sheath decreases in strength as the current approaches $\bar{J} = 0.8$ from below. For $\bar{J} = 0.8$ the ion sheath essentially disappears (see Fig. 2.16). When $\bar{J} > 0.8$ an electron sheath forms adjacent to the anode surface as shown in Fig. 2.17. The electron sheath creates a positive electric field near the anode surface and the electron temperature is raised above the neutral background temperature. The temperature elevation also increases the total net generation rate in the layer, hence for $\overline{J} > 0.8$ here, the total net generation rate is larger than the value of 1/2 found with the quasi-neutral solution.

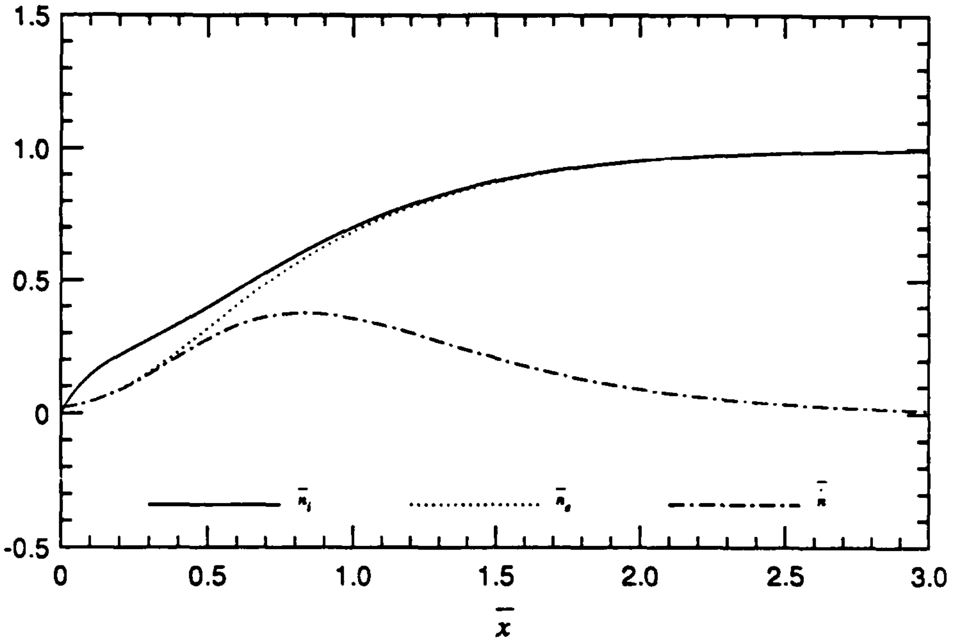

Fig. 2.14. Ion and electron number density and net generation rate spatial profiles for $\bar{n}_e(0) = 0.02$, $\bar{n}_i(0) = 0$, $\epsilon = 10^{-1}$, $\bar{\epsilon}_i = 16.7$, $\mu = 1/300$, $\Theta = 2 \times 10^4$ and $\overline{J} = 0$.

C.3.2 Strongly-Emitting Anode

Strong electron emission by the anode ($\bar{n}_e(0) > 0, \overline{E}(\bar{x} = 0, \overline{J} = 0) > 0$) substantially modifies the low current sheath structure discussed above. The emitted electrons neutralize the ion sheath which would normally be present in the absence of emission. An electron sheath forms adjacent to the anode surface, and a positive electric field is set up which accelerates the electrons drawn from the plasma, heating them. The heated electrons raise the total net generation rate above the value calculated with the isothermal model.

The total net generation rate increases with increasing current and the boundary layer incremental resistance decreases with increasing current. Current-voltage characteristics are shown in Fig. 2.18 for

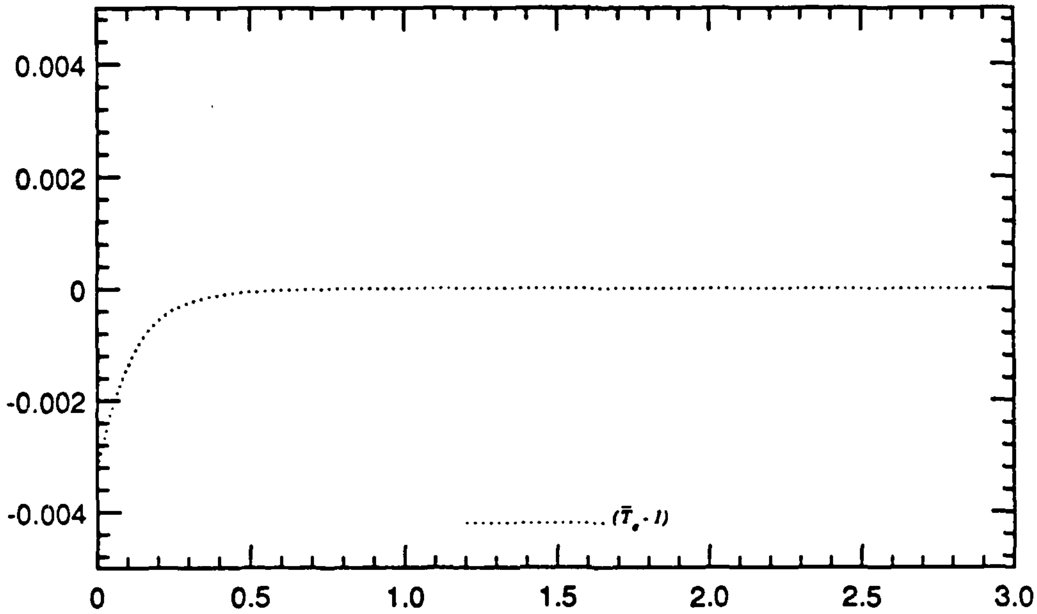

Fig. 2.15. Electron temperature spatial profile for $\bar{n}_e(0) = 0.02$, $\bar{n}_i(0) = 0$, $\epsilon = 10^{-1}$, $\bar{\epsilon}_i = 16.7$, $\mu = 1/300$, $\Theta = 2 \times 10^4$ and $\bar{J} = 0$.

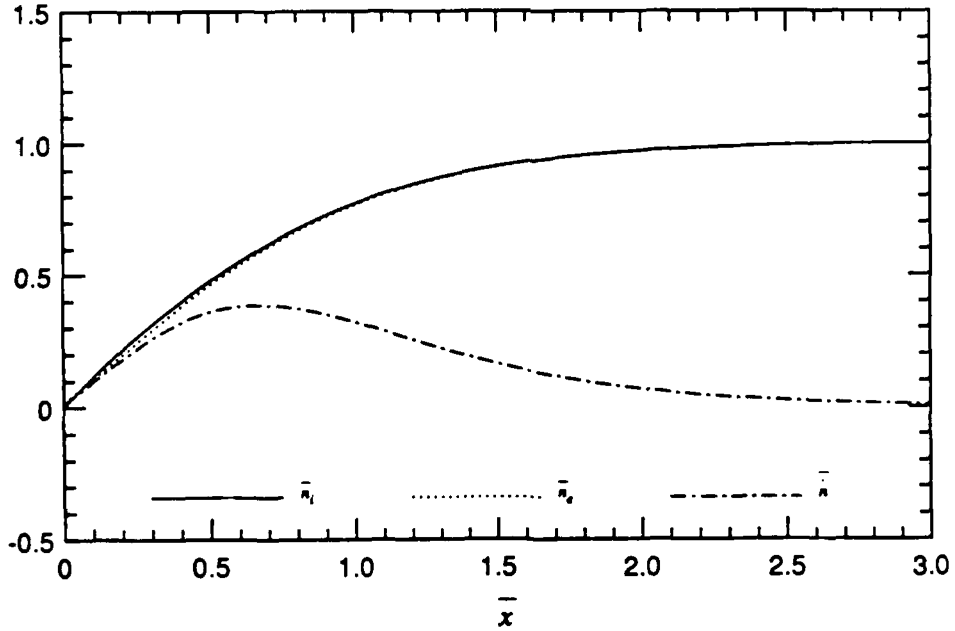

Fig. 2.16. Ion and electron number density and net generation rate spatial profiles for $\bar{n}_e(0) = 0.02$, $\bar{n}_i(0) = 0$, $\epsilon = 10^{-1}$, $\bar{\epsilon}_i = 16.7$, $\mu = 1/300$, $\Theta = 2 \times 10^4$ and $\bar{J} = 0.8$.

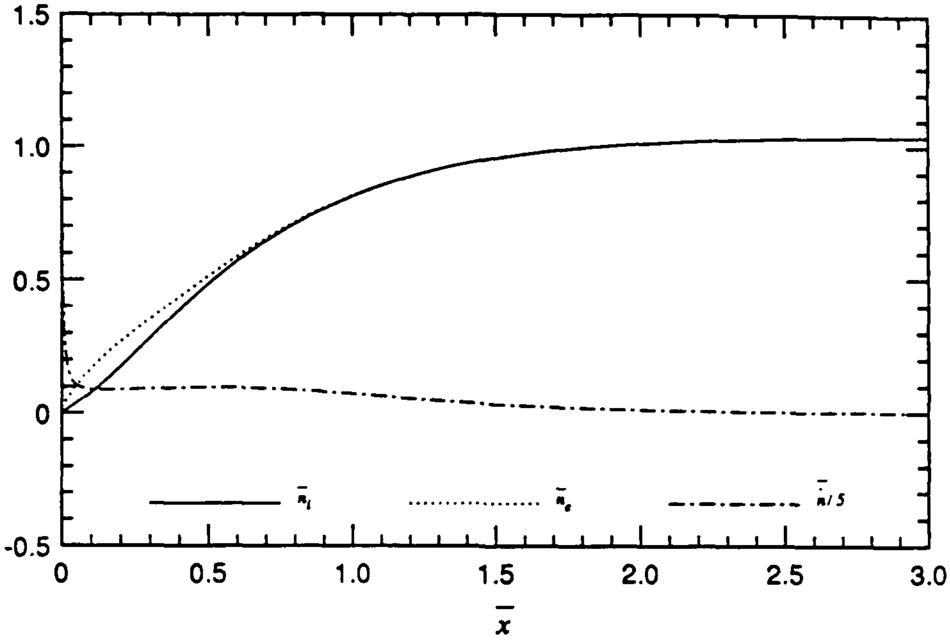

Fig. 2.17. Ion and electron number density and net generation rate spatial profiles for $\overline{n}_e(0) = 0.02$, $\overline{n}_i(0) = 0$, $\epsilon = 10^{-1}$, $\overline{\epsilon}_i = 16.7$, $\mu = 1/300$, $\Theta = 2 \times 10^4$ and $\overline{J} = 2.0$.

an anode with $\overline{n}_e(0) = 0.4$. Comparing Figs. (2.13) and (2.18), it is observed that for a given value of the collision parameter Θ, increasing the electron emission from an anode decreases the current at which the transition from a diffuse to constricted discharge will begin.

These results demonstrate that Joule dissipation significantly enriches the possible solutions for the plasma-electrode boundary layer. As with the simpler models, it is clear that the total net generation is the key variable to consider, as it has a direct bearing on the current-voltage characteristics. In the next section, we investigate the importance of the remaining (heretofore neglected) electron energy equation terms.

C.4 Non-Isothermal Solution, Complete Set of Equations (Numerical)

In this part, we replace the simplified electron energy equation of the previous section with a more complete form of the electron energy equation which includes additional terms for electron thermal conduction, electron energy loss due to the net generation rate of electron-ion pairs, and energy convected by the electron flux. The

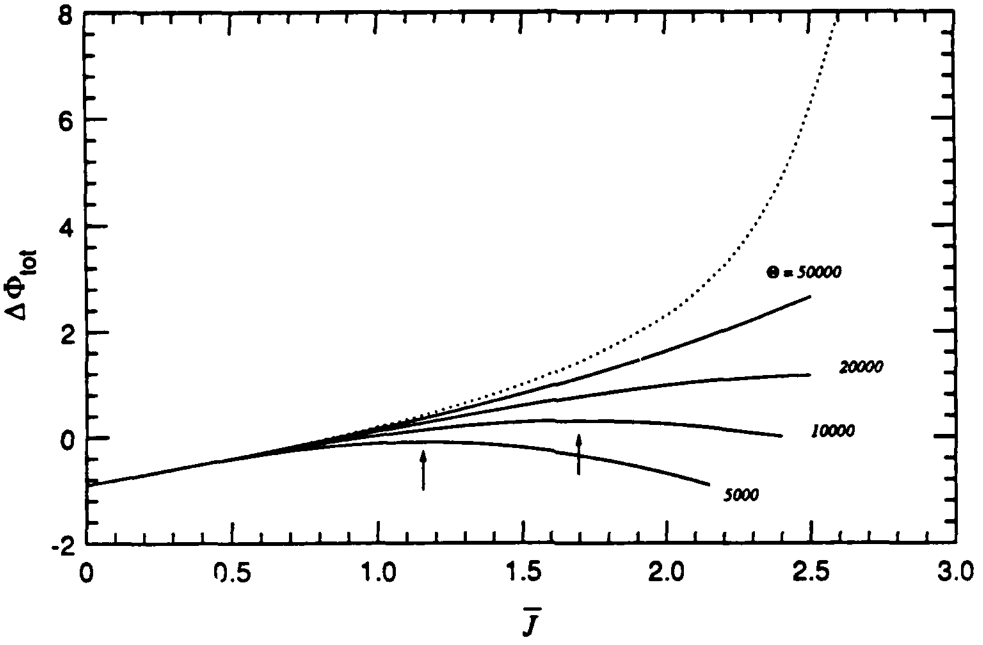

Fig. 2.18. Current-voltage characteristics for a strongly-emitting anode ($\bar{n}_e(0) = 0.4, \bar{n}_i(0) = 0$) with $\epsilon = 10^{-1}$, $\bar{\epsilon}_i = 16.7$ and $\mu = 1/300$. The solid lines are solutions for $5 \times 10^3 < \Theta < 5 \times 10^4$ and the dotted line is a solution for the isothermal model ($\Theta \rightarrow \infty$).

energy equation is written:

$$-\frac{6}{5}\frac{d}{d\bar{x}}\left(\bar{n}_e\bar{T}_e\frac{d\bar{T}_e}{d\bar{x}}\right) + \frac{5\mu}{1+\mu}\frac{d}{d\bar{x}}(\bar{\Gamma}_e\bar{T}_e) + \frac{2\mu}{1+\mu}\bar{\Gamma}_e\bar{E} = -\frac{6\mu}{1+\mu}\Theta\bar{n}_e(\bar{T}_e - \bar{T}) - \bar{\epsilon}_i\frac{2\mu}{1+\mu}\bar{n}\,. \qquad (2.4)$$

This second-order, nonlinear ordinary differential equation replaces the algebraic energy equation of the previous section, so two additional boundary conditions are required. We use eq. (2.42) to find the electron temperature in the far-field as one boundary condition. The second boundary condition is taken at the electrode surface, where we assume that for an electrode with strong electron emission, $\bar{T}_e(0) \rightarrow \bar{T}_{electrode}$, and for weak electron emission $d\bar{T}_e/d\bar{x}|_0 \propto \bar{E}(0)$. The latter condition is based on a nonequilibrium, kinetic analysis by Chung [2.12] of the near electrode region. This form of the energy equation also has a singularity for $\bar{T}_e$ when $\bar{n}_e \rightarrow 0$, so we approximate the solution for a non-emitting electrode with a small but non-zero value for $\bar{n}_e(0)$.

Figure 2.19 shows the calculated current-voltage characteristics for an anode with strong electron emission, and compares solutions for the simple and complete forms of the electron energy equation. Very little difference is observed. A slightly larger potential drop is calculated for the full solution for currents near the transition to a constricted mode discharge. Equivalently, the solution for the simple form of the energy equation tends to slightly underpredict the current at which constriction begins.

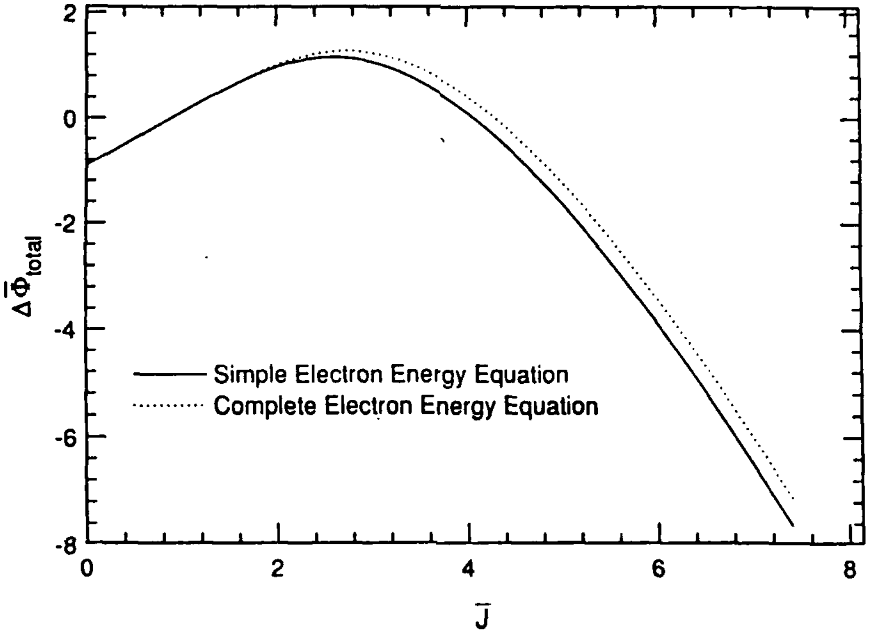

Fig. 2.19. Comparison of the current-voltage characteristics for the simple electron energy equation (solid line) and the full electron energy equation (broken line) for a strongly-emitting anode.

To understand why the current-voltage characteristics differ, one must examine the magnitude of each of the terms in the electron energy equation. As shown in Fig. 2.20, when the current is large the collisional loss and Joule dissipation are in balance far from the electrode. Near the electrode surface, the electrons gain energy by Joule heating and convection, and lose energy by conduction. Note that in this figure, the positive sense represents an energy loss by the electrons. Joule dissipation adds energy to the electrons, hence it is negative.

The additional energy loss by thermal conduction, not included in the simple model, tends to decrease the electron temperature in the sheath. For a given current and electron emission capability, the net generation rate is slightly less for the full solution than for the simple energy equation solution. This is why, as the transition to a constricted discharge begins, the total potential drop for the full solution falls off more slowly than the total potential drop found with the simple energy equation.

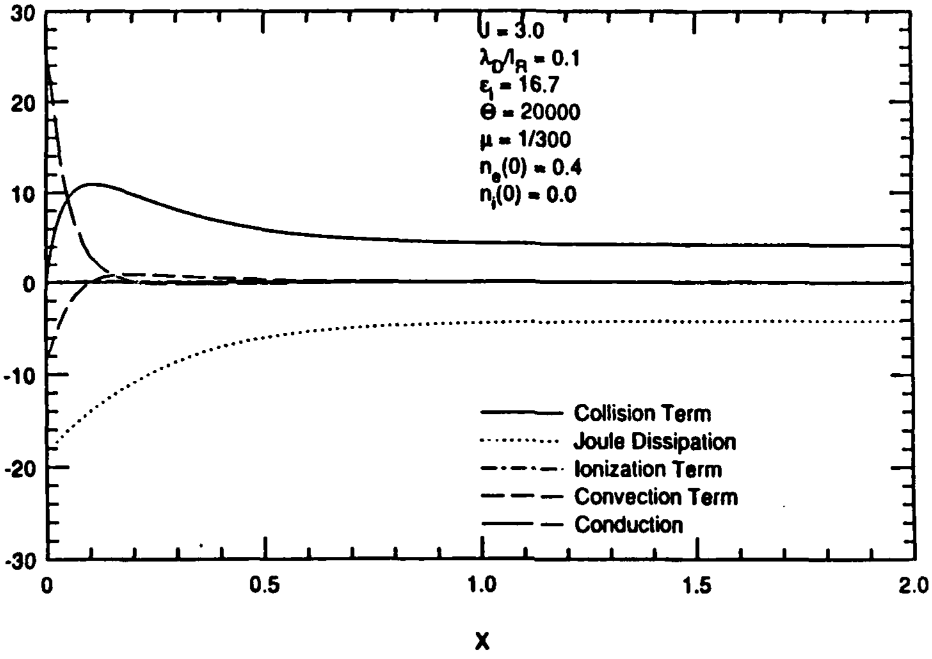

Fig. 2.20. Magnitude of the electron energy equation terms for a strongly-emitting anode at high current.

The mechanisms for energy exchange are quite different for small currents, as shown in Fig. 2.21, for a floating electrode with strong electron emission. Here, the *ionization* and *collision* terms are dominant over most of the boundary layer, except in the sheath. In the sheath, the energy transfer by collisions is replaced by thermal conduction, as was the case for large currents. Also note that, in this case, the electrons move against the field and are cooled ($\overline{J} \cdot \overline{E} < 0$), so that the total net generation rate is actually decreased below the quasi-neutral value.

To summarize, there is no significant difference between the isothermal and non-isothermal results for an anode at low current, but for large currents the increased net generation rate due to Joule heating removes the current saturation behavior found with the isothermal model. The non-isothermal results show that the net generation rate monotonically increases with increasing current. This reduces the incremental resistance of the plasma-electrode boundary layer and leads to the transition from a diffuse to a constricted mode of current transfer.

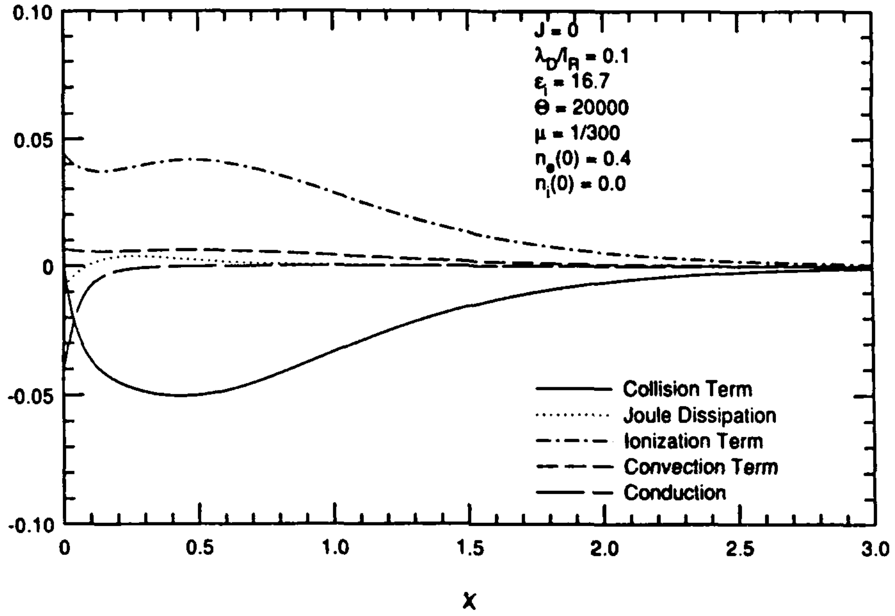

Fig. 2.21. Magnitude of the electron energy equation terms for a strongly-emitting floating electrode.

2.3 Interaction of Plasma Currents and Fluid Mechanics: MHD Secondary Flow

2.3.1 Introduction

In several space power and propulsion systems of potential interest to the Air Force, such as MPD thrusters, MHD generators, and rail guns, the interaction of current-induced forces and energy transfer with the plasma flow can be critical to both the understanding and performance of the system. The channel flow of a plasma through a transverse magnetic field is influenced by the Hall effect, which causes nonuniform Lorentz forces to arise in the direction mutually perpendicular to the channel axis and the magnetic field. The forces cause secondary flows to develop as the flow progresses down the region of electromagnetic-fluid interaction. The theoretical treatment of this problem has included the work of Fay [3.1], Broer et al. [3.2], Sato [3.3], Tani [3.4], Apollonskii and Kos'kin [3.5], Sastry and Bhadram [3.6], Liu et al. [3.7], and Ishikawa and Umoto [3.8]; in particular, for conditions which would be typical of a large-scale MHD power generator these secondary flows were predicted to be of substantial magnitude in the calculations reported by Maxwell et al. [3.9], Bityurin et al. [3.10], and Doss and Ahluwalia [3.11]. The calculated magnitude of these flows for a large-scale device ranges from 10 to 30% of the bulk velocity, depending on conditions, and the predicted consequences include the development of significant asymmetries in the profiles of mean axial velocity and of temperature, with resultant effects on wall heat transfer and electrode voltage drops. In addition, Demetriades et al. [3.12] predicted that these secondary flows could lead to magneto-aerothermal instabilities, which could include boundary layer separation and/or electric field breakdown near the electrodes.

Indirect evidence for the existence of MHD-induced secondary flow, reviewed by Girshick and Kruger [3.13], included measurements of temperature profiles obtained by James and Kruger [3.14] and of electrode voltage drops obtained by Barton [3.15], which indicated that MHD effects caused the anode (top) wall boundary layer of the channel to be colder than expected while the cathode (bottom) wall was hotter than expected. It was hypothesized that these results could be ascribed to a secondary flow mechanism. Demetriades et al. [3.12] conjectured that evident arc damage to the center of the anode wall in the downstream half of the channel used in the High Performance Demonstration Experiment at the Arnold Engineering Development Center [3.16] was a manifestation of the magneto-aerothermal instability mentioned above. McClaine et al. [3.17] reported axial velocity profiles measured using a traversing stagnation pressure probe mounted in the diffuser of the Avco Mk VI generator. The profile measured between the top and bottom walls was found to be strongly skewed by MHD forces, presumably as a consequence of secondary flow.

The work reported here consisted of experiments which included the first direct, quantitative measurements of the secondary flow field in an MHD channel. Additionally, the effect of secondary flow on the plasma momentum, thermal and electrical behavior was studied by making measurements of the profiles of mean axial velocity, turbulence intensity (axial and transverse) and plasma voltage, and by measuring electrode surface temperatures.

These experiments were performed under conditions which were not ideal, in that the flow in a combustion-driven MHD channel is inherently less "clean" than in a carefully arranged laboratory flow involving low-temperature air or water. Factors such as combustion nonuniformities, cooled walls, and irregularities in the electrode-insulator wall structure inevitably affect the flow. Nevertheless, the present experiments were designed to minimize extraneous effects to the extent possible. Also, the channel was run under non-slagging conditions, and the measurements were made under different orientations of the magnetic field, and with the magnet turned off, in order to isolate the effects on the flow field of Lorentz forces as opposed to non-ideal conditions.

2.3.2 Research Objectives

The goal of the work in this area was to obtain experimental information which would help describe the three-dimensional flow field in an MHD device. Specifically, the major objectives which guided this work were the following:

1. To study the effect of electromagnetic body forces on the secondary flow field including investigation of the magnitudes of these secondary flows and how the vortex structure is affected by applied magnetic fields and discharges.

2. To study the effect of MHD interaction on mean axial velocity profiles.

3. To study the effect of MHD interaction on turbulence.

2.3.3 Status of Research

A. Theoretical Background

A schematic representation of an MHD channel is pictured in Fig. 3.1. The channel is a rectilinear duct whose axis points in the x-direction. An external magnet supplies a uniform magnetic induction B, pointing in the z-direction. The magnetic Reynolds number is assumed small, thus the induced magnetic field is negligible in comparison to the applied field.

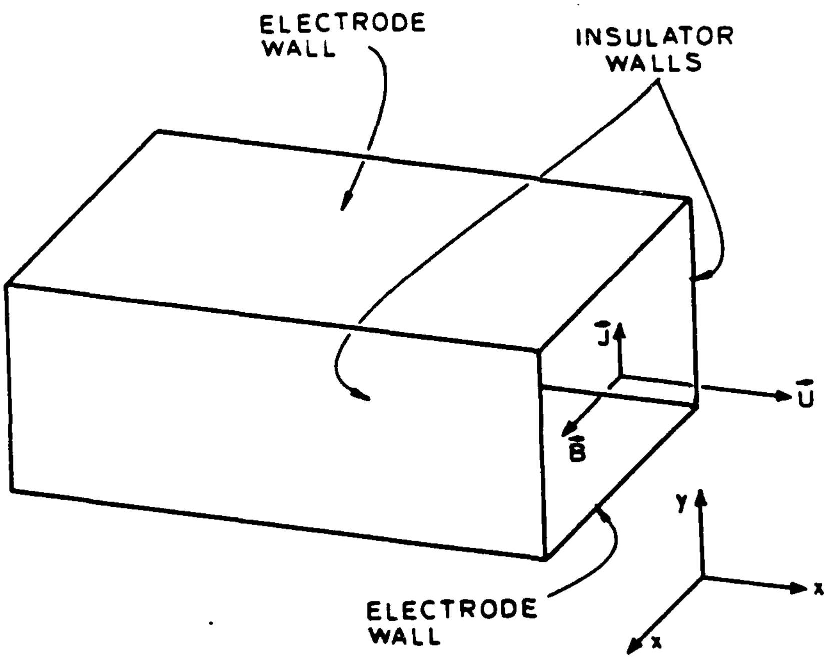

Fig. 3.1. Schematic representation of an MHD channel.

The motion of charged particles through the magnetic field establishes a u×B Faraday field (in the laboratory frame of the reference) which points in the y-direction. In an MHD generator this field is utilized by drawing current through electrodes placed in the top and bottom walls, these electrodes being connected through an external load. In addition to the Faraday current J_y, the Hall effect for a partially ionized gas causes the current density vector J to have a local component in the x-direction. This can be expressed by considering the conductivity as a tensor and writing Ohm's Law in the form (see, e.g., Mitchner and Kruger [3.18])

$$J = \overleftrightarrow{\sigma}E' \ , \tag{3.1}$$

where E' is the electric field in a frame of reference moving with the mean mass velocity of the fluid and, assuming ion slip to be negligible,

$$\overleftrightarrow{\sigma} = \frac{\sigma}{1 + \beta^2} \begin{vmatrix} 1 & -\beta & 0 \\ \beta & 1 & 0 \\ 0 & 0 & 1 \end{vmatrix} . \tag{3.2}$$

For simplicity, it is assumed that the Hall current J_x is everywhere non-negative, as pictured in Fig. 3.2. In a combustion MHD channel the walls must be cooled because of materials constraints, and consequently the plasma is much more conductive in the core than near the walls. Furthermore, the u×B interaction goes to zero at the walls because of the no-slip condition. Thus, to first order, the profile $J_x(z)$ would appear approximately as indicated in Fig. 3.2.

The fluid momentum equation under the stated conditions can be written

$$\rho \frac{Du}{Dt} = - \nabla p + \nabla \overleftrightarrow{\tau} + J \times B \ , \tag{3.3}$$

where ρ is the mass density, p the thermodynamic pressure and $\overleftrightarrow{\tau}$ the viscous stress tensor. With $B = B_z$, the presence of a non-zero Hall current causes the J×B Lorentz force to have a component in the y-direction. Taking the curl of (3.3) to obtain the fluid vorticity equation, the following result is obtained for the vorticity Ω:

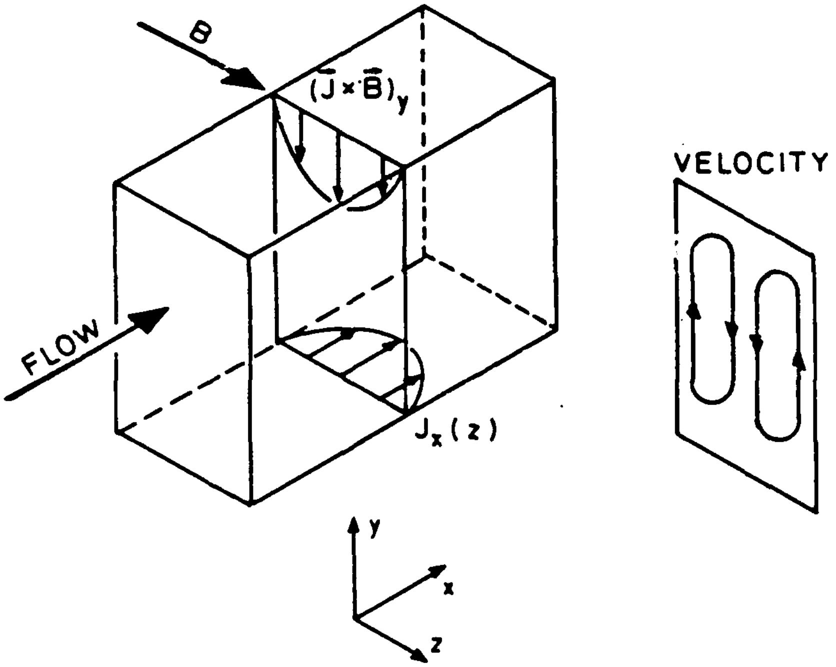

Fig. 3.2. Secondary flow mechanism for a case of positive net Hall current.

$$\rho \frac{D\Omega}{Dt} = \nabla(J\times B) + (\text{viscous terms}) + (\text{density-gradient terms}) \ . \qquad (3.4)$$

In a combustion-driven MHD channel, the flow is generally turbulent so that the viscous terms are dominated by Reynolds stresses. Moreover, the density is nonuniform because the walls are cooled. Neglecting these effects and assuming that B_z = constant, the following expression is obtained for the contribution of Lorentz forces to the axial vortices component:

$$p \frac{D\Omega_x}{Dt} = B \frac{\partial J_x}{\partial z} \ . \qquad (3.5)$$

It is thus evident that the nonuniformity of the Hall current density between the core and the side walls introduces a rotational component into the Lorentz force. For the first-order profile of J_x pictured, the two-cell flow structure shown on the right of Fig. 3.2 would be expected to arise. The presumed effect of such a secondary flow would be to transport hot, fast core plasma toward the bottom wall while sweeping relatively cold, slow, side-wall fluid into the boundary layer of the top wall.

As the axial vorticity and the distribution of J_x are coupled through (3.5), the actual structure of the secondary flow field could be considerably more complicated than the simple pattern suggested in Fig. 3.2; indeed, J_x might not increase monotonically from the walls to the core, in which case the axial vorticity could change sign in some regions of the cross-plane. It should also be pointed out that commercial Faraday MHD generators would suppress the flow of net Hall current by using segmented electrodes separated by insulators. However, the Hall effect would still cause the local value of J_x to be in general non-zero; only the integrated value of J_x over the cross-plane would vanish, and then only in the absence of axial leakage currents. A typical profile of J_x under these circumstances and of the resulting six-cell secondary flow field are shown in Fig. 3.3. For the conditions of envisioned commercial-scale MHD generators the strength of these secondary flows could be significant, in spite of the suppression of net Hall current; this case was discussed by Swean et al. [3.19] as well as by several of the authors cited earlier.

A.1 Description of Experiments

A.1.1 Flow Train and Run Conditions

MHD secondary flow was investigated in series of experiments conducted at the High Temperature Gasdynamics Laboratory at Stanford University. The M-2 flow train, shown in Fig. 3.4 was used. This consisted of a combustor with a nominal 2-MW thermal input rating, a large mixing plenum, a nozzle through which the combustion products were accelerated into a duct having a square cross-section measuring 5.1 cm on a side, a diffuser, and an exhaust system including a scrubber and a stack. The square duct consisted of a run-in section and the active channel itself, which was enclosed in a 2.6-T water-cooled, copper-coil magnet. Physical dimensions of the flow train are given in Table 3.1, including distances from the nozzle exit to the measurement locations.

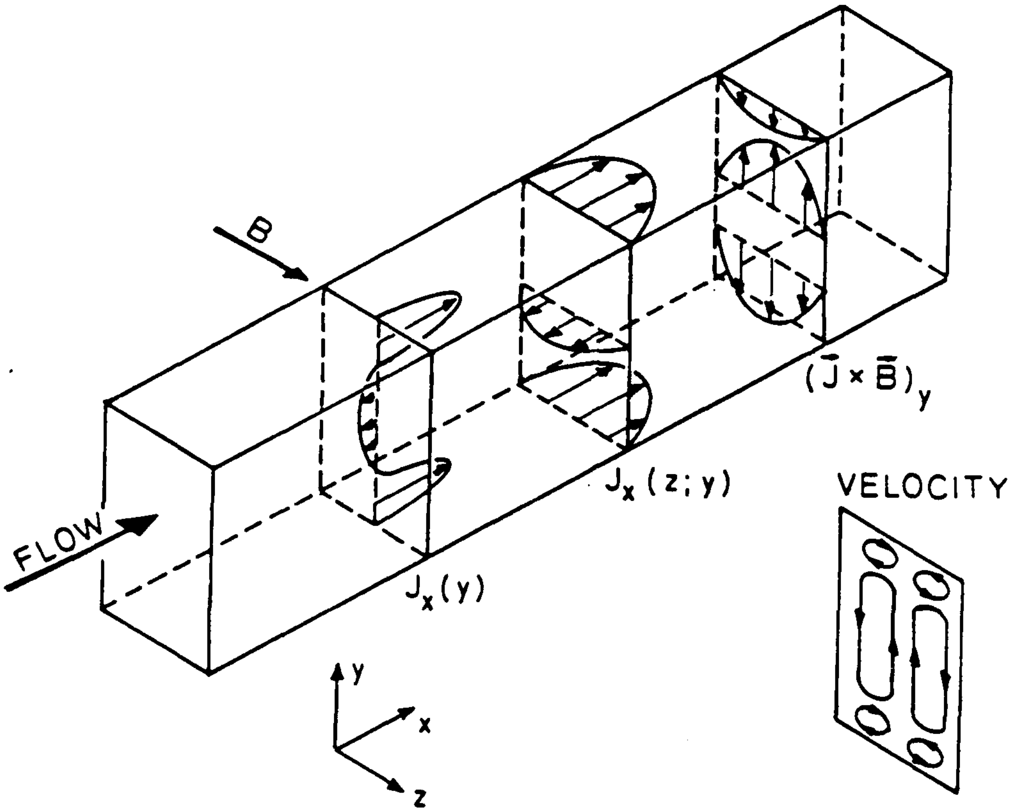
B
FLOW
$J_x(y)$
$J_x(z;y)$
$(\vec{J} \times \vec{B})_y$
VELOCITY
y
x
z

Fig. 3.3. Secondary flow mechanism for a segmented Faraday generator (zero net Hall current).

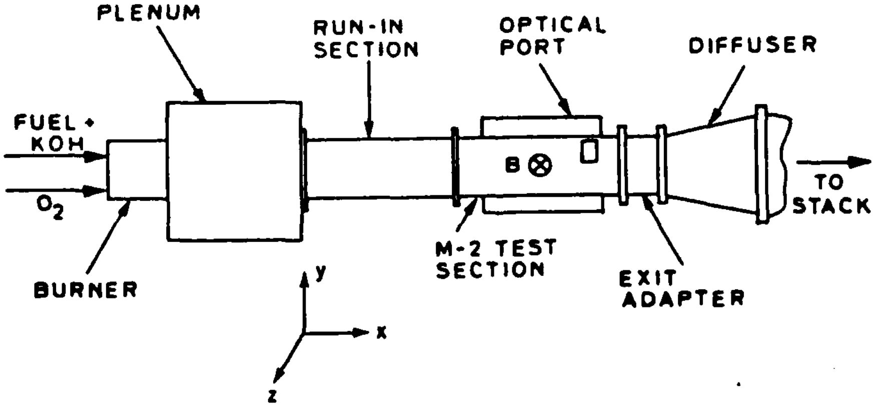
PLENUM
RUN-IN SECTION
OPTICAL PORT
DIFFUSER
FUEL + KOH
O_2
B ⊗
TO STACK
BURNER
M-2 TEST SECTION
EXIT ADAPTER
y
x
z

Fig. 3.4. M-2 flow train.

Table 3.1

Channel Geometry

Component	Dimensions (in cm)
Combustor	D = 8.9, L = 36.8
Plenum	H = 22.9, W = 17.8, L = 48.3
Nozzle	H = W = 5.08, L = 2.5
Run-in section	H = W = 5.08, L = 74.8
Active channel	H = W = 5.08, L = 74.9
Extender section	H = W = 5.08, L = 20.3
Diffuser	H = 13.3, W = 6.4 expanding to 13.3, L = 43.2
Transfer tube	D = 25.4, L = 290

Vertical exhaust/scrubber system

Distances from nozzle exit (cm):

to active channel entrance	50.8
to center of first electrode	64.1
to conductivity-measurement plane	98.4
to temperature-measurement plane	108.2
to velocity-measurement plane	108.9 (21.4 hydraulic diam.)
to center of last electrode	109.9

Electrodes: width = 5.08 cm, length = 1.81 cm.

Run conditions are listed in Table 3.2. The plasma consisted of the combustion products of ethyl alcohol burned in pure oxygen. The fuel was seeded with potassium hydroxide. The total flow rate, 54.4 g/s, at a calculated nozzle exit temperature of 2750 K, corresponded to a Reynolds number (based on hydraulic diameter) of 1.3×10^4; the calculated nozzle exit velocity was 171 m/s. This value has been used throughout to characterize the bulk velocity U_b, although it should be noted that the actual bulk velocity decreases somewhat in the downstream direction as the plasma cools. At the velocity measurement plane, which was located 21.4 hydraulic diameters downstream of the nozzle exit, the boundary layers of this turbulent flow were fully developed (or at least nearly so) in the absence of MHD interaction.

Table 3.2

Run Conditions

Fuel	Ethyl alcohol (C_2H_5OH)
N_2/O_2 ratio	0
Stoichiometry	1.05 (fuel rich)
Seed	Potassium hydroxide (KOH)
Potassium mass fraction in reactants	2.1%
Total flow rate	54.4 g/s
Reynolds number based on hydraulic diameter	1.3×10^4
Calculated core conditions at nozzle exit:	
Velocity	~ 170
Temperature	2750 K
Mass density	0.122 kg/m^3
Mach number	0.17
Electrical conductivity	14 S/m
Electron mobility	0.37 $m^2/V \cdot s$
Channel conditions:	
Wall temperatures:	
Insulator (estimated)	~ 1900 K
Electrodes	~ 1000 K
Magnetic induction	2.4 T
Electron Hall parameter	0.8
Applied Hall current	0, 3.6, 7.6, 9.3, 15.6
Magnetic interaction parameter at velocity measurement plane, based on applied Hall current	0, 0.4, 0.85, 1.1, 1.74

A.1.2 Electrical Configuration

An important goal of the experiments was to isolate the effect on the fluid flow of the Hall current, since the Faraday current itself has important effects because it induces an axial Lorentz force given by J_yB. It was also considered desirable to establish conditions which allowed, insofar as possible, for a straightforward interpretation of the measured secondary flow field. Accordingly, the channel was connected in the "Hall configuration", with a pair of electrodes at the upstream end connected through an external load to a pair of electrodes at the downstream end, as shown in Fig. 3.5. A controlled current was driven through the plasma by means of a bank of batteries, and by varying

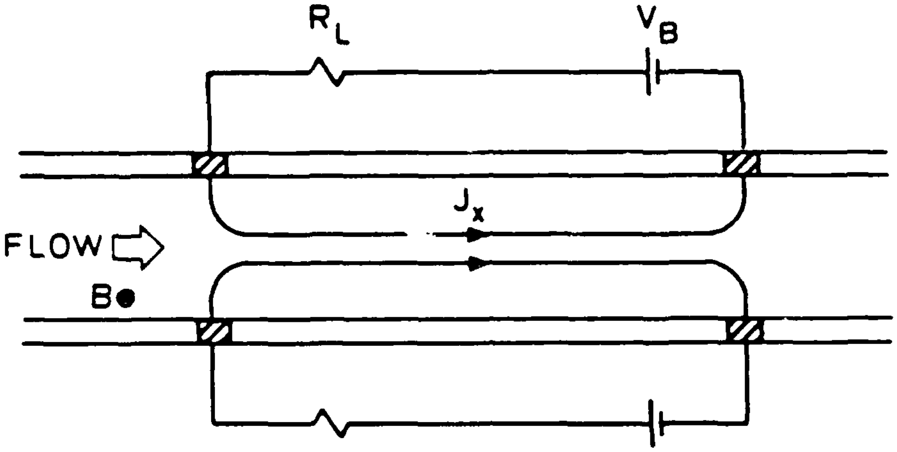

Fig. 3.5. Electrical configuration used for the main experiments.

the load resistance. Thus the experimental situation corresponded to the case illustrated in Fig. 3.2, with a positive net Hall current.

A non-dimensional parameter which indicates the strength of the electro-magnetic-fluid interaction is the Stuart number, or magnetic interaction parameter, S. For this configuration an appropriate definition of S is

$$S \equiv \frac{I_x BL}{\dot{m}U} , \qquad (3.6)$$

where I_x is the applied Hall current, L the distance from the first loaded electrode to the measurement plane, $\dot{m}$ the mass flow rate and U the mean axial velocity. The interaction parameter in this form represents the ratio of the Lorentz twisting force to the axial inertia of the flow. The interaction parameter values used are listed in Table 3.2.

A.1.3 Laser-Doppler Anemometry System

Plasma velocities were measured using laser Doppler anemometry. The LDA system, shown schematically in Fig. 3.6, used a dual-beam, single-color, backscatter configuration. The optical train consisted primarily of TSI modular components. Measurements of the x- and y-directed velocity components were made separately by rotating components of the optical train by 90°. For the y-directed measurements a

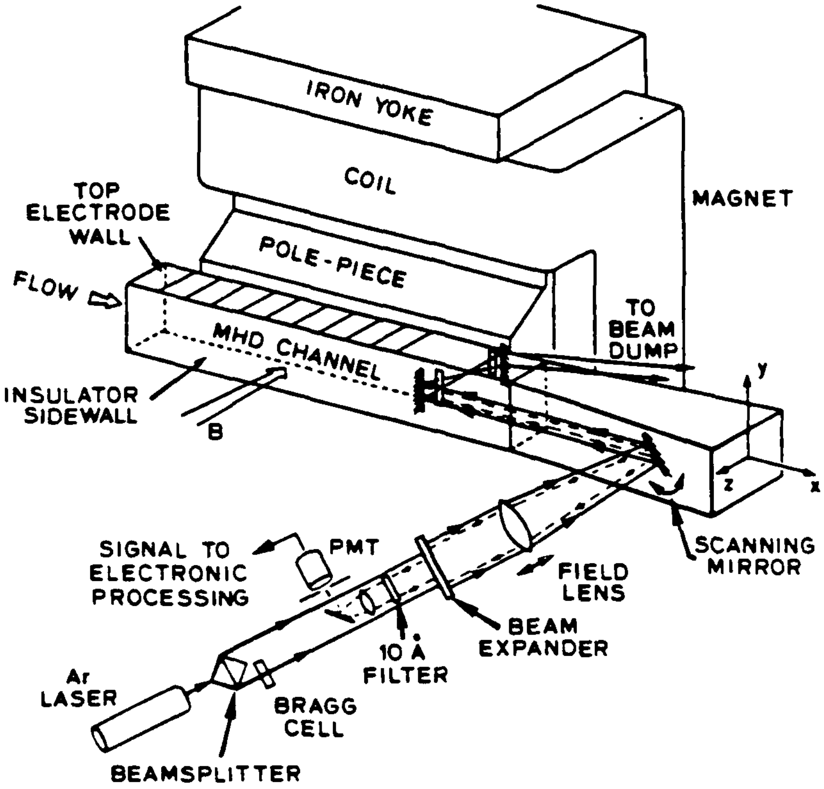
IRON YOKE
COIL
MAGNET
TOP ELECTRODE WALL
POLE-PIECE
FLOW
MHD CHANNEL
TO BEAM DUMP
INSULATOR SIDEWALL
B
y
x
z
SCANNING MIRROR
SIGNAL TO ELECTRONIC PROCESSING
PMT
FIELD LENS
BEAM EXPANDER
10 Å FILTER
Ar LASER
BRAGG CELL
BEAMSPLITTER

Fig. 3.6. Schematic of laser-Doppler anemometry optical train.

Bragg cell was used to frequency shift one of the transmitted beams by 40 MHz so as to allow discrimination of positive and negative velocities. Tight spatial and spectral filtering was used to maximize the signal-to-noise ratio of the collected scattered light; this included a narrow-line (10-Å half-width) interference filter, the purpose of which was to filter the highly radiative background emanating from the hot, potassium-laden plasma.

Suitable light-scattering centers were obtained by seeding the fuel with zirconia particles having a mean diameter of 0.7 μm. These were mixed into an alcohol-glycerine slurry and then injected into the fuel line by means of a mechanical injector utilizing a slowly-descending piston. Optical access to the plasma was provided by an open slit cut into the channel side wall and located at the leading edge of the downstream electrodes.

The photomultiplier tube signal was processed by a TSI 1990A counter-type processor interfaced to a laboratory computer. Typical data rates were ~500 Hz; total sample size was chosen in each case so that the sampling interval was about one minute.

The major sources of experimental uncertainty in these measurements were the imperfect stationarity in conditions (including combustion temperature and applied current) and the difficulty in perfectly aligning the intersecting beams for the transverse velocity measurements. The latter problem is always important in secondary flow measurements, because a slight misalignment introduces a portion of the much higher axial velocity into the transverse velocity measurement (see [3.20] for a brief review of this question in relation to secondary flow measurements made by hot-wire anemometry as well as by LDA). In the present experiments the problem was exacerbated by the fact that turning the magnet on or off caused a slight shift of the entire channel; a calibration procedure was devised to correct for the effect of this occurrence on the measured transverse velocities. A detailed uncertainty analysis by Girshick [3.21] estimated the cumulative uncertainty (to 10:1 confidence) in the mean velocity measurements as ± 0.016 for $\bar{v}/U_b$ in the MHD cases and ± 0.0055 in the non-MHD case, and ± 0.045 for $\bar{u}/U_b$, where $\bar{v}$ and $\bar{u}$ are, respectively, the y- and x-directed components of the mean velocity. The uncertainty in spatial location was estimated as ± 0.11 for y/H, ± 0.031 for z/W in the measurements of secondary flow and ± 0.042 for z/W in the measurements of axial velocity, where H and W are, respectively, the channel height and width. The major contributions to this uncertainty were the finite size of the measurement volume and the uncertainty in locating the wall.

A.1.4 Conductivity Measurements

The effect of secondary flow on the plasma conductivity profile was investigated by driving a Faraday discharge across a set of electrodes whose external circuitry was separate from that used to drive the Hall current. This set consisted of three electrode pairs located just upstream of the optical port. These electrodes were used only for the conductivity measurements, and were open-circuited at all other times.

Near-electrode voltage drops in both the x- and y-directions were obtained from a grid of iridium voltage pins inserted through a channel side wall. Voltage distributions were obtained over a range of values for J_y, and under various applied conditions, including:

(1) applied Faraday current only;

(2) both Faraday current and Hall current;

(3) Faraday current with magnetic field; and

(4) Faraday current, Hall current, and magnetic field.

For cases (3) and (4), measurements were made with the magnetic field pointing in both the positive-z and negative-z directions. The open-circuit voltage with magnetic field was measured as well. Note that only case (4) would be expected to drive secondary flow.

The voltage information was analyzed using an approximate model based on the expression, obtainable from the generalized Ohm's law,

$$\bar{\rho} = \frac{\bar{E}_y - \overline{uB} + \beta \bar{E}_x}{(1 + \beta^2) J_y} , \tag{3.7}$$

where ρ is the resistivity, E_y and E_x the electric field components, and u the axial velocity. The overbar indicates an average over a region of the cross-plane which encompasses the width W in the z-direction and ranges in the y-direction from the electrode surface to the height of the nearest voltage pin, a distance of 6.2 mm, or H/8, H being the channel height. The major assumptions of the model are that the transverse conductivity distribution in the absence of secondary flow is symmetric; that the near-electrode voltage gradients are much greater in the y-direction than in the z-direction; that the term J_y in the denominator of (3.7) is constant and can be estimated using a "current-constriction factor" obtained from a comparison of the data from cases (1) and (3) in the above list; and that β is constant. The data from the first case were also used to estimate a constant value for the cathode surface-sheath voltage drop, which was subtracted from the measured value of E_y for the near-cathode data.

A.1.5 Temperature Measurements

All electrodes were fitted with thermocouples located close to their surfaces. Of particular interest were the temperatures of the electrode pair just upstream of the velocity measurement plane, for cases in which these electrodes were not passing current. A number of measurements were recorded in which a case without secondary flow (i.e., without the simultaneous presence of magnetic field and Hall current) was immediately followed or preceded by a case with secondary flow (i.e., both were present). The change in surface temperature between these two cases could then be attributed to altered heat transfer as a result of secondary flow. As with the other measurements, data were collected for both the positive-z and negative-z orientations of the magnetic induction.

B. Experimental Results

B.1 Transverse Velocity Measurements

B.1.1 Non-MHD Case

In order to have a base case with which to compare the measurements with MHD effects present, measurements of the y-directed velocity were made for the case of zero magnetic induction and zero current. The results are shown in Fig. 3.7. The peak measured transverse velocity was 0.05 U_b. This is significantly higher than reported measurements for secondary flows driven purely by the interaction of turbulence stresses with the corners of a rectangular duct. Several factors may be involved in this discrepancy, including combustion nonuniformities and other nonidealities related to the combustor, density gradients, and the heterogeneous nature of the channel walls. (The top and bottom walls had alternating sections of brick and of electrodes, whereas the side walls had only brick.)

The data appear to indicate a top-bottom asymmetry, in that flow toward the corners appears at the bottom of the cross-plane but not at the top. This may possibly be ascribable to top-bottom density nonuniformity from the combustor. It is also possible that flow toward the top

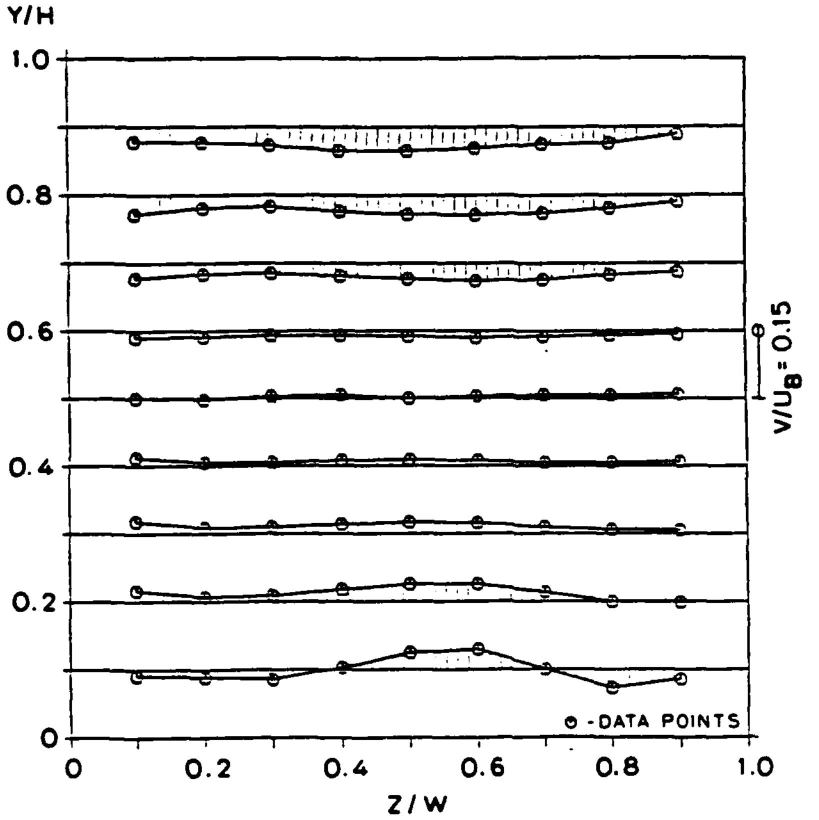

Fig. 3.7. Measurements of the mean y-directed velocity without magnetic field.

corners would have been observed had measurements been made closer to these corners.

B.1.2 MHD Case with S = 1.1

The value of the interaction parameter used in the first series of experiments was 1.1 at the plane of the velocity measurements. This value is comparable to envisioned values in large-scale channels. Measurements of the y-directed velocity were made with the magnetic field pointing in the positive-z and negative-z directions. Reversing the magnet polarity reverses the sign of the Lorentz force and so should be approximately equivalent to rotating the channel by 180° about its axis.

The measurements for the case of B pointing in the positive-z direction are shown in Fig. 3.8. In this figure and in the figures following, the secondary flow appears stronger near the left side wall than

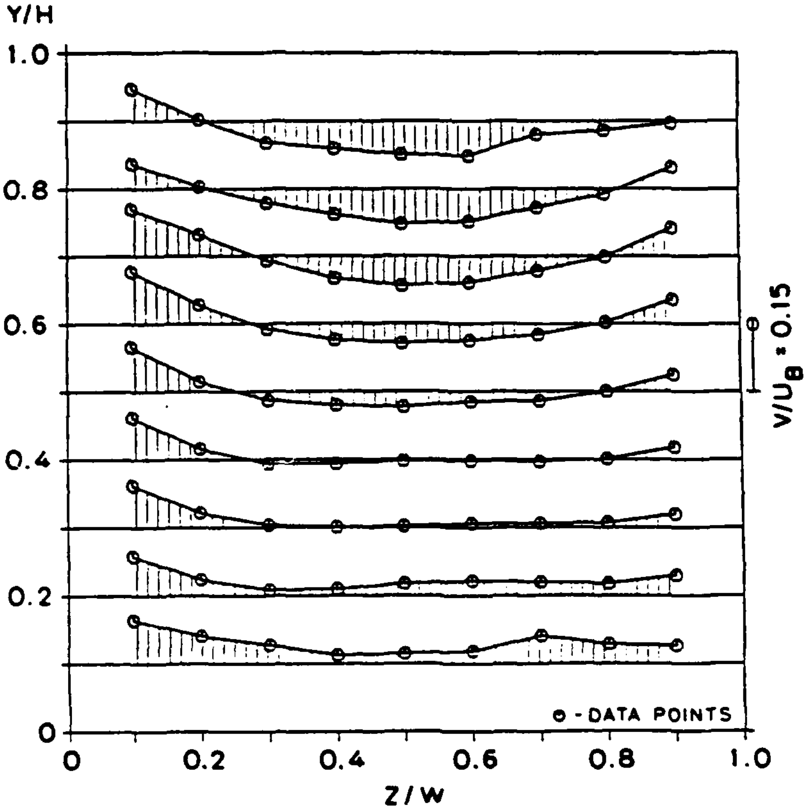

Fig. 3.8. Measurements of the mean y-directed velocity with the magnetic field pointing in the positive-z direction (S = 1.1).

near the right; it is believed that this is an artifact caused by a consistently erroneous measurement of the wall location. Shifting all the measurement locations to the left by an amount $\Delta(z/W) = 0.035$ would produce a symmetric result, which is physically what we would expect. This systematic error is additional to the uncertainty in spatial location discussed above.

In any case, the results suggest the presence of two large, counter-rotating secondary flow cells, with the flow in the core directed downward in agreement with the first-order argument illustrated in Fig. 3.2. The peak measured velocities, found in the side-wall region, measured 0.12 U_b; as the magnitude of the transverse velocity was increasing steeply toward the side wall, it is reasonable to assume that significantly higher velocities would have been found had measurements been made closer to the walls.

The vorticity is concentrated in the top half of the channel, with the vortex cells closing at about $y/H = 0.35$. An explanation for this behavior is suggested by a three-dimensional, numerical simulation performed by Maxwell et al. [3.22] for conditions which were similar to those of the present experiments. In these calculations, the secondary flow field at the upstream end of the interaction region has a symmetric structure similar to that in Fig. 3.2. As the flow progresses, hot plasma from the core has time to be swept sideways and then upwards as it follows a secondary flow path. This has the effect of increasing $\partial J_x/\partial z$ in the upper side-wall regions, which in turn intensifies the vorticity in these regions. The coupling between $\partial J_x/\partial z$ and axial vorticity causes the secondary flow cells to migrate toward the top walls in the downstream half of the channel. In this respect, the simulation and the measurements are in good agreement. The quantitative agreement is also reasonably good, although precise comparisons would require a more detailed specification than is available of the side-wall temperature distributions and of the upstream turbulence history. Both of these factors were shown in the simulation to have a substantial influence on the secondary flow field: the side-wall temperature because it affects $\partial J_x/\partial z$; the turbulence intensity because of its cross-plane smoothing effect.

The measurements in the region at the bottom of the cross-plane indicate a flow which was everywhere directed away from the bottom wall. A possible explanation for these measurements is discussed in connection with the temperature results.

In Fig. 3.9, the results for the case with the magnet polarity reversed are shown. As anticipated, the velocity field was upside-down compared to the results in Fig. 3.8. A few measurements were made in this case closer to the side walls, resulting in a peak transverse-velocity measurement of $0.15\ U_b$.

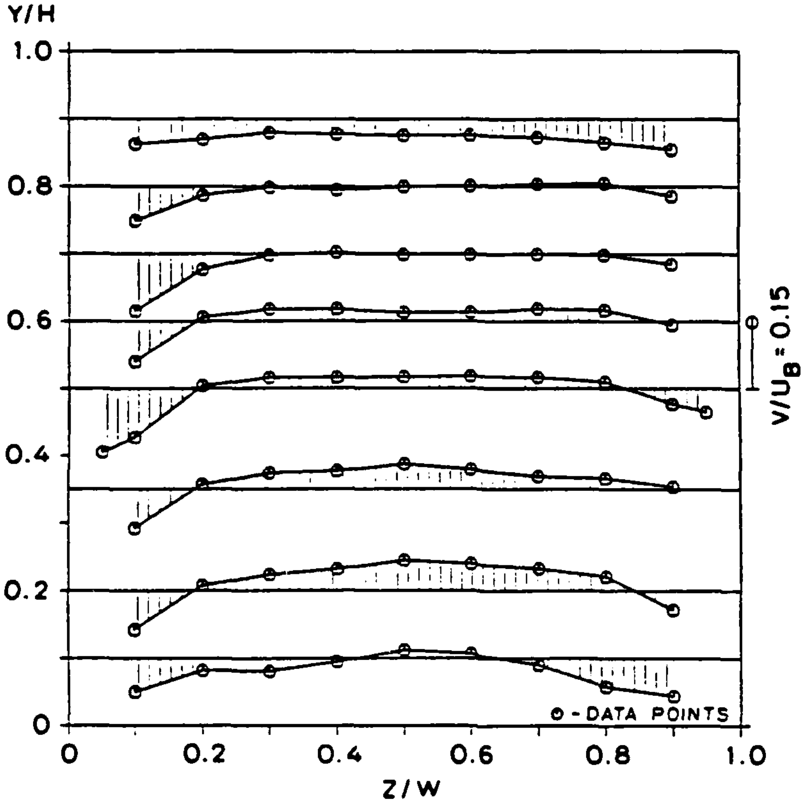

Fig. 3.9. Measurements of the mean v-directed velocity with the magnetic field pointing in the negative-z direction (S = 1.1).

B.2 Effects of Secondary Flow

The measured secondary flow field was certainly strong enough to have an effect on several aspects of the plasma momentum and thermal behavior. This section reports the results of the measurements of mean axial velocity, turbulence intensity, electrical conductivity, and electrode surface temperature.

B.2.1 Mean Axial Velocity

Measurements of the mean axial velocity with the magnetic field pointing in the positive-z direction are shown in Fig. 3.10; these results correspond to the secondary flow field shown in Fig. 3.8. The distortion of the velocity profile was dramatic: the peak velocity was forced downward from the center of the cross-plane to a position of about

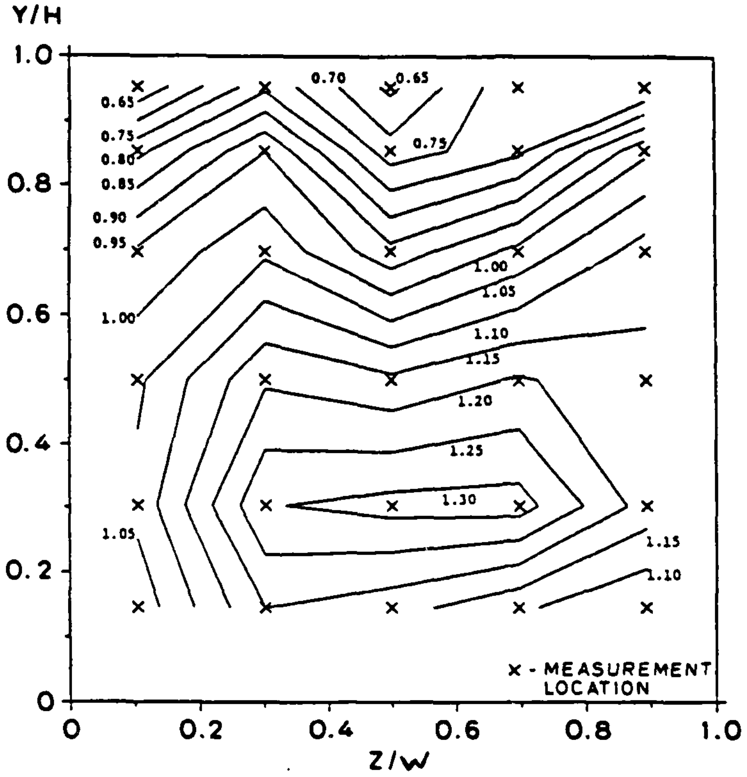

Fig. 3.10. Contour map of the measured mean x-directed velocity (normalized by U_b) with the magnetic field pointing in the positive-z direction (S = 1.1).

y/H = 0.3. The constant velocity lines near the top wall follow the vortex pattern, as slow-moving fluid was swept upward along the side wall and then pushed downward along the z-centerline. The axial velocity profiles along the z-centerline for three conditions of the magnetic field are shown in Fig. 3.11. As expected, the profile was symmetric when Lorentz forces were absent; with Lorentz forces present, the profile became strongly skewed according to the direction of the force.

These results are similar to the measurements reported by McClaine et al. [3.17]. In their experiments, performed in the larger Avco Mk VI channel, the conditions included a magnetic induction of 4T, an interaction length of 2.5 m, and peak velocities of about 1000 m/s. Unfortunately, the electrical loading which was used during these particular measurements was not reported; their tests encompassed a wide range of loading conditions in both Faraday and diagonal configurations.

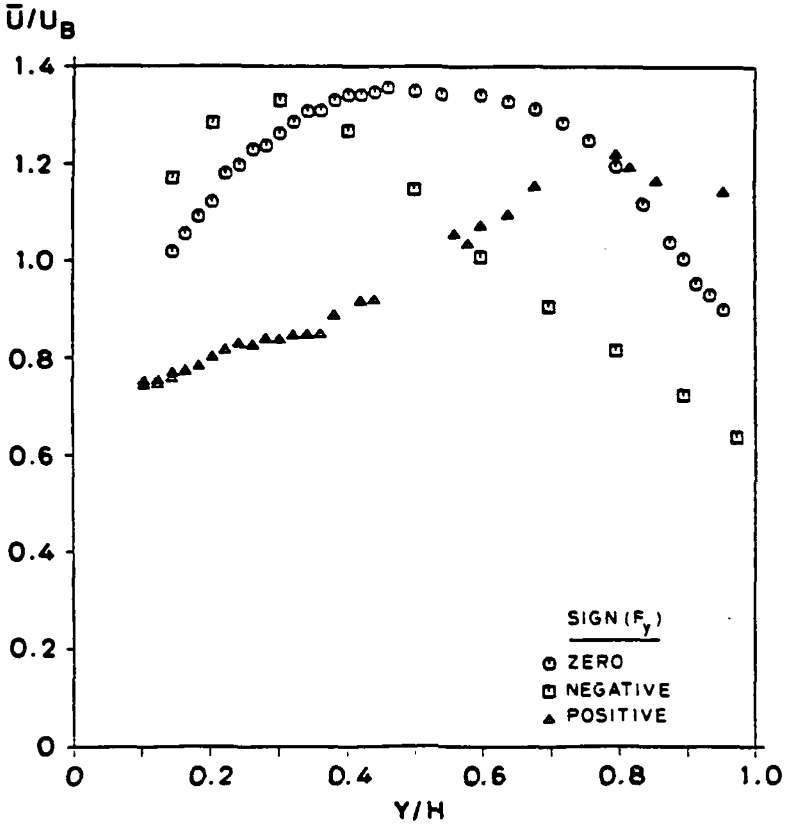

Fig. 3.11. Measurements of the mean x-directed velocity along the z-centerline, for three conditions of the transverse Lorentz force F_y ($S = 1.1$).

While the axial velocity profiles measured in the present experiments were strongly skewed, there was no evidence of the occurrence of a magneto-aerothermal instabilitiy. This is not remarkable in view of the fact that the experiments were designed to suppress the Faraday current while imposing a Hall current. In the magneto-aerothermal case, the Hall current is driven by the conductivity nonuniformity encountered by the Faraday current; this nonuniformity is then amplified by secondary flows driven by the Hall current [3.12]. In the present experiments, the local Hall current is still coupled to secondary flow, but the regulation of the total Hall current may have precluded the emergence of an instability.

B.2.2 Turbulence Intensity

Previous measurements of turbulence intensity in the Stanford M-2 channel have found relatively high values of the center-point axial turbulence intensity $\tilde{u}_c/\bar{u}_c$, where $\tilde{u}_c$ is the turbulence velocity (the standard deviation of the velocity-probability-distribution function) and $\bar{u}_c$ is the center-point mean velocity. For example, Reis and Kruger [3.23] measured values ranging from 6.6% to 9.6% for a variety of non-MHD flow cases; in the present experiments, several measurements of $\tilde{u}_c/\bar{u}_c$ yielded values ranging from 5.8% to 6.3%. For comparison, Melling and Whitelaw [3.20] in their water-flow experiment measured values of 4-5% at an axial location where the boundary layers had merged. It has been conjectured that the relatively high axial turbulence in the Stanford channel is caused by combustion nonuniformities. The measured value in the non-MHD case of the y-directed core turbulence $\tilde{v}$, again normalized by $\bar{u}_c$, was 3.75%; this is virtually identical to the value reported by Melling and Whitelaw.

Measurements of the y-directed turbulence intensity in the non-MHD case are shown in Fig. 3.12, in which the measured values of $\tilde{v}$ have been normalized by U_b. As expected, the distribution was symmetric and $|\tilde{v}|$ was greater near walls parallel to y than near walls normal to y.

The measurements made in the MHD case, with the magnetic field pointing in the positive-z direction, are shown in Fig. 3.13. The region of minimum turbulence (whose magnitude was somewhat less than in the non-MHD case because of turbulence damping by the magnetic field; cf. [3.23]) was shifted downward by Lorentz forces.

The measurements for $\tilde{u}/U_b$, shown in Fig. 3.14, exhibited the same effect; these same measurements are shown in Fig. 3.15 normalized instead by the local mean velocity $\bar{u}$. In these measurements, there appears to be a region beneath the center of the top wall where the turbulence was greater than its value closer to the wall; this might be explainable in terms of secondary-flow convection.

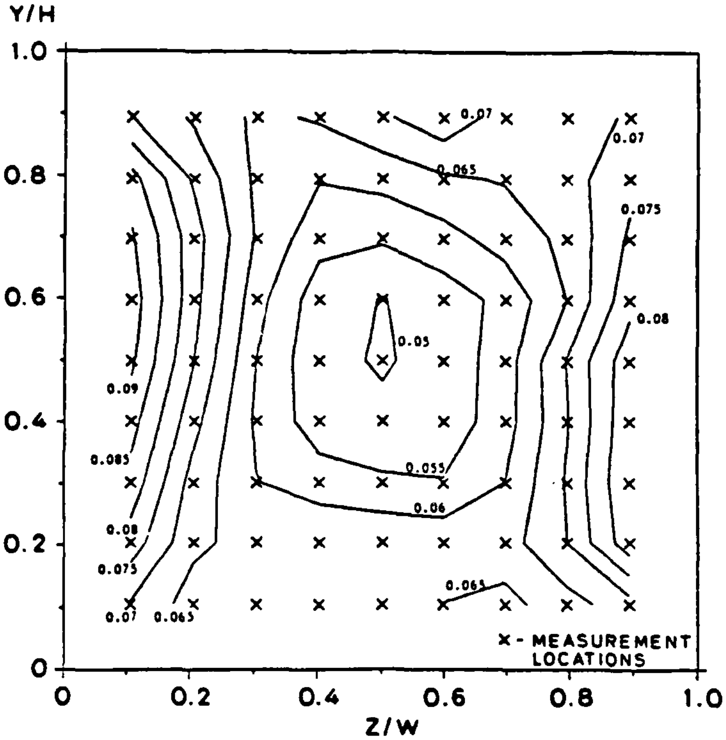

Fig. 3.12. Contour map of the measured y-directed turbulence intensity (normalized by the bulk axial velocity) without magnetic field (S = 1.1).

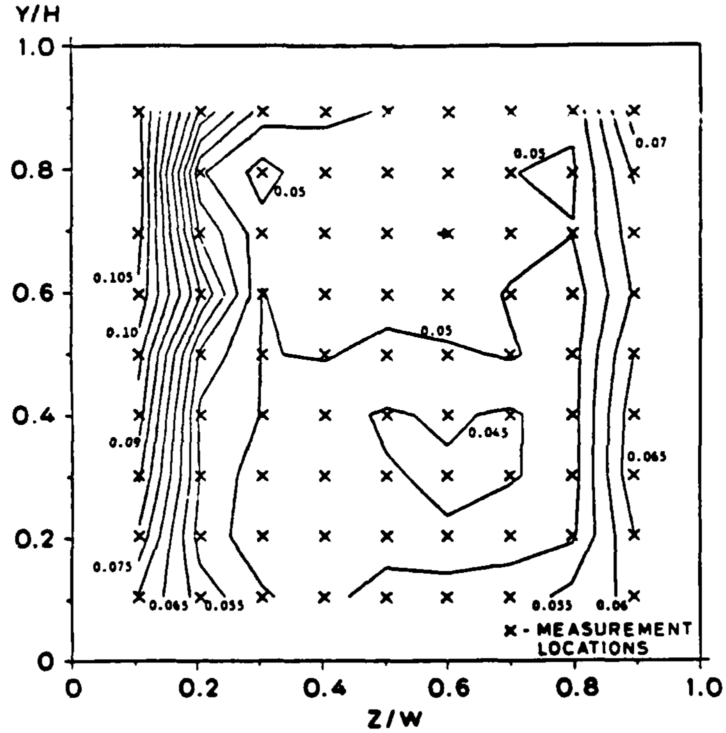

Fig. 3.13. Contour map of the measured y-directed turbulence intensity (normalized by the bulk axial velocity) with the magnetic field pointing in the positive-z direction (S = 1.1).

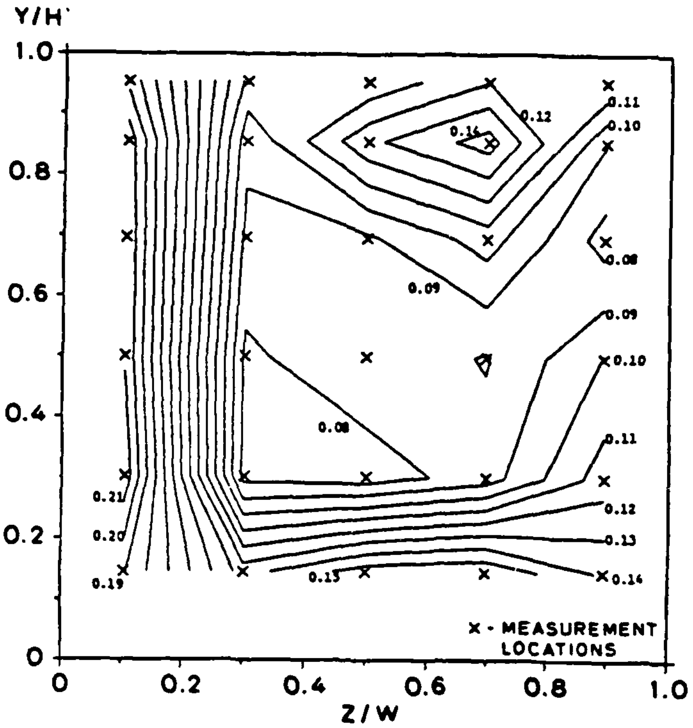

Fig. 3.14. Contour map of the measured x-directed turbulence intensity (normalized by the bulk axial velocity), with the magnetic field pointing in the positive-z direction (S = 1.1).

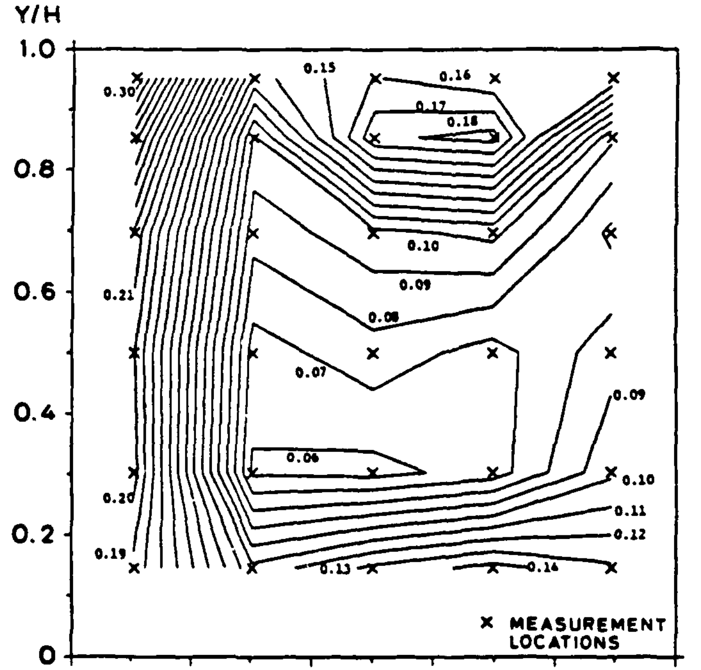

Fig. 3.15. Contour map of the measured x-directed turbulence intensity (normalized by the local mean axial velocity) with the magnetic field pointing in the positive-z direction (S = 1.1).

B.2.3 Electrical Conductivity

The results of the conductivity measurements for the MHD cases are summarized in Fig. 3.16, in which the near-electrode resistivity defined by eq. (3.7) has been normalized by the value of the core conductivity measured without magnetic field. The term "anode region" and "cathode region" refer, respectively, to the regions adjacent to the top and bottom electrodes which were used for the conductivity measurements. The abscissa in this figure represents the value of the core current density associated with the Faraday discharge; for all the data shown, the Hall circuit was active as well, corresponding to Case (4) described earlier.

The decrease in resistivity as J_y increased was an expected consequence of Joule heating. Otherwise, these results indicate that secondary flow caused the resistivity distribution to become significantly asymmetric. The boundary layer receiving cold side-wall fluid was much more resistive than the boundary layer toward which hot core fluid was directed; the average value of the ratio of the higher resistivity to the value at the opposite wall was 1.8. The importance of these results is that near-electrode voltage drops, which are a performance-limiting effect in combustion MHD devices, can be significantly altered by secondary flow.

B.2.4 Electrode Surface Temperatures

Thirteen separate measurements were made of the effect of secondary flow on electrode surface temperatures, as described earlier. The results are shown in Fig. 3.17. Each point in this figure represents the temperature with secondary flow (with simultaneous Hall current and magnetic field) minus the temperature without secondary flow (without current); the latter temperature was typically about 1000 K. A separate analysis of data not shown in the figure indicates that the presence of magnetic field alone made no difference in the temperature, while the presence of Hall current alone caused a warming of both the top and bottom electrodes by an average of about 10 K, because of Joule heating.

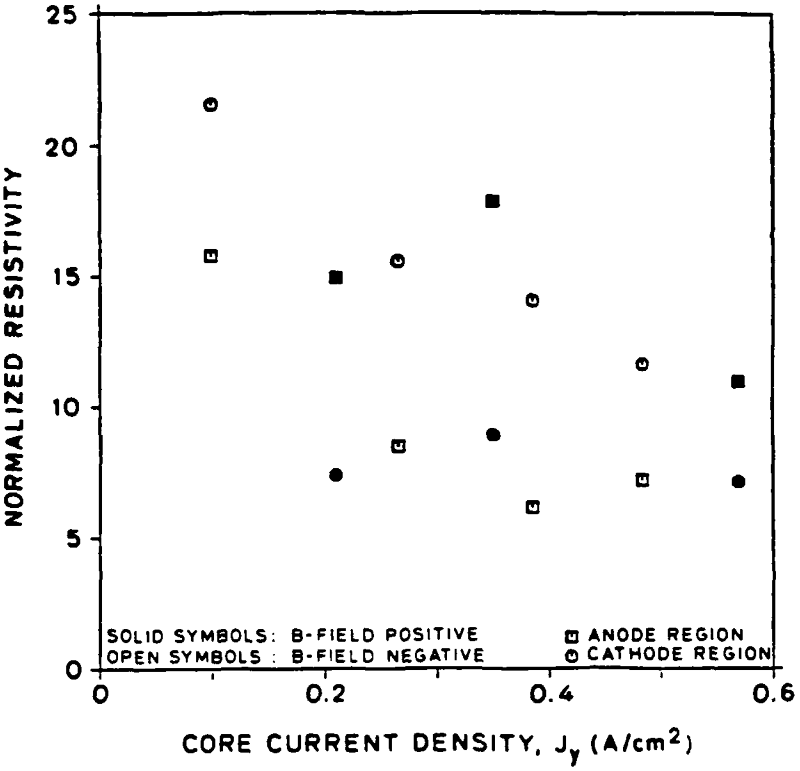

Fig. 3.16. Summary of resistivity results for cases with complete electrical configuration and magnetic field (S = 1.1).

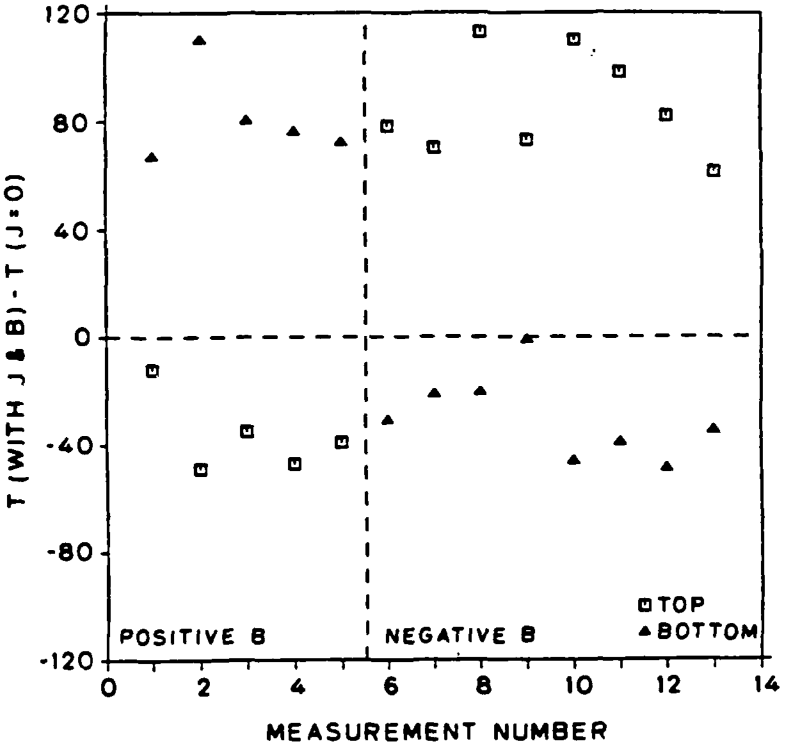

Fig. 3.17. Measured electrode surface temperatures with Hall current and magnetic field minus reference measurements without current (S = 1.1).

The effect of secondary flow in the positive-B case is seen to be a substantial heating of the bottom electrode and a smaller but still significant cooling of the top electrode--reversing the magnet polarity reversed the results. The electrode toward which hot core fluid was pushed was heated on the average by 85 K; the opposite electrode was cooled by an average of 32 K. Using the fact that the electrodes were cooled by water at about 300 K, it appears that secondary flow caused a 12% increase in the heat flux from the plasma to the heated electrode and a 5% reduction in the heat flux to the cooled electrode.

Aside from the obvious conclusion that secondary flow has the expected qualitative asymmetric effect on heat transfer to the top and bottom walls, it is interesting to consider the surprising result that the effect at the heated electrode was more than twice as great as the effect at the cooled electrode. This result is surprising, first, because the secondary flow cells appeared to be concentrated near the cooled electrode, and, second, because the resistivity measurements showed the opposite trend, with a stronger effect being observed in the region adjacent to the cooled electrode.

A possible explanation is as follows. As already noted, the secondary flow cells not only sweep cold side-wall fluid into the top-wall boundary layer, but also eventually convect hot core fluid around a loop into the same boundary layer in the side-wall region. As the stainless-steel electrodes are thermally quite conductive, the net result is that the cooling effect is mitigated; no such effect occurs for the boundary layer of the bottom wall, toward which core fluid has been pushed but which has less vortical mixing. Distortion of the turbulence distribution could also be a factor in the asymmetrical heat transfer. Near-electrode voltage drops, on the other hand, are dependent on complex physical processes which are strongly but nonlinearly temperature-dependent. Since the calculated resistivities were averaged over an area described earlier, it is not remarkable that the net quantitative effects for the resistivity distribution could be quite different from that for heat transfer, although the qualitative trends were the same.

The temperature results suggest a possible explanation for the secondary flow measurements in the region near the bottom wall (in the positive-B case). The substantial warming of the bottom electrode suggests that the mass density near the bottom wall may have been decreasing in the axial direction, causing a net reduction in the axial mass flux which would have to be balanced by a flow away from the wall. Flow away from the bottom wall did not appear in the simulation of Maxwell et al. [3.22]. However, their calculations assumed a constant wall temperature. It is possible that such a flow effect might appear in the simulations if the wall temperature were coupled to the flow field.

B.3 Dependence of Secondary Flow and Related Effects on Interaction Parameter

Since secondary-flow phenomena are highly complex and nonlinear, it is important to determine their dependence on driving parameters. The simplest theoretical description of secondary flow suggests that the magnitude of the secondary-flow velocities should be directly proportional to the interaction parameter, previously defined in eq. (3.6). Experiments were conducted to determine the actual dependence, and the results are discussed here.

A straightforward, although indirect, measure of the magnitude of the secondary flow is the displacement of the axial velocity profile--as in Fig. 3.11. Figure 3.18 shows the effect of the interaction parameter on this displacement of the axial velocity for three values of interaction parameter, $S = 0.1$, 0.4, and 0.85. It is notable that the displacement is significant even for the modest interaction $S = 0.4$. Figure 3.19 shows the corresponding effect on turbulence intensity for the same interaction parameter values. It is evident from these data that the secondary flow does scale with the interaction parameter, at least for interaction-parameter values less than approximately $S = 1$. For interaction parameter values above this level, however, the magnitude of the secondary flow does not appear to change markedly. This is seen in Fig. 3.20, in which the axial profiles have been replotted with the additional case $S = 1.74$ included, and in Figs. 3.21 and 3.22, which

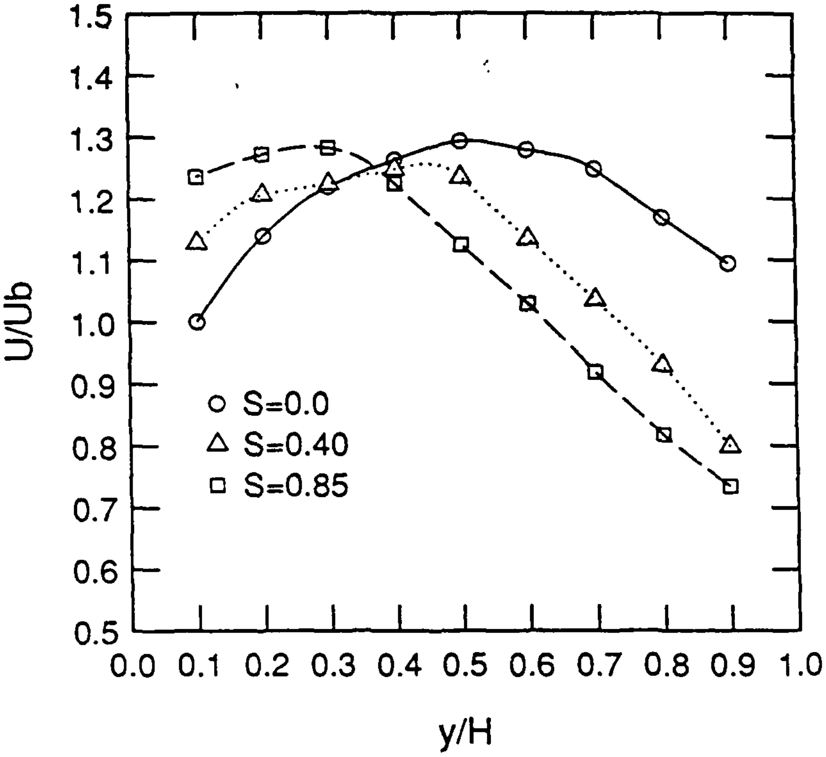

Fig. 3.18. Measurements of the mean x-directed velocity along the z-centerline, for three values of interaction parameter S.

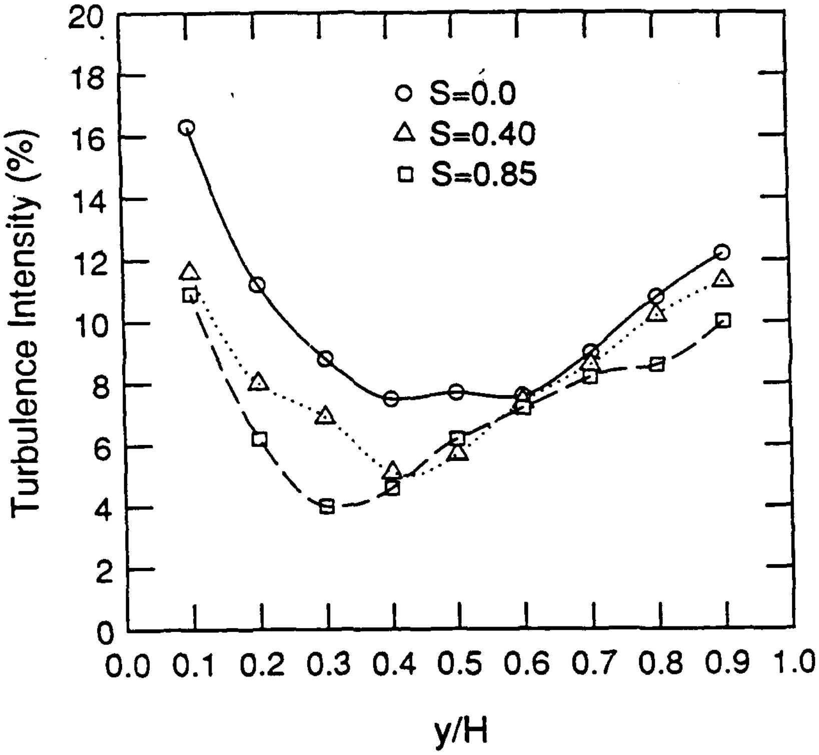

Fig. 3.19. Measurements of the x-directed turbulence intensity (U/U_b) along the z-centerline, for three values of interaction parameter S.

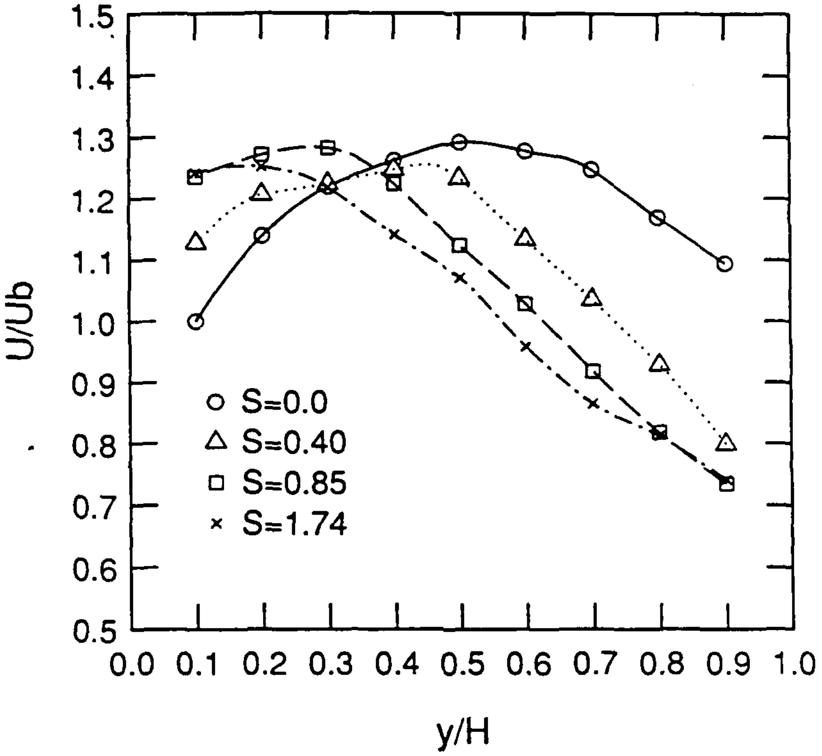

Fig. 3.20. Measurements of the mean x-directed velocity along the z-centerline, for four values of interaction parameter -S.

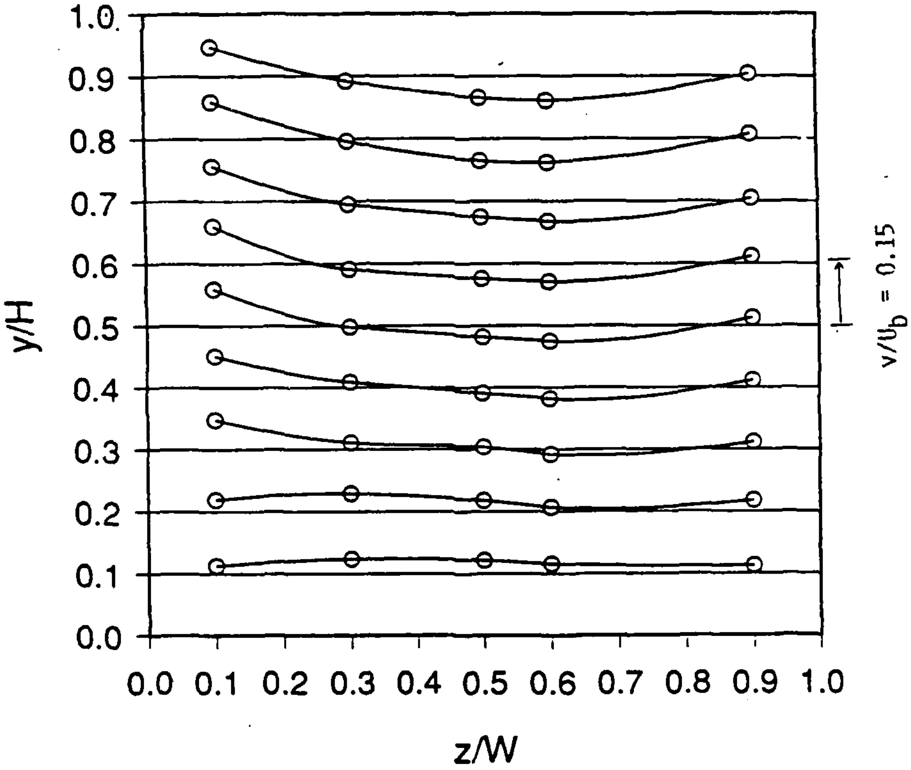

Fig. 3.21 Measurements of the mean y-directed velocity (normalized by U_b) for interaction parameter S = 0.85.

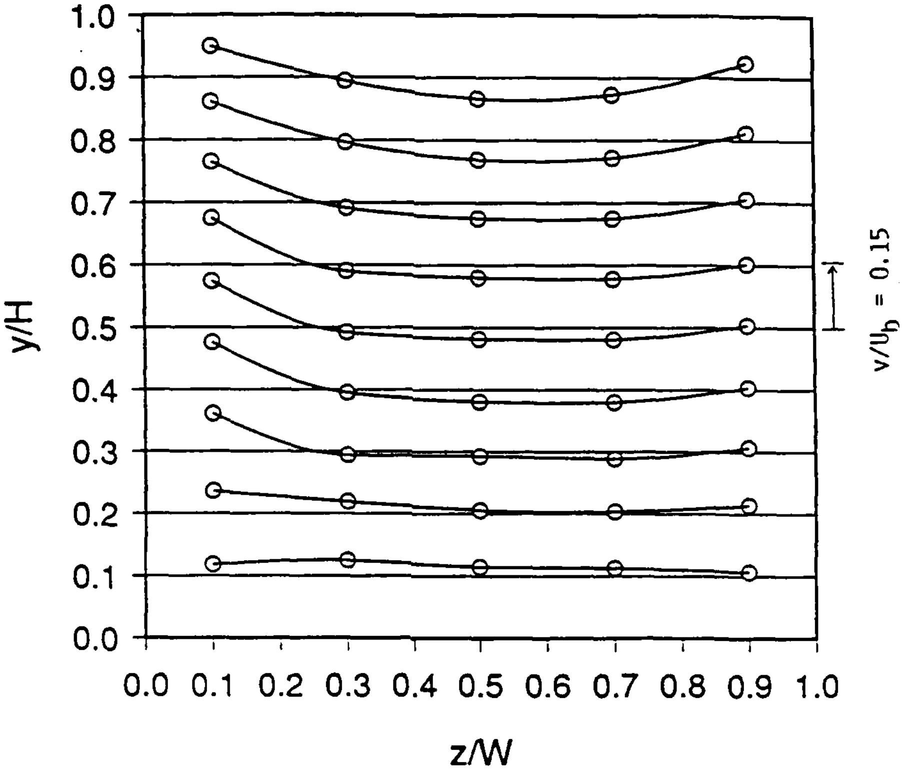

Fig. 3.22 Measurements of the mean y-directed velocity (normalized by U_b) for interaction parameter S = 1.74.

show the y-directed velocity mapped over the cross plane for the two cases S = 0.85 and S = 1.74, respectively. It is seen that the secondary flow appears to "saturate" for high interaction parameters. This apparent saturation was not anticipated prior to the experiments actually being conducted. This effect may result at least in part from the fact that the secondary flow causes a major redistribution in the flow field which, by altering the conductivity distribution, couples back to the driving Lorentz forces in a nonlinear way.

B.4 Summary and Conclusions

Experiments were conducted to measure MHD-induced secondary flow. The results included the first direct, quantitative measurements of secondary flow in a combustion MHD channel. The experiments were performed in a laboratory channel, with dimensions an order of magnitude smaller than in envisioned full-scale MHD devices; however, the use of an applied Hall current and of a relatively low axial velocity allowed values for the magnetic interaction parameter based on the Hall current comparable to anticipated values in the core of large-scale MHD channels.

Laser-Doppler anemometry measurements of transverse velocities under various controlled conditions showed that Lorentz forces caused large-scale secondary flows to develop over a downstream channel cross-plane. Peak measured transverse velocities were as high as 15% of the bulk velocity. The structure of the measured secondary flow field was qualitatively in accord with simple models, with a concentration of the vortices toward the top wall explainable in terms of the coupling between axial vorticity and nonuniformities in the Hall current density.

The simplest theoretical description of secondary flow indicates that the magnitude of the secondary flow velocities should be directly proportional to the interaction parameter. However, the experiments showed that secondary flow causes a major redistribution of the flow which couples back to the driving Lorentz forces in a nonlinear way. The magnitude of the flow appears to "saturate" for interaction parameter values greater than approximately $S = 1$.

Several effects of MHD secondary flow were also investigated, including the skewing of the cross-plane distributions of mean axial velocity and of the axial and transverse components of turbulence intensity, and the development of asymmetries in the wall heat flux and in the near-electrode conductivity. These results consistently demonstrated that secondary flow exerted a profound influence on the plasma momentum, thermal, and electrical behavior. The major conclusion is that secondary flow is an important effect which needs to be accurately assessed in designing full-scale MHD devices.

3.0 REFERENCES

1.1 Mitchner, M., and C.H. Kruger, Jr., *Partially Ionized Gases*, John Wiley & Sons, Inc., 1973.

1.2 Bates, D.R., V. Malaviya, and N.A. Young, "Electron-Ion Recombination in a Dense Molecular Gas," Proc. Roy. Soc. A-*320*, 437 (1971).

1.3 Kelley, R., and P.J. Padley, "Measurement of Collisional Ionization Cross Sections for Metal Atoms in Flames," Proc. Roy. Soc. *A-327*, 345 (1972).

1.4 Bates, D.R., "Ionization and Recombination in Flames," Proc. Roy. Soc. *A-349*, 427 (1976).

1.5 Hinnov, E., and J.G. Hirschberg, "Electron-Ion Recombination in Dense Plasmas," Phys. Rev. *125*, 795 (1962).

1.6 Shapiro, A.H., *The Dynamics and Thermodynamics of Compressible Fluid Flow*, Vol. I. The Ronald Press Co., 1953.

1.7 Mitchner and Kruger, Jr., 1973, p. 146.

1.8 Ibid., p. 32.

1.9 Ibid., p. 52.

1.10 Marr, G.V., *Photoionization Processes in Gases*, Academic Press, 1967, p. 236.

1.11 Herzburg, G., *Spectra of Diatomic Molecules*, Van Nostrand Reinhold, 1950, p. 449.

1.12 Spears, K.G., "Ion-Neutral Bonding," J. Chem. Phys. *57*, 1850 (1972).

1.13 Dzidic, J., and P. Kebarle, "Hydration of the Alkali Ions in the Gas Phase. Enthalpies and Entropies of Reactions $M^+(H_2O)_{n-1} + H_2O = M^+(H_2O)_n$," J. Phys. Chem. *74*, 1466 (1970).

1.14 Patrick, R., and D.M. Golden, "The Temperature Dependence of Ion-Molecule Association Reactions," J. Chem. Phys. *82*, 75 (1985).

1.15 Franklin, J.L. (Ed.), *Ion-Molecule Reactions*, Dowden, Hutchinson, and Ross, 1979.

1.16 Vincenti, W.G., and C.H. Kruger, Jr., *Introduction to Physical Gas Dynamics*, Krieger, 1965, p. 144.

1.17 Ibid., Chapter IV.

1.18 Ibid., p. 524.

1.19 Stogryn, D.E., and A.P. Stogryn, Mol. Phys. 11, 371 (1966).

1.20 Searles, S.K., and P. Kebarle, "Hydration of the Potassium Ion in the Gas Phase: Enthalpies and Entropies of Hydration Reactions $K^+(H_2O)_{n-1} + H_2O = K^+(H_2O)_n$," Can. J. Chem. 47, 2619 (1969).

1.21 Niles, F.E., J.M. Heirmerl, G.E. Keller, and L.J. Puckett, "Reactions Involving Cluster Ions," Radio Science 7, 117 (1972).

1.22 Janaf Thermochemical Tables, Second Ed., NSRDS-NBS-37, 1971.

1.23 Loeb, L.B., Basic Processes of Gaseous Electronics, Univ. of California Press, 1955, p. 590.

1.24 Clifton, D.G., "Ideal Gas Treatment of the Equilibrium Composition, Enthalpy Function, and Heat Capacity of Cesium Vapor and Cesium Plasma," Los Alamos Report LA-2419, 1960, p. 13.

1.25 Harris, L.P., J. Appl. Phys. 36, 1543 (1965).

1.26 McGowan, J.Wm., and J.B.A. Mitchell, "Electron-Molecular Positive-Ion Recombination," in Electron-Molecule Interactions, L.G. Christophorou (Ed.), Vol. 2, p. 65, 1984.

1.27 Keller, G.E., and R.A. Beyer, "CO_2 and O_2 Clustering to Sodium Ions," J. Geophys. Res. 76, 289 (1971).

1.28 Hirschfelder, Molecular Theory of Gases and Liquids, Wiley, 1954, p. 946.

1.29 Slater et al., Phys. Rev. A, 17, 201 (1978).

1.30 Roth, A., Vacuum Technology, North Holland, 1876, p. 156.

1.31 Ibid., p. 144.

1.32 Doucet, H., A. Truc, and A. Richardt, "Piegeage des vapeurs d'eau et d'oxygene dans une enceinte en haut vide et an vide clasique," Le Vide 132, 347 (1967).

1.33 Lyons, R.N. (Ed.), Liquid Metals Handbook, U.S. Government Printing Office, Office of Naval Research and the Atomic Energy Commission, Washington, D.C., 1950. (1952 and 1956 editions also available).

1.34 General Electric, Nela Park, Cleveland, OH. Lucalox is also manufactured under the trade name Vistal. (G. E. sells tubing in sizes appropriate for sodium arc lamps, ranging from 5 mm O.D., 5" length to 8.8 mm O.D., 10" length.)

1.35 Johnson, D.E., "Ultraviolet and Visible Absorption Spectra of Potassium and Porassium-Xenon Mixtures," Ph.D. Thesis, University of Illinois at Urbana-Champaign, 1985. (The appendix contains a complete and up-to-date literature survey of materials with alkali metal compatibility.)

1.36 Gupta, R., et al., "Absorption Studies of Cs_2 and Rb_2 Molecular Bands in the Visible and Near Visible," J. Chem. Phys. 68(3), 799 (1978).

1.37 Berry, W., Corrosion in Nuclear Applications, Corrosion Monograph Series, J. Wiley & Sons, New York, 1971.

1.38 Agnew, L., and C. Summers, "Isothermal Plasma Oven," Rev. Sci. Instr. 37(9), 1224 (1966).

1.39 Mausteller, J.W., F. Tepper, and S.J. Rodgers, Alkali Metal Handling and Systems Operating Techniques, Gordon & Beach, 1967. (A good reference, available from the American Nuclear Society, 555 North Kensington Av., La Grange, IL 60525, phone (312) 352-6611.)

1.40 Rhodes, W.H., in Van Nostrand's Scientific Encyclopedia, 6th Ed., 1983, p. 1580.

1.41 Winslow, P.M., "Corrosivity of Cesium," Corrosion 221(11), 341 (1965).

1.42 Shaffer, High Temperature Materials.

1.43 Miller, G.L., Tantalum and Niobium, Academic Press, 1959.

1.44 Cajon Co., Macedonia, OH 44056.

1.45 Len Reed, International Associates, Santa Clara, CA. Private communication.

1.46 MDC, Hayward, CA. Vacuum products manufacturer.

1.47 Helicoflex, Boonton, NJ; Advanced Products, North Haven, CT; Pressure Science, Beltsville, MD.

1.48 "Introduction to NaK and BZ Alloys," a bulletin of the Callery Chemical Co., Callery, PA 16024.

1.49 Vidal, C.R., and J. Cooper, "Heat-Pipe Oven: A New, Well-Defined Metal Vapor Device for Spectroscopic Measurements," J. Appl. Phys., 40(8), 3370 (1969).

1.50 Vidal, C.R., and F.B. Haller, "Heat Pipe Oven Applications. I. Isothermal Heater of Well Defined Temperature. II. Production of Metal Vapor-Gas Mixtures," Rev. Sci. Instr. 42(12), 1779 (1971).

1.51 Vidal, C.R., and M.M. Hessel, "Heat-Pipe Oven for Homogeneous Mixtures of Saturated and Unsaturated Vapors; Application to NaLi," J. Appl. Phys. 43(6) (1972).

1.52 Wisoff, P.J.K., and R.G. Caro, "A Superheated Na Cell for X-Ray Photoionization Experiments," Appl. Phys. B, 35, 65-69 (1984).

1.53 Roth, A., Vacuum Technology, North-Holland, 1982.

1.54 Carslaw and Jaeger, Conduction of Heat in Solids, Oxford, 1959, pp. 230-234.

1.55 Batchelor, G.K., An Introduction to Fluid Dynamics, Cambridge, 1980, p. 235.

1.56 Corney, A., Atomic and Laser Spectroscopy, Clarendon, Oxford, 1977.

1.57 Miles, R.B., and S.E. Harris, "Optical Third Harmonic Generation in Alkali Metal Vapors," IEEE J. Quantum Electronics, QE-9(4), 472 (1973).

1.58 Chen, S., and M. Takeo, "Broadening and Shift of Spectral Lines Due to the Presence of Foreign Gases," Rev. Mod. Phys., 29, 20-73 (1957).

1.59 Fabry, M., and J.R. Cussenot, "Determination theorique et experimentale des forces d'oscillateur des transitions de l'atomie de cesium," Can. J. Phys., 54, 836 (1976).

1.60 Mitchel and Zemansky, Resonance Radiation and Excited Atoms, 1961, pp. 93-96.

1.61 Nygaard, K.J., "On the Effect of Cs in Photoionization Laser Plasmas," IEEE J. Quantum Electronics, QE-9, 1020 (1973).

1.62 Dutton, J., "A Survey of Electron Swarm Data," J. Phys. Chem. Ref. Data 4(3) 577 (1975).

1.63 Heald, M.A., and C.B. Warton, Plasma Diagnostics with Microwaves, Wiley, 1965, p. 9.

1.64 Baum, E., and R.L. Chapkis, "Theory of a Spherical Electrostatic Probe in a Continuum Gas: An Exact Solution," AIAA J. 8(6), 1073 (1970).

1.65 Chung, R.M., L. Talbot, K.J. Touryan, "Electric Probes in Stationary and Flowing Plasmas: Part II," AIAA J. 12(2), 144 (1974).

1.66 Kruger, C.H., et al., "Fundamental Processes in Partially Ionized Plasmas," Technical Proposal, Proposal No. MET 83-86 (Ren), Grant AFOSR-83-0108, August 1986.

1.67 Johnsen, R., "r-f Probe Method for Measurements of Electron Densities in Plasmas at High Neutral Densities," Rev. Sci. Instr. 57(3), 428 (1986).

1.68 Persson, K.B., "A Method for Measuring the Conductivity in a High Electron Density Plasma," J. Appl. Phys. 32(12), 2631 (1961).

1.69 Huddlestone, R.H., and S.L. Lenard, Plasma Diagnostic Techniques, Academic Press, 1965.

1.70 James, R.K., "Joule Heating Effects in the Electrode Wall Boundary Layer of MHD Generators," Ph.D. Thesis and HTGL Report #115, Stanford University, 1980.

1.71 Agnews, L., and C. Summers, "Quantitative Spectroscopy of Cesium Plasmas," in Proc., 7th International Conference on Phenomena in Ionized Gases, Belgrade, 1965, p. 574.

1.72 Borghi, C.A., "Discharges in the Inlet Region of a Noble Gas MHD Generator," Ph.D. Thesis, Eindhoven University of Technology, 1982.

1.73 Bates, D.R., A.E. Kingston, and R.W.P. McWhirter, "Recombination Between Electrons and Atomic Ions: I. Optically Thin Plasmas," Proc. Roy Soc. A-267, 297 (1962).

1.74 Mitchner and Kruger, Jr., 1973, p. 457.

2.1 Davidson, B., Neutron Transport Theory, Clarendon Press, Oxford, 1958.

2.2 Kalnavarns, J., and G.K. Bienkowski, "Continuum Theory for the Interaction of a Weakly Ionized Gas with an Emitting Surface," Phys. Fluids 20(10), 1657-1667 (1977).

2.3 Schottky, W., Ann. d. Physik 44, 1011-1032 (1914).

2.4 Messerle, H.K., and A. Manglick, "Temperature Sheaths on Probes or Electrodes in MHD Plasmas," J. Phys. D.: Appl. Phys. 11, 1073-1084 (1978).

2.5 Messerle, H.K., and A. Manglick, "Electrostatic Breakdown of Boundary Layers on Electrodes," in Proc., 7th International Conference on MHD Power Generation, Cambridge, MA, Vol. II, 1980, pp. 733-737.

2.6 Cheng, W.K., M. Martinez-Sanchez, and D. Dvore, "Surface Field Limitation in Diffuse Anodic Discharges," J. Energy 7(6), 518-522 (1983).

2.7 Langmuir, I., "The Pressure Effect and Other Phenomena in Gaseous Discharges," J. Franklin Inst. 196, 751 (1923). Also in The

Collected Works of Irving Langmuir, C. Guy Suits (Ed.), Pergammon Press, 1961, Vol. 5, pp. 1-10.

2.8 Kemp, R.F., and J.F. Sellen, "Plasma Potential Measurements by Electron Emissive Probes," Rev. Sci. Instr. 37(4), 455-461 (1966).

2.9 Chang, K.W., and G.K. Bienkowski, "Effects of Electron Emission on Electrostatic Probes at Arbitrary Pressures," Phys. Fluids 13(4), 902-920 (1970).

2.10 Argyropolous, G.S., et al., "Electron Equilibrium in Open-Cycle MHD Generators," AIAA J. 12(5), 669-671 (1974).

2.11 Okazaki, K., et al., Analysis of the Combustion Gas Boundary Layer Near a Cold Cathode," AIAA J. 15(2) 1778-1784 (1977).

2.12 Chung, P.M., "Near Surface Electron Temperature of Weakly Ionized Plasma, According to Kinetic theory," Phys. Fluids 12(8), 1623-1634 (1969).

3.1 Fay, J.A., "Hall Effects in a Laminar Boundary Layer of the Hartmann Type," Avco-Everett Research Report 81, 1959.

3.2 Broer, L.J.F., L.A. Peletier, and L. van Wigngaarden, "A Mechanical Hall Effect," Appl. Sci. Res. Sect. B, 8, 259 (1960).

3.3 Sato, H., "The Hall Effect in the Viscous Flow of Ionized Gas between Parallel Plates under Transverse Magnetic Field," J. Phys. Soc. Japan 16, 1427 (1961).

3.4 Tani, I., "Steady Flow of Conducting Fluids in Channels under Transverse Magnetic Fields, with Consideration of Hall Effect," J. Aerospace Sci. 29, 297 (1962).

3.5 Appollonskii, S.M., and Yu.P. Koskin, "On Transverse Velocity Disturbances in Magnetohydrodynamic Channel Flows, Magnetohydrodynamics 5, 37 (1968).

3.6 Sastry, V.U.K., and C.V.V. Bhadram, "Effect of Hall Currents on the Hydromagnetic Flow in an Annular Channel with a Radial Magnetic Field," Phys. Fluids 21, 857 (1978).

3.7 Liu, B.L., J.T. Lineberry, and H.J. Schmidt, "Simplified Three-Dimensional Modeling for MHD DCW Channels," J. Energy 7, 456 (1983).

3.8 Ishikawa, M., and J. Umoto, "New Approach to Calculation of Three-Dimensional Flow in MHD Generators," in Proc., 22nd Symposium on Engineering Aspects of Magnetohydrodynamics, Starkville, Mississippi, 1984.

3.9 Maxwell, C.D., D.M. Markham, S.T. Demetriades, and D.A. Oliver, "Coupled Electrical and Fluid Calculations in the Cross-Plane in

Linear MHD Generators," in Proc., 16th Symposium on Engineering Aspects of Magnetohydrodynamics, Pittsburgh, Pennsylvania, 1977.

3.10 Bityurin, V.A., V.N. Zatelepin, and G.A. Lyubimov, "Effect of Force-Field Nonuniformity on Flow in an MHD Channel, Fluid Dyn. 13, 1 (1978).

3.11 Doss, E.D., and R.K. Ahluwalia, "Three-Dimensional Flow Development in MHD Generators at Part Load, J. Energy 7, 289 (1983).

3.12 Demetriades, S.T., D.A. Oliver, T.F. Swean, and C.D. Maxwell, "On the Magnetoaerothermal Instability," AIAA 19th Aerospace Sciences Meeting, St. Louis, Paper No. AIAA-81-0248, 1981.

3.13 Girshick, S.L., and C.H. Kruger, "Evidence of Secondary Flow in Faraday MHD Generators," in Proc., 21st Symposium on Engineering Aspects of Magnetohydrodynamics, Argonne, Illinois, 1983.

3.14 James, R.K., and C.H. Kruger, "Joule Heating Effects in the Electrode Wall Boundary Layer of MHD Generators," AIAA J. 21, 679 (1983).

3.15 Barton, J.P., "Fluctuations in Combustion-Driven MHD Generators," Ph.D. Thesis and HTGL Rept. No. 118, Stanford University, 1980.

3.16 Starr, R.F., L.S. Christensen, G.W. Garrison, and G.L. Whitehead, "Preliminary Faraday Performance of a Large Magnetohydrodynamic Generator at High Magnetic Field," J. Energy 6, 163 (1982).

3.17 McClaine, A.W., D.W. Swallom, and R. Kessler, "Experimental Investigation of Subsonic, Combustion-Driven, MHD Generator Performance," J. Propulsion 11, 263 (1985).

3.18 Mitchner, M., and C.H. Kruger, Partially Ionized Gases, Wiley, New York, 1973.

3.19 Swean, T.F., D.A. Oliver, C.D. Maxwell, and S.T. Demetriades, "Prediction of Transverse Asymmetries in MHD Ducts with Zero Net Hall Current," AIAA J. 19, 651 (1981).

3.20 Melling, A., and J.H. Whitelaw, "Turbulent Flow in a Rectangular Duct," J. Fluid Mech. 78, 289 (1976).

3.21 Girshick, S.L., "Secondary Flow in a Magnetohydrodynamic Channel," Ph.D. Thesis, Stanford University, 1985.

3.22 Maxwell, C.D., D.W. Early, and S.T. Demetriades, "Predicted Strength and Influence of MHD-Induced Secondary Flows in Recent Experiments," in Proc., 23rd Symposium on Engineering Aspects of Magnetohydrodynamics, Somerset, Pennsylvania, 1985.

3.23 Reis, J.C., and C.H. Kruger, "Turbulence Suppression in Combustion-Driven Magnetohydrodynamic Channels,"J. Fluid Mech. 188, 147 (1988).

4.0 PUBLICATIONS AND PRESENTATIONS

To date this program has resulted in the following publications and presentations:

Girshick, S.L., and C.H. Kruger, "Evidence of Secondary Flow in Faraday MHD Generators," 21st Symposium on Engineering Aspects of Magnetohydrodynamics, Argonne, IL, 1983.

Kruger, C.H., and S.L. Girshick, "A Review of MHD Boundary Layer Research at Stanford, with Emphasis on Measurements of the Effects of Secondary Flows," 8th International Conference on MHD Electrical Power Generation, Moscow, USSR, 1983.

Self, S.A., and L. Eskin, "The Boundary Layers Between Electrodes and a Thermal Plasma," IEEE Trans. Plasma Science, P.S. 11, 279-285 (Dec. 1983).

Girshick, S.L., and C.H. Kruger, "The Transverse Flow Field in an MHD Channel," IEEE International Conference on Plasma Science, May 14-16, 1984, St. Louis.

Girshick, S.L., and C.H. Kruger, "Measurements of Secondary Flow in an MHD Channel," 22nd Symposium on Engineering Aspects of MHD, Mississippi State University, MS, June 26-28, 1984.

Girshick, S.L., and C.H. Kruger, "Experimental Study of Secondary Flow in an MHD Channel," 23rd Symposium on Engineering Aspects of MHD, Somerset, PA, June 1983.

Self, S.A., and L.D. Eskin, "Plasma-Sheath Structure for an Electrode Contacting an Isothermal Plasma: I. Formulation and Quasi-Neutral Solution," presented at the 38th Gaseous Electronics Conference, Monterey, CA, October 1985.

Eskin, L.D., and S.A. Self, "Plasma-Sheath Structure for an Electrode Contacting an Isothermal Plasma: II. An Electrically Isolated (Floating) Electrode," presented at the 38th Gaseous Electronics Conference, Monterey, CA, October 1985.

Jaffe, S.M., M. Mitchner and S.A. Self, "Electron-Ion Recombination Rates in an Atmospheric Pressure Plasma," presented at the 38th Annual Gaseous Electronics Conference, Monterey, CA, October 1985.

Eskin, L.D., and S.A. Self, "Plasma-Sheath Structure for an Electrode Contacting an Isothermal Plasma: I. Formulation and Quasi-Neutral Solution," submitted to Phys. Fluids.

Kruger, C.H., "Boundary Layer Phenomena in MHD Generators," 3rd US/Japan Symposium on MHD, Hakone, Japan, August 1985.

Girshick, S.L., and C.H. Kruger, "Experimental Study of Secondary Flow in a Magnetohydrodynamic Channel," J. Fluid Mech., 170, 233-252 (1986).

Eskin, L.D., and S.A. Self, "Plasma-Sheath Structure for an Electrode Contacting an Isothermal Plasma: III. Cathodes," presented at the 39th Gaseous Electronics Conferece, Madison, WI, October 1986.

Jaffe, S.M., M. Mitchner and S.A. Self, "Electron-Ion Recombination Rates in an Atmospheric Pressure Plasma," presented at the 39th Gaseous Electronics Conference, Madison, WI, October 1986.

Kruger, C.H., "Stanford MHD Program, MHD Secondary Flows," US/Japan Workshop, Honolulu, HI, 1986.

Girshick, S.L., and C.H. Kruger, "Secondary Flow in a Linear MHD Channel with Applied Axial Current," 9th International Conference on MHD Electrical Power Generation, Tsukuba, Ibaraki, Japan, 1986.

Kruger, C.H., and R.C. Goforth, "New Measurements of Secondary Flow in an MHD Channel," 25th SEAM Symposium, Bethesda, MD, 1987.

Eskin, L.D., and S.A. Self, "Plasma-Sheath Structure for an Electrode Contacting an Isothermal Plasma, Including Electron Energy Effects," presented at the 40th Gaseous Electronics Conference, Atlanta, GA, October 1987.

Jaffe, S.M., M. Mitchner, and S.A. Self, "Measurement of the Recombination Rate of Cs^+ and e^- in High-Pressure Molecular Cases," presented at the 40th Gaseous Electronics Conference, Atlanta, GA, October 1987.

Reis, J.C., and C.H. Kruger, "Turbulence Suppression in Combustion-Driven Magnetohydrodynamic Channels," J. Fluid Mech, **188**, 147, March 1988.

Goforth, R.C., and C.H. Kruger, "Measurements of the Effect of Interaction Parameter and Wall Temperature on Secondary Flow in an MHD Channel," accepted for publication, 26th SEAM Symposium, Nashville, Tennessee, 1988.

Eskin, L.D., and S.A. Self, "The Transition from Diffuse Mode to Constricted Mode Current Transfer for a Plane Electrode Contacting a Thermal Plasma," to be presented at the 41st Gaseous Electronics Conference, Minneapolis, MN, October 1988.

5.0 PERSONNEL

The following personnel contributed to this report:

Charles H. Kruger	Professor and Chairman, Department of Mechanical Engineering (Ph.D. Mechanical Engineering, minor Physics, Massachusetts Institute of Technology 1960. Thesis: "The Axial Flow Compressor in the Free Molecule Range")
Morton Mitchner	Professor, Department of Mechanical Engineering (Ph.D. Physics, Harvard University 1952. Thesis: "The Propagation of Turbulence into a Laminar Boundary Layer")
Sidney A. Self	Professor (Research), Department of Mechanical Engineering (Ph.D. Physics, London University 1965. Thesis: "Radio-Frequency Interaction in a Beam-Generated Plasma System")
Rolf G. Hernberg	Visiting Professor, High Temperature Gasdynamics Laboratory, Department of Mechanical Engineering (Doctor of Technology, Tampere University of Technology, Tampere, Finland 1983)
Leo D. Eskin	Research Assistant, High Temperature Gasdynamics Laboratory, Department of Mechanical Engineering. (M.S. Mechanical Engineering, Virginia Polytechnic Institute and State University 1981. Thesis: "Application of the Monte Carlo Method to the Transient Thermal Modeling of a Diffuse-Specular Radiometer Cavity")
Stephen M. Jaffe	Research Assistant, High Temperature Gasdynamics Laboratory, Department of Mechanical Engineering (M.S. Mechanical Engineering, Stanford University 1983)
Douglas W. Johnson	Research Assistant, High Temperature Gasdynamics Laboratory, Department of Mechanical Engineering (B.S. ME, 1984), University of California, Davis
R. Calvin Goforth	Research Assistant, High Temperature Gasdynamics Laboratory, Department of Mechanical Engineering (B.S. Mechanical Engineering, University of Texas, Austin 1984)

END
DATE
FILMED
DTIC
10-88